UNIVERSITY OF HERTFORDSHIRE

MSC BY RESEARCH DEGREE THESIS

Spectral ageing in the most powerful radio galaxies

Author:
Vijay MAHATMA

Supervised by:
Prof. Martin J. HARDCASTLE

Centre for Astrophysics Research
School of Physics, Astronomy and Mathematics
University of Hertfordshire

Submitted to the University of Hertfordshire in partial fulfilment of the requirements of the degree of Master of Science.

September 2016

Abstract

Radio-loud AGN represent the most energetic and influential large-scale structures in the Universe. Through physical processes such as AGN feedback, they are suggested to play a major role in the evolution of galaxies. The key physical parameter in these studies is the jet power, which requires an accurately determined age for the source.

In this thesis I present a detailed investigation of the dynamics and energetics of two powerful radio galaxies found in cluster environments, in order to probe the well known spectral age/dynamical age discrepancy. Through the use of the high-resolution and newly improved radio interferometer, the JVLA, I present the highest fidelity radio maps of 3C320 and 3C444 to date, which I then use to determine their spectral ages. I also present analysis of the deep and sensitive *Chandra* observation of the cluster shock surrounding 3C320, used to determine its dynamical age.

Applying the most widely used models of spectral ageing I find that, although all models do not provide a reasonable fit to the data, the spectral and dynamical ages can be brought into agreement. I find that the low frequency spectral index (injection index) is relatively flat for these sources, agreeing with previously held assumptions although in contrast to recent work on spectral ageing. There is some suggestion to reject the Kardashev-Pacholczyk model as a valid ageing model for powerful radio galaxies, although this is not robust. I suggest that, since the Tribble model provides consistent fits compared to the other models while providing a more physically realistic description of spectral ageing in the lobes of radio galaxies, it may proceed to be the ageing model of choice for future studies. I argue that the combination of broad-bandwidth data at low and high frequencies with a lobe magnetic field that has a large departure from equipartition estimates can give an agreement between spectral and dynamical ages. I also argue that projection effects and a robust determination of the Mach number of the driven shock by the radio galaxy into its environment are also important factors which may cause a discrepancy in ages.

I find no evidence for the conclusions drawn from previous work on powerful radio galaxies in rich-cluster environments, where it was suggested that their lobes are apparently under-pressured with respect to their environment and therefore require a significant contribution from non-radiating particles for pressure-balance. I therefore suggest that conclusions cannot be made regarding the effect of the environment on lobe particle content of powerful radio galaxies in these rich environments until further samples are studied.

Declaration

I declare that no part of this work is being submitted concurrently for another award of the University or any other awarding body or institution. This thesis contains a substantial body of work that has not previously been submitted successfully for an award of the University or any other awarding body or institution. Except where indicated otherwise in the submission, the submission is my own work and has not previously been submitted successfully for any award.

Vijay Mahatma
September 2016

Contents

List of Figures

List of Tables

Chapter 1

Introduction

1.1 Active Galactic Nuclei

Active Galactic Nuclei (AGN) are some of the most powerful and luminous astrophysical objects in the observable universe. They represent the active core of a galaxy containing a supermassive black hole (SMBH) and its surrounding accretion system (Figure 1.1). Relativistic jets of radiating matter originating from the accretion system can be generated, and can extend as far as a few Mpc (outside the host galaxy) where they terminate in the intergalactic or intracluster medium for AGN in clusters. Due to their interaction with their environment, AGN can play a key role in interstellar, intergalactic and intracluster evolution. It is clear therefore that in order to understand the evolution of the Universe, understanding the dynamics of AGN is vital. Figure 1.1 gives a rendering of how a typical powerful AGN is expected to be seen.

'Radio Galaxies', 'Quasars' and 'Blazars' have all been identified as classes of AGN in contemporary studies. In the past these classifications have been somewhat difficult to make due to the poor resolution of telescopes and other limitations of instruments. Some observations of AGN exhibit features that define other classes, while some are difficult to classify at all due to poorly resolved images. Studies of AGN to probe their dynamics and morphological structures are therefore often difficult, requiring extensive observations at multiple wavelengths. High resolution observations using powerful telescopes are also necessary to avoid such problems, although the unification picture also points to a potential solution to classification problems (Section 1.6).

A brief history of the initial observations and subsequent discoveries of the different types of AGN is given first in this introductory chapter, with particular emphasis on the so called radio galaxies. A theoretical description of the way AGN may be triggered is also given. Section 1.2 then explains some of the physics governing the various observed characteristics that may be exclusive only to radio galaxies.

FIGURE 1.1: Artist's impression of an AGN-an active supermassive black hole accreting matter and releasing powerful outflows. *Credit: Wolfgang Steffen, Cosmovision; Marscher et al., NRAO/AUI/NSF*.

Section 1.3 explains the effects they may have on their surrounding environment that are important for AGN studies. Sections 1.4 and 1.5 describe other interesting studies that have accompanied the introduction of more powerful modern day telescopes, such as the effects of *relativistic beaming* and unified models of AGN. Sections 1.6-1.7 describe the physical radiation processes that explain the observed radiation from AGN, while highlighting outstanding questions that still need to be addressed regarding our understanding of radio galaxies. The project aims are then given in Section 1.8 and finally Section 1.9 describes two of the current most powerful telescopes used in contemporary studies of AGN, which will be used in the remainder of this thesis.

1.1.1 Brief history

Spectroscopic observations give detailed information of the observed flux of a source as a function of observing frequency—known as the *spectrum* of a source. The properties of the spectrum of an astrophysical source, such as emission lines, have historically been used to identify the physical properties of the source. This has indeed been the case for AGN and in fact, spectroscopic observations led to the very first identification of AGN, as described below.

The existence of unusually broad emission lines from the spectra of certain galaxies was first observed in 1943 by Carl Seyfert (Seyfert, 1943). These broad lines were generally not observed in normal galaxies, and eventually became a characteristic feature observed in what are now known as 'active

galaxies'. These galaxies were named 'Seyfert' galaxies, and were spiral in morphology with a very bright nucleus. This class was further subdivided into 'Seyfert 1s' and 'Seyfert 2s' based on the relative widths of their emission lines. The continuum emission from these Seyferts is usually strong at most wavelengths (X-ray through to infra-red), but weak at long wavelengths (radio).

1.1.1.1 Quasars

After the discovery of Seyferts, the search for other galaxies with broad emission lines became popular amongst astronomers. The earliest detections of one of the most luminous classes of AGN, 'Quasars', came in the late 50's as astronomers from the Mullard Radio Astronomy Laboratory in Cambridge made their first all-sky radio maps. Most of the radio sources in the maps were identified as either Galactic supernova remnants or what are now known as 'radio galaxies' (described in Section 1.1.2), but some very compact sources were unidentified due to the poor resolution of radio telescopes at the time. One of these unidentified sources, later named 3C48 (the 48th source in the third Cambridge radio catalogue), was further studied using optical telescopes by Thomas Matthews and Alan Sandage (Matthews and Sandage, 1963). Although broad emission lines were present in the optical spectrum, which was peculiar at the time for a source which was actually emitting brightly at radio wavelengths, they first identified the source to be Galactic in origin—i.e, a 'radio star'.

However, a subsequent redshift study of 3C48 by Greenstein and Matthews (1963) gave a redshift of $z \approx 0.37$, giving evidence for an extragalactic origin of the source. Further radio sources such as these were later found with other telescopes, such as the Lovell telescope at Jodrell Bank, and were used to identify many more of these extragalactic sources which were found to have luminosities of up to $\sim 10^{13}$ $L_{\odot}$-around an order of magnitude greater than the most luminous regular galaxies. This very high luminosity observed for such a distant source was startling. It was later found that these ultra-luminous sources, named 'quasars', represent the very bright nucleus of an active galaxy containing an accreting supermassive black hole (Section 1.1.3).

1.1.1.2 LINERS

Spectroscopic observations were still being used prominently in the hunt for more quasars. Low Ionization Nuclear Emission Line Region Galaxies (LINERS) were identified in this process. These sources possessed weak and narrow emission lines from the spectra of their nuclei. Due to the large difference between their spectra and those of typical quasars, it is generally a matter of debate whether LINERS are really AGN, or whether their cores include a large amount of star formation, or radiate via other processes. Optical observations provide the added difficulty that the high luminosity 'AGN-like' nuclear emission from LINERS can be shrouded by starlight from the underlying galaxy. Radio and X-ray observations, which are usually unaffected by host galaxy emission, therefore became important in

identifying whether a particular LINER is an AGN. The search for AGN using high-resolution radio telescopes drove further developments in the field of radio astronomy. In particular, the increasing need for high-resolution radio mapping led to the advance of 'radio interferometry', which became a popular tool used to observe radio sources in greater detail than that obtained with single dish telescopes (see Section 1.9).

1.1.1.3 BL Lacs and Blazars

A further peculiar class of AGN observed were the BL Lacertae objects (BL Lacs). Also originally thought to be stars, they were found to show unusually featureless spectra with neither emission or absorption lines—i.e., continuum spectra, along with high luminosity at radio wavelengths. The spectra were 'flat' and showed a *power-law* form up to radio wavelengths. This means that the spectrum has a form such that $S_\nu \sim \nu^{-\alpha}$ where $\alpha \leq 0.5$ is known as the *spectral index*. This spectrum is deemed to be flat since, on a log-log plot, the spectrum shows only a weak decline of flux with frequency.

As well as a flat power-law spectrum, there was also evidence of strong linear polarization at the nucleus (indicative of non-thermal emission—see Section 1.3) from the observed emission along with rapid flux variability. Most importantly however, some characteristics in common with 'radio-loud' quasars were found—both classes were bright in the radio compared to optical and both showed a power-law form for the IR-optical spectra, implying that BL Lacs were a type of AGN. Further evidence was also obtained in the mid 70's for other AGN that showed similar features to BL Lacs such as extreme variability and strong linear polarisation. Their variability however, was found to be very erratic, often found to be showing long periods of stability followed by rapid flaring in timescales of just days. A further distinction was that they usually contained broad and strong optical emission lines, unlike the continuum emission from classical BL Lacs. These were termed 'Optically Violent Variable' (OVV) quasars. OVV quasars and BL Lacs are collectively known as 'Blazars', although treated as separate entities for observational purposes. Evidence was obtained from VLBI techniques (a method of obtaining very high resolution observations—see Section 1.9) for a *jet* structure close to the AGN with 'blobs' of emission at radio wavelengths.

Radio-loud quasars, BL Lacs and Blazars collectively became known as 'radio-loud AGN'. The ubiquitous nature of these objects at radio wavelengths provoked further observations with more powerful radio telescopes. A further class of radio-loud AGN were then observed which had extended structure from parsec (Birkinshaw et al., 1981; Alexander, 1987) to megaparsec scales (Willis and Strom, 1978; Kellermann and Pauliny-Toth, 1981), compared to the compact structures discussed until now. These powerful and extended radio-emitting sources were called 'radio galaxies'.

1.1.2 Extended double radio galaxies

Although radio-loud AGN were observed many years ago, the advent of powerful radio telescopes such as the JVLA (see Section 1.9) have enabled very high resolution images to be obtained. We are now able to observe extended radio galaxies and resolve these large structures to very small (arc-second) scales, revealing their true morphology (other than their bright unresolved core which is seen for all types of AGN). These radio galaxies represent radio-loud AGN that show bright and extended *lobe* structure at radio wavelengths that can extend up to the megaparsec scale away from the core. There may also be a narrow jet of radiation bridging the gap between the core and one of the lobes, and in fact some are observed to show two collimated twin jets symmetrically emerging from either side of the core which terminate at the outermost region of the lobes. This is in contrast to radio-loud quasars which may only contain a single jet without extended lobes. This observable emission from radio galaxies has therefore identified them as some of the largest structures in the Universe.

1.1.2.1 The Fanaroff-Riley Class

Radio galaxies were found to have a wide range of morphologies themselves, as well as differences in luminosity. This was first observed by Bernard Fanaroff and Julia Riley in 1974 (Fanaroff and Riley, 1974), and radio galaxies with extended structure were classed as either FR-I or FR-II.

For FR-I radio galaxies the brightest region is usually at the core, corresponding to the AGN, with smooth and diffuse jets appearing fainter with distance from the core. Their spectra are generally flat at the core, getting steeper with distance towards the edges of the lobes. FR-II sources on the other hand, are lobe-dominated sources. They appear to contain collimated but usually fainter jets than FR-Is, possibly due to the large contrast between the bright lobes and the less luminous jets (see Figure 1.2). Unlike FR-Is, the edges of the lobes may contain 'hotspots' which are compact and extremely bright regions. Furthermore, the jets are predominantly 'one-sided'—meaning that one of the two jets is usually more visible than the other, possibly due to *relativistic beaming* effects (see Section 1.5). The physical interpretation for the existence of these structures are described in detail in Section 1.2.

This morphological difference was also shown to correspond to a physical difference in luminosities. FR-Is have the lower luminosities of the two groups. At a radio observing frequency of 178 MHz, Fanaroff and Riley concluded that there is a luminosity cut-off at 5×10^{25} W Hz^{-1}, below which generally FR-I radio galaxies are found and above which FR-IIs are found (Fanaroff and Riley, 1974).

In terms of their central host galaxies, FR-Is are associated with bright and large elliptical galaxies and are often located in rich clusters. Due to their lower power compared to FR-IIs, their jets can often be in

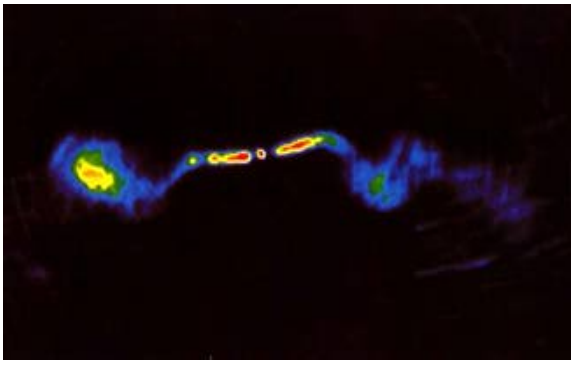

(A) FR-I radio galaxy 3C449

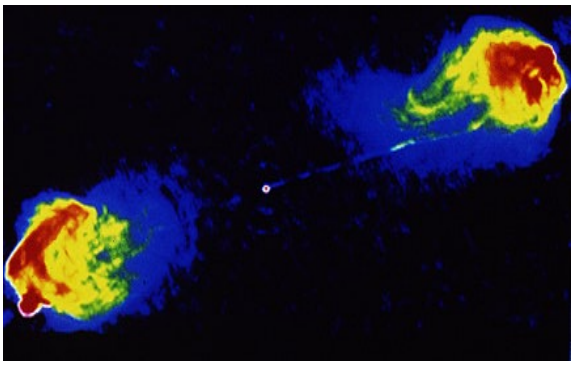

(B) FR-II radio galaxy 3C405

FIGURE 1.2: JVLA images showing the clear morphological difference between FR-I and FR-II radio galaxies. 3C449 on the left was observed at a wavelength of 20cm (Perley et al., 1979), while 3C405 (Cygnus A) on the right was observed in 1996 at a wavelength of 6cm (Carilli and Harris, 1996).

direct contact with their environment. In particular the jets of FR-Is may contain a mixture of particles from the surrounding environment as they are entrained by the propagating jet (Bicknell, 1984; Croston et al., 2005b, 2008), evident by their lower power and decelerating jets. Jets and their effect on their external environment are explained more detail in Section 1.2.

FR-IIs are usually associated with normal elliptical galaxies and traditionally not found in rich cluster environments, particularly at low redshift. Evidence has been obtained using modern day instruments however, for some FR-II radio galaxies in rich cluster environments (Smith et al., 2002; Croston et al., 2011), and in fact they are very interesting to study in these cases—see Section 1.5.

The recent advance of radio interferometric observations using modern day instruments, such as the JVLA (Section 1.9) and MERLIN, has enabled much greater resolution to be obtained for extended radio galaxies (e.g. Harwood et al. (2013, 2015)) than had been available in the past. We are able to probe the detailed structure of FR-Is and FR-IIs including the radio lobes and the structure of the jets near the core using VLBI techniques (Tingay et al., 1998; Giovannini et al., 2001). Furthermore, JVLA observations are now able to probe radio-loud AGN on arcsec scales at full bandwidth capabilities, meaning that the continuum emission can be measured at a broad range of frequencies in a single observation (further

details about JVLA capabilities are given in Section 1.9). Multi-frequency observations are essential since we can then observe how the spectra changes over a broad range of frequencies, and this can give information about the underlying physics within the structures of radio galaxies, such as the process of *spectral ageing* in the lobes (Section 1.7).

1.1.2.2 Radio spectra

Radio galaxies often show distinct features such as steep spectra that are generally unobserved in the spectra of other types of radio-loud AGN. In general, radio-loud AGN are described in terms of two fundamental spectral types:

- Flat spectra (core dominated)
- Steep spectra (extended emission)

The first evidence for AGN with flat radio spectra came with the advent of BL Lacs—as discussed previously. The emission mechanism which is responsible for this radio emission has been accepted to be the synchrotron process—where relativistic electrons lose energy in the form of radiation via interaction with a magnetic field (see Section 1.3).

The characteristics of flat spectrum and steep spectrum sources vary remarkably. Flat spectrum sources such as BL Lacs and quasars are compact and core-dominated as explained previously—the brightest emission comes from the nuclear regions of the host galaxy and dominates the emission. Their spectrum follows that of a power-law form. Radio galaxies, particularly in the lobes, have steep spectra with higher spectral indices—containing a peak at low frequencies and decreasing flux with increasing frequency. The physical interpretation and mechanisms behind the observed flat and steep spectra in radio-loud AGN are explored further in Section 1.3.

1.1.3 Core and accretion power

The compact core of AGN, whether radio-loud or radio-quiet, is extremely bright regardless of the observing frequency. The obvious questions are then *where* does this ultra-luminous radiation come from and *why* do the cores and other structures radiate so brightly? Furthermore, what are the physical mechanisms by which AGN are powered?

The current best theoretical explanation of the source of AGN power is accretion (Pringle, 1981; Shlosman et al., 1990). The core of an AGN contains a SMBH, and due to its enormous gravitational pull,

surrounding cold or hot matter gets accreted (Fabian, 1984; Hardcastle et al., 2007). By simple Newtonian laws, a massive body accretes a nearby object towards the centre of its gravitational pull, which then releases gravitational potential energy. This energy is expected to be released in the form of electromagnetic radiation-and this is certainly the case with numerous optical, infra-red, X-ray and radio observations having been made of the core of AGN (e.g. Pearson and Readhead (1988); Wills (1989); Hardcastle et al. (2007)).

Since the gravitational potential energy released by accretion goes as GMm/R, where M and R are the mass and radius of the accreting body respectively, it is clear that accretion power, as a radiation mechanism, is most efficient for the most massive but compact objects such as black holes in AGN. Neutron stars would therefore also fall into this category (Lattimer and Prakash, 2004). The luminosity observed from the core of the AGN must therefore depend on how much matter is accreted per unit time, $\dot{M}$, and hence we expect more powerful AGN in rich environments such as galaxy clusters (Smith et al., 2002). This highlights the relative importance of understanding the dynamics of radio galaxies in rich cluster environments—I return to this topic in Section 1.4. In calculating the luminosity from the core, as a standard calculation we assume all of the accreted matter radiates, however, for a black hole some of the accreted matter could simply disappear into the black hole and add to its mass without radiating and therefore this must be accounted for in luminosity calculations.

Models of AGN therefore involve the generation of radiation in a dense, compact region of accreting material surrounding a supermassive black hole (Hardcastle et al., 2007; Mingo et al., 2014). The accretion mass comes from a supply of gas from which the gravitational potential energy can be extracted. This gas supply can originate from collisions of nearby massive stars or stars from a nearby star cluster having orbits very close to the black hole and being torn apart by tidal forces (although the reality of these gas supply mechanisms are themselves uncertain). In fact, there has been some evidence for large star formation rates near an AGN (King and Pringle, 2007). As an order of magnitude range this mass supply needs to be at a rate of $\sim 1 - 100 M_{\odot}$ yr^{-1} to match the high luminosities observed for typical AGN. Although, theoretically a compact star cluster consisting of several supernovae in a small galaxy without a supermassive black hole can in fact temporarily imitate the characteristics of standard AGN due to the large luminosities outshining the host galaxy emission (see review by in Begelman et al. (1984);Meurer et al. (1995)), however accretion onto SMBH is the generally most accepted model for triggering AGN activity (e.g. Turner and Pounds (1989)).

Other models of gas supply include infall from host galaxy interstellar gas (Shlosman et al., 1990) and galaxy interactions or mergers (Comerford et al., 2015)—introducing turbulence and winds which give rise to gas infall into the nucleus of the galaxy. Large scale poloidal magnetic fields have also been suggested to exist near the core, adding to the possibility of 'magnetic torques' providing a large-scale

inflow of interstellar matter towards the SMBH to trigger AGN activity, rather than nearby dense star clusters. (Shlosman et al., 1990; Balbus and Hawley, 1998; Martí-Vidal et al., 2015).

1.2 Components of radio galaxies

In this section, a description of the dynamics of radio galaxies is given in terms of the various observed extended structures, such as lobes and hotspots. A particular emphasis is given to FR-II radio galaxies, since they represent the most energetic and powerful systems.

The jets and lobes themselves can be observed in the radio band (as in Figure 1.2) associated with the synchrotron radiation released from the relativistic electrons circling in a magnetic field within the jet. The non-thermal spectra and linear polarisation observed from these structures gives sound evidence for the synchrotron origin of the radiation. In FR-II's, there are large radio lobes symmetrically placed on either side of the AGN core, extending far beyond the host galaxy—as far as a few megaparsecs for the largest sources. At the tip of the radio lobes there may contain a compact region of very high radio surface brightness—known as a 'hotspot'. These are seen to be powered by narrow collimated 'radio jets', which represent a bridge between the active nucleus and the hotspots. The jets must therefore originate from the active nucleus, and the physical mechanisms for the jet creation are described below. The host galaxy may also be the most luminous of a cluster of galaxies (Owen et al., 1997). This has particular dynamical implications, as well as implications for the energy transferred into the external medium by the radio jets. The energetic impact on the environment of a powerful radio galaxy is explored further in Section 1.4.

1.2.1 Jets

For extended double radio galaxies, of the type seen in Figure 1.2, it is clear that the energy available in the accretion system or an accretion disk around the SMBH must be directed outward as relativistic or sub-relativistic jets. These jets of radiation have been observed extensively through high resolution radio mapping and VLBI techniques (e.g. Carilli et al. (1991a)). Although high resolution observations close to the core are also possible (Pearson and Readhead, 1988; Giovannini et al., 2001), the mechanisms by which radio jets are generated still cause some debate. Jet creation mechanisms are discussed in Section 1.2.1.1.

In terms of the particle content, it is most likely that the jet material contains relativistic charged particles originating from the core accretion system. The collimated nature of jets gives an *a priori* assumption that they must be electrically neutral, and therefore contain electrons, protons and/or positrons. Electron-proton pairs originating from the accretion flows could provide the bulk of the material in a jet (Celotti

and Fabian, 1993). Furthermore, for low-power jets, protons (from ionised hydrogen) from the ambient medium can make up a significant fraction of the jet material (jet entrainment) (Bicknell, 1984). However, there are also strong cases for electron-positron pair dominance in the jet (Konar and Hardcastle, 2013), and further depolarization studies have effectively ruled out electron-proton jets (Wardle, 1977; Wardle et al., 1998).

It is universally accepted that the radio emission from the material in the jets of radio galaxies is due to synchrotron radiation from relativistic electrons and/or positrons. The physical mechanisms that generate these radio jets associated with AGN are still debated, and a few theories have been proposed—some of which are briefly outlined below.

1.2.1.1 Jet creation

As the matter from the accretion system or accretion disk gets pulled inwards towards the event horizon of a rotating black hole ('Kerr' black hole), the magnetic fields contained in the disk are dragged along the surface of the event horizon, and eventually align themselves along the axis of rotation of the black hole—usually perpendicular to the accretion disk itself. These strong magnetic fields are tightened and collimated, thus allowing charged particles to traverse along them at high speeds (relativistic in most cases). The two well-known theories which describe the jet formation in this way by a spinning black hole are the *Blandford-Znajek* process (Blandford and Znajek, 1977) and the *Penrose* mechanism (Williams, 2004). The charged particles traversing along the magnetic field lines then produce synchrotron radiation, as discussed in Section 1.3, and can therefore be observed as jets of electromagnetic radiation. Synchrotron radiation can be observed in the radio, optical and X-ray regimes, although the difficulty in optical observations arises when the optical emission from the host galaxy and a (kilo)parsec-scale jet cannot be distinguished.

1.2.2 Hotspots and shocks

For an FR-II radio galaxy, the jets move relativistically (e.g. Mullin et al. (2008); Mullin and Hardcastle (2009)). Therefore, they are also travelling supersonically—faster than the speed of sound of the medium through which the jets propagate[1]. Since disturbances in the medium cannot propagate faster than the speed of sound by definition, a discontinuity between the jet and the surrounding material is formed. This abrupt change in pressure, temperature and density in the medium is known as a shock, and is formed along and in front of the jet. This coincides with, at the head of the jet, a region of very bright radio emission—what is known as a *hotspot* (Meisenheimer et al., 1989; Carilli et al., 1991a).

[1] This also explains why jets remain highly collimated out to large distances. Supersonic jets are also less prone to dissipating their kinetic energy as heat, thus maintaining their high velocities over time.

Here, strong shock front is formed at the beam head due to the speed of the jet. Through *Fermi acceleration* processes (Bell, 1978), charged particles in the medium in front of the jet can repeatedly cross the shock front as it advances, and these particles can be accelerated (and re-accelerated) to very high energies (Rachen and Biermann, 1993). This form of particle acceleration gives a power-law form for the energy distribution of the particles (Bell, 1978), which also leads to the power-law form of the observed synchrotron radiation described in Section 1.3.

Particle acceleration from a strong shock at the hotspot therefore becomes necessary in order to explain the extremely bright hotspots observed relative to the lobes—as seen in the VLA map for the prototypical FR-II Cygnus A in Figure 1.2. Further support for particle acceleration arises in considering the radiative loss time-scales for the electrons in the hotspots. The synchrotron radiative lifetimes at the hotspots are usually found to be much shorter than the time taken for light to travel from the core to the hotspots (e.g. (Matthews and Sandage, 1963)). Therefore, not only do the hotspots need to be injected with energy continually by the jets, strong particle acceleration must also take place at the hotspots to maintain their high luminosities without without energy dissipation.

1.2.3 Lobes

It was found that not all of the energy in the hotspots, which is continually injected by the jets, is lost to radiation. Some energy escapes the hotspots to form a 'back-flow' of material in opposition to the jet, forming a large 'cocoon' or lobe structure behind the hotspots (Longair et al., 1973). It was then found by analytical modelling (Kaiser and Alexander, 1997) that the internal pressure given by the material in the cocoon is actually necessary to obtain a fully self-consistent model for the evolution for FR-II's. Here, the energy injected by the jet, the luminosity of the hotspot and the pressure of the lobes are shown to be proportional to each other. This means that as the source evolves, the jets continuously feed the hotspot, the lobes grow larger in volume and the internal lobe pressure increases.

This can be readily observed in the lobes of FR-II radio galaxies through the radiative losses. As the hotspot advances, previously charged particles are left behind, going through energy losses which we observe in the radio lobes. Particularly, the particles are going through synchrotron and inverse-Compton losses, which are explained in detail in the next section.

These observational characteristics of FR-I and FR-II radio galaxies have been well studied using the current generation of radio telescopes such as the JVLA and VLBI techniques (Section 1.9) to probe these structures at high resolution, revealing their extended structure that is otherwise not generally observed in other classes of AGN such as BL Lacs and Blazars. Although the emphasis so far has been on radio maps, multi-wavelength studies help to give a more complete description of the physical processes

in radio-loud AGN. Particularly, deep and sensitive X-ray observations have led to further insights into the underlying physics contained in these powerful structures that help to build on that obtained by the radio images (Hardcastle et al., 1998; Croston et al., 2005b; Mingo et al., 2014). Synchrotron and inverse-Compton losses can produce radiation in the X-ray regime (as well as other wavelengths) and therefore multi-wavelength studies have provided a powerful tool to study radio galaxies in the past (Croston et al., 2005b, 2009; Hardcastle et al., 2009). X-ray telescopes can also probe the rich ambient medium of powerful radio galaxies—as explained in Section 1.4.

1.3 Radiative processes in radio galaxies

So far the dynamics of AGN have been described in detail; how they form, the effect they may have on their environment and how this influences the evolution of the host galaxy or its surrounding galaxy cluster. However understanding their dynamics also requires a thorough understanding of their radiative processes—from the core of the AGN to the environment surrounding the source. Radio galaxies emit radiation at a broad range of frequencies from the radio to the hard X-rays and gamma rays (for extremely powerful and variable objects such as BL Lacs). Here, I quantitatively describe some of the radiation mechanisms responsible for much of the observed emission of radio galaxies. I describe non-thermal processes, which are defined as those where the continuum radiation from the energetic particles cannot be explained by a Maxwellian energy distribution, as well as thermal processes.

1.3.1 Synchrotron losses

It is well known that charged particles that are accelerated produce electromagnetic radiation. When a relativistic charged particle experiences a magnetic field, it gyrates around the field line(s) and therefore radiates—this is called synchrotron radiation. The equivalent non-relativistic case is cyclotron radiation; however for powerful radio galaxies many of the particles are relativistic and therefore I focus only on the relativistic case. Synchrotron radiation is important, particularly for AGN studies where high-energy electrons are common, as are large scale magnetic fields (e.g. Aharonian (2002)). We therefore expect synchrotron radiation to be prominent for AGN, and therefore I quantitatively describe its production here. The following equations are based on derivations from Longair (2011).

1.3.1.1 Single electron

The rate of energy loss for a single, non-relativistic charged particle that is accelerated is given by *Larmor's formula*

$$-\left(\frac{dE}{dt}\right) = \frac{q^2|\mathbf{a}|^2}{6\pi\varepsilon_0 c^3} \tag{1.1}$$

where q is the charge, **a** is the acceleration and the constants have their usual physical values. For a relativistic charged particle, the form changes to

$$-\left(\frac{dE}{dt}\right) = \frac{q^2\gamma^4}{6\pi\varepsilon_0 c^3}\left(|a_\perp|^2 + \gamma^2|a_\parallel|^2\right), \tag{1.2}$$

where $a_\perp$ and $a_\parallel$ are the components of acceleration parallel and perpendicular to the velocity vector. In a magnetic field however, the acceleration is perpendicular to the velocity vector of the particle, and therefore we have

$$\begin{aligned} -\left(\frac{dE}{dt}\right) &= \frac{q^2\gamma^4}{6\pi\varepsilon_0 c^3}|a_\perp|^2 \\ &= \frac{q^2\gamma^4}{6\pi\varepsilon_0 c^3}\frac{e^2v^2B^2\sin^2\alpha}{\gamma^2 m_e^2} \\ &= \frac{e^4B^2}{6\pi\varepsilon_0 c m_e^2}\frac{v^2}{c^2}\gamma^2\sin^2\alpha \end{aligned} \tag{1.3}$$

where we have used $a_\perp = evB\sin\alpha/\gamma m_e$ for centripetal acceleration of a relativistic charged particle. Rearranging terms again and using $c^2 = (\mu_0\varepsilon_0)^{-1}$ we have

$$-\left(\frac{dE}{dt}\right) = 2\left(\frac{e^4}{6\pi\varepsilon_0^2 c^4 m_e^2}\right)\left(\frac{v}{c}\right)^2 c\frac{B^2}{2\mu_0}\gamma^2\sin^2\alpha. \tag{1.4}$$

The first term in brackets on the right hand side with the constant terms is the Thomson cross-section σ_T and the magnetic field term $B^2/2\mu_0 = U_{mag}$ is the magnetic field energy density—the energy per unit volume stored in the magnetic field. Furthermore, in the limit $v \to c$, we then have

$$-\left(\frac{dE}{dt}\right) = 2\sigma_T c U_{mag}\gamma^2\sin^2\alpha. \tag{1.5}$$

For a single high-energy electron, the distribution of pitch angles α is expected to be isotropic. This is because the electrons in a plasma are expected to be scattered by magnetic fields continuously and during their lifetimes any high energy electron can be randomly scattered in pitch angle. Furthermore irregularities in the magnetic field distribution is likely to further randomise the pitch angle distribution. For an isotropic distribution of pitch angles the probability density for a certain pitch angle α is $p(\alpha)d\alpha = \frac{1}{2}\sin\alpha d\alpha$. Multiplying this with the above equation and performing the integral we have

$$-\left(\frac{dE}{dt}\right) = 2\sigma_T c U_{mag}\gamma^2\left(\frac{v}{c}\right)^2\frac{1}{2}\int_0^\pi \sin^2\alpha d\alpha = \frac{4}{3}\sigma_T c U_{mag}\left(\frac{v}{c}\right)^2\gamma^2. \tag{1.6}$$

Therefore, assuming a constant magnetic field and if $v \sim c$, it can be seen that the rate of energy losses go as the square of the particle energy (since $\gamma = E/mc^2$)—i.e. the highest energy electrons have a faster rate of energy loss through synchrotron radiation. Using the derivations of Rybicki and Lightman (1979), it can also be shown that the *emissivity* (the energy radiated as a function of frequency) of a

single electron is

$$j(\omega) = \frac{\sqrt{3}Bq^3 \sin\alpha}{8\pi^2 \varepsilon_0 cm} F'(x), \tag{1.7}$$

where $F'(x)$ is a function of the angular frequency of the electron such that $x = \omega/\omega_c$ where ω_c is the critical angular frequency—above which the emission from the electron falls sharply having radiated away most of its energy.

1.3.1.2 Power-law distribution of electrons

For a distribution of electrons, which is what is physically realistic for astrophysical scenarios, the total synchrotron emissivity then becomes (Longair, 2011)

$$J(\nu) = \int_{E_{min}}^{E_{max}} j(\nu)N(E)dE = \frac{\sqrt{3}Be^3 \sin\alpha}{4\pi\varepsilon_0 cm_e} \int_{E_{min}}^{E_{max}} F(x)N(E)dE. \tag{1.8}$$

Therefore, for an ensemble of particles the shape of the emission spectrum depends on the energy distribution $N(E)$ of the particles. The function $F(x)$ is such that $x = \omega/\omega_c$, as for the single electron case above, and it peaks at the critical frequency ν_c. If we assume that all of the radiation from each electron is emitted at this frequency we can let $F(x) = \delta(x-1)$, making integration easier. If we also let the electron energy distribution be a power-law such that $N(E) = N_0 E^{-p}$ and we use the formulae for the energy for a relativistic electron

$$E = \gamma m_e c^2 = \left(\frac{\nu}{\nu_g}\right)^{1/2} m_e c^2; \;\; dE = \frac{m_e c^2}{2\nu_g^{1/2}} \nu^{-1/2} d\nu, \tag{1.9}$$

we finally obtain the relation

$$J(\nu) \propto N_0 \nu^{-\frac{(p-1)}{2}} B^{\frac{p+1}{2}}. \tag{1.10}$$

This important relation shows that if the electron energy distribution follows a power-law, as we have assumed, then so does the synchrotron spectrum. This power-law spectrum is indeed observed in the lobes of radio galaxies as well as many other sources (e.g Carilli et al. (1991a); Croston et al. (2009)). We can therefore infer that the underlying electron energy distribution in the lobes of radio galaxies must also be a power-law, according to Equation 1.8. For a given magnetic field and electron energy normalisation N_0, we then have that $S(\nu) \propto \nu^{-\alpha}$, where α is called the *spectral index*—the slope of the spectrum. Observed power-law spectra provide key evidence for the synchrotron origin of the radio emission of radio galaxies and other classes of AGN. Synchrotron radiation (from relativistic electrons) is also linearly polarised (Longair 2011), and extensive studies have indeed shown a large amount of polarisation in the structures of radio galaxies—therefore giving further evidence for the synchrotron origin for the radio emission.

1.3.2 Inverse-Compton scattering

Within the structures of radio galaxies, ultra-relativistic electrons can scatter low energy photons to higher energies. Here the photons gain energy while the electrons lose kinetic energy in the process, and this is called *inverse-Compton* scattering. This is so named since *Compton* scattering describes the loss of energy of high energy photons scattering electrons to higher energies. Inverse-Compton scattering is therefore another radiative loss process, as with synchrotron radiation, and has been detected (with significant uncertainty in some cases) in radio galaxies using X-ray telescopes (e.g. Croston et al. (2004, 2005b)). The source of the initial low energy photons can be background CMB photons, photons from the host galaxy or from the central AGN. Radiation from inverse-Compton scattering is therefore important in AGN studies due to the abundance of (ultra)relativistic electrons.

Following the derivations of Longair (2011), we first consider the low-energy limit where a photon encounters a stationary electron and gets scattered due to the interaction with the electric field of the photon—causing the electron to oscillate and therefore emit radiation. The intensity of radiation scattered by an angle α into a solid angle $d\Omega$ by the electric field of the photon is given by

$$-\left(\frac{dE}{dt}\right)_x d\Omega = \frac{e^4|E_x|^2}{16\pi^2 m_e^2 \varepsilon_0 c^3}\cos^2\alpha d\Omega, \tag{1.11}$$

where E_x is the x-component of the electric field of the incident photon. Integrating over all solid angles and summing the radiation in all directions one obtains

$$-\left(\frac{dE}{dt}\right) = \sigma_T c u_{rad}, \tag{1.12}$$

where u_{rad} is the energy density (energy per unit volume) of the scattered radiation. These considerations lead to what is known as *Thomson* scattering—where the electron is stationary and the incident photon frequency do not change as a result of the collision. This is known as an *elastic* scattering. At higher photon energies however, part of the photon energy is transferred to the electron, which recoils as a result. This is known as *Compton* scattering. *Inverse-Compton* scattering occurs when high energy electrons scatter low-energy photons to higher energies, with the electrons transferring energy to the photons. By high energy electrons, we mean ultra-relativistic, and therefore important in the studies of radiation from AGN.

Treating the above equations from Thomson scattering but with special relativistic considerations (see Longair (2011)), one obtains the total energy rate gained by the photon field (or the loss rate of the electrons) as

$$-\left(\frac{dE}{dt}\right)_{IC} = \frac{4}{3}\sigma_T c u_{rad}\left(\frac{v^2}{c^2}\right)\gamma^2. \tag{1.13}$$

We see here that remarkably, the energy loss rate for the electron through inverse-Compton scattering is very similar to the energy loss rate for the electron through synchrotron radiation, Equation 1.6. The differences in the inverse-Compton and synchrotron loss rates lie in the energy densities of the radiation field u_{rad} and magnetic field u_{mag}, respectively.

Owing to its similarity in the energy loss rate with synchrotron radiation, the emissivity of radiation due to inverse-Compton scattering can be found as

$$J_{\rm IC}(\nu_1) \propto N_0 \nu_1^{-\frac{(p+1)}{2}} \int_{\nu_{\rm min}}^{\nu_{\rm max}} \nu_0^{\frac{p-1}{2}} U(\nu_0) d\nu_0 \tag{1.14}$$

(Hardcastle et al., 1998), where ν_0 and ν_1 are the initial and up-scattered frequencies of the photon respectively and $U(\nu_0)$ is the energy density in the photon field. We can see that Equation 1.14 is analogous to Equation 1.8 for the synchrotron emissivity, with the additional integral over the photon field. This is an important result as it highlights the similarity in emissivity between both inverse-Compton and synchrotron radiation (Equation 1.10). In particular, it can be seen that the synchrotron emissivity depends on the magnetic field strength B and the electron normalisation N_0, whereas the inverse-Compton emissivity depends solely on the electron normalisation N_0 (if we know the photon field $U(\nu_0)$). Therefore, with both synchrotron and inverse-Compton emissivities observed, N_0 can be cancelled out to obtain the magnetic field B. This method of obtaining estimates of the magnetic field strength in the lobes of radio galaxies has been used extensively in the past, by detecting both inverse-Compton and synchrotron components of radiation from the lobes (Hardcastle et al., 1998; Croston et al., 2005b, 2008, 2009).

Inverse-Compton emission gives observational evidence for the creation of very high-energy photons, giving a clear physical basis for the commonly observed high frequency X-ray and gamma rays associated with AGN (Croston et al., 2004, 2005b; Stawarz et al., 2013). *Synchrotron self-Compton* is a similar mechanism where the photons created through the synchrotron process by the energetic electrons are scattered themselves by the same electrons. Non-thermal radiation is therefore ubiquitous in AGN, and gives interesting implications for the physics that govern the dynamics and energetics of radio galaxies.

1.3.3 Thermal radiation

Thermal radiation is the electromagnetic radiation released from a heated object, due to the internal energy from the random motions of particles when the object is heated. This random motion consists of the kinetic energy of the particles gained when the temperature of the object or medium is greater than absolute zero. Electromagnetic radiation is then produced when the inter-atomic particles, such as protons and electrons, scatter and accelerate in their own electric field—producing electromagnetic radiation. This again represents an energy loss and was named *bremsstrahlung* (the German for ‘braking

radiation').

The speeds of particles moving freely in a closed system, and in thermodynamic equilibrium, can be described by the Maxwell-Boltzmann distribution. This gives the probability for a particle to be in a specific range of speeds, and depends on the particle mass and the temperature of the medium. Therefore, the electron density N_e at a particular range of velocities dv (Longair, 2011) is given by

$$N_e(v)dv = 4\pi N_e \left(\frac{m_e}{2\pi kT}\right)^{3/2} v^2 exp\left(-\frac{m_e v^2}{2kT}\right) dv. \tag{1.15}$$

This can then be substituted into an approximate formula for the spectral emissivity of a thermal plasma of electron density N_e (as a function of angular frequency ω), as shown in Longair (2011)

$$J(\omega) \approx \frac{Z^2 e^6 N N_e}{12\sqrt{3}\pi^3 \varepsilon_0^3 c^3 m_e^2} \left(\frac{m_e}{kT}\right)^{1/2} g(\omega, T) \tag{1.16}$$

where N is the space density of nuclei in the thermal medium, and $g(\omega, T)$ is the *Gaunt factor*. Note that this spectrum reflects the low frequency electrons, where at high frequencies the spectrum cuts of exponentially as $\exp(-\bar{h}\omega/kT)$—since the Maxwell-Boltzmann distribution does so at high particle speeds. This cut-off occurs at X-ray energies, and the spectrum is roughly flat at energies lower than this.

The total energy loss rate of the plasma is found, as has been described for the non-thermal energy losses, by integrating the spectral emissivity from Equation 1.16 over all frequencies. This gives the energy loss rate for thermal bremsstrahlung as

$$-\left(\frac{dE}{dt}\right)_{\text{brem}} = kZ^2 T^{1/2} \bar{g} N N_e \tag{1.17}$$

where k represents the constant terms after integration and the frequency averaged Gaunt factor $\bar{g} \sim 1.2$.

For hot X-ray emission from a thermal plasma, where the interpretation for this radiation is thermal bremsstrahlung, X-ray observations can therefore provide information of the temperature and electron densities of the plasma. This has been key to quantifying the dynamics in cluster environments, where the hot X-ray emitting plasma at the centre of a galaxy cluster radiates via the bremsstrahlung process.

1.4 The environment of radio galaxies

1.4.1 Effects of radio galaxies on their environment

It has long been known that radio galaxies and other types of AGN are in 'contact' with their environment—i.e. that that the particles in the jets and lobes interact with the particles in the external medium. This has been found to be particularly true for lower power FR-I radio galaxies where the jets are diffuse and their deceleration at large scales is thought to be due to the entrainment of external particles (Bicknell, 1984; Hardcastle et al., 2002; Croston et al., 2008; Hardcastle, 2008). Classical double radio galaxies such as Cygnus A on the other hand, shown in Figure 1.2, show clear and collimated jets and lobes out to large scales in line with the jet axis and are thought to not be in such contact with their environment (Croston et al., 2005a). Deviations from the classical picture of radio galaxies such as bending of the jets and distortions of the lobes are also likely to be due to particle collisions and scattering from the external medium of the radio source.

The external medium can be the interstellar medium (ISM) for small and young radio galaxies whose jets interact mainly with the host galaxy; the intergalactic medium (IGM) for jets powerful enough to escape the host galaxy; or the intra-cluster medium (ICM) for radio galaxies in a cluster of galaxies. FR-I radio galaxies are generally found in group or cluster environments (Croston et al., 2008), and are particularly prone to particle entrainment of the intra-cluster gas (Hardcastle et al., 2002; Croston et al., 2008; Hardcastle, 2008). The more powerful FR-IIs, are less ubiquitous and also tend not to inhabit cluster environments at low redshift, although there is evidence that at moderately higher redshifts ($0.45 \leqslant z \leqslant 4$) a majority of FR-IIs lie in cluster environments (Hill and Lilly, 1991; Pentericci et al., 2000; Best, 2004). High redshift sources can drive resolution capabilities of telescopes to their limit, and therefore FR-Is at low redshift become ideal for observations due to their prominence in cluster environments.

However, FR-IIs are much more energetic in terms of their jet powers and therefore the interaction with their external medium in cluster environments can present interesting physics: the nearby FR-II Cygnus A has evidence of driving a shock into the hot thermal gas of its surrounding cluster medium, as observed with *Chandra* (Smith et al., 2002). The dynamics of powerful radio galaxies in environments such as this have been tested extensively in numerical models (Basson and Alexander, 2003; Krause, 2005; O'Neill and Jones, 2010; Hardcastle and Krause, 2013), and it is vital that these models are tested against actual observations. It is therefore important to study the most powerful (FR-II) radio galaxies in cluster environments with central hot thermal regions.

1.4.2 Cluster properties

A rich galaxy cluster contains hundreds to thousands of galaxies in a (roughly) spherical distribution. It contains hot thermal X-ray emitting gas which is generally hotter towards the centre, as a consequence of its strong gravitational potential driving material inwards, converting gravitational potential energy into kinetic energy. The cluster is also in hydrostatic equilibrium, assuming the hot gas is almost at rest in the local gravitational potential well. The hot gas in clusters of galaxies is therefore 'virialised'—the temperature of the gas is implied by the virial theorem. As a result the medium contains a large number of hot ions and electrons, which then go through a process of radiative losses (thermal bremsstrahlung). The galaxies in a cluster are therefore embedded in a large central region of hot X-ray emitting gas.

However, a problem arises in that there must be a mechanism by which the cluster gas remains at these hot temperatures without cooling significantly. Potentially, *shock heating* by a residing powerful radio galaxy in the cluster could provide a solution, although there are arguments to suggest otherwise (Omma and Binney, 2004). As explained previously, powerful radio galaxies at high redshift are common, whereas at low redshifts where AGN are easier to detect, the most powerful radio galaxies tend to inhabit poor-cluster environments. The physical reason for this redshift dependence is unclear, although the overall presence of powerful radio galaxies in clusters may be explained by galaxy interactions (major mergers) close to the centre of the cluster triggering AGN activity (Treister et al., 2012).

1.4.3 Shock heating

As mentioned above, an advancing powerful radio galaxy may drive a supersonic shock into its immediate surrounding medium, accelerating particles to higher energies (Smith et al., 2002; Mingo et al., 2014) (analogous to shock acceleration in the hotspots of radio galaxies). This shock, which one would expect to be symmetrically surrounding the radio galaxy, heats the gas to higher X-ray energies. The result is that the regions of the cluster near the radio galaxy are much hotter and brighter relative to the outer cooler X-ray emitting gas. The conditions for shock heating are given by the Rankine-Hugoniot relationships for the differences in the densities, pressures and temperatures between the shocked and un-shocked thermal medium:

$$\begin{aligned}
\frac{\rho_2}{\rho_1} &= \frac{\Gamma+1}{\Gamma-1+2/\mathscr{M}^2} \\
\frac{p_2}{p_1} &= \frac{2\Gamma\mathscr{M}^2+(1-\Gamma)}{\Gamma+1} \\
\frac{T_2}{T_1} &= \frac{\left[2\Gamma\mathscr{M}^2+(1-\Gamma)\right]\left[\Gamma-1+2/\mathscr{M}^2\right]}{(\Gamma+1)^2},
\end{aligned} \tag{1.18}$$

where Γ is the adiabatic index of the gas such that $p \propto \rho^{\Gamma}$, the subscripts 1 and 2 denote the unshocked and shocked medium respectively and $\mathscr{M}$ is the Mach number. The Mach number is a quantity that describes the strength of the shock, given by the ratio of the shock advance speed and the speed of sound of the pre-shocked external medium.

Measuring the gas temperature and density of these environments can therefore give important information about the strength of a shock due to a residing radio galaxy on its external environment. Crucially however, if a shock is actually observed, then by analysing this X-ray emission to determine a Mach number and the speed of sound, an estimate of the lobe advance speed can be obtained. Then, with an accurate determination of the length of the jet, an age of the radio source can be obtained. This is known as its 'dynamical' age.

The process of shock heating can potentially explain the 'cool-core' problem of clusters, as mentioned previously, which asks how the thermally emitting X-ray plasma of the ICM is kept hot without dissipating heat energy. The X-ray emitting gas in clusters in normal circumstances is expected to cool and contract, flowing towards the centre of the ICM (Cowie and Binney, 1977; Fabian and Nulsen, 1977; Mathews and Bregman, 1978). Continuous injection of energy by powerful radio galaxies could therefore give a solution. Evidence for this energetic impact by radio galaxies has been given by the existence of X-ray 'cavities' in the cluster medium (Hardcastle et al., 1998)—regions of low thermal X-ray emission at the positions of the radio lobes implying that work has been done by the lobes in the ICM.

Traditionally, FR-I radio galaxies have been perceived to be more important in off-setting cluster-cooling due to their ubiquity in these 'cool-core' clusters (Cavagnolo et al., 2008), and also that FR-IIs in nearby clusters where shocks can be easily detected are less common than FR-Is. Studying shocks around FR-II radio galaxies can be important for other reasons however, as they enable direct measurements of inverse-Compton detections, which in the past have concluded that their lobes are in general pressure-balanced with their environment (which is actually a minimum condition for expanding lobes) without requiring a significant fraction of protons in their lobes (Croston et al., 2005b; Kataoka and Stawarz, 2005). This is in contrast to the lobes of FR-Is, which may need a significant fraction of protons in their lobes/jets for pressure balance (Croston et al., 2008). In rich-clusters however, there has been evidence to suggest that FR-II's may in fact need a significant contribution of protons in their lobes (Belsole et al., 2007; Hardcastle and Croston, 2010), suggesting that the environment of an FR-II radio galaxy has a relationship with the particle content in its lobes.

In particular, the cluster shock surrounding the powerful radio galaxy 3C444 observed with *Chandra* has given important constraints on the energetics of the source—the pdV work done by the lobes of 3C444 on its environment is shown to be an underestimate of the total energy injected by the radio galaxy

(Croston et al., 2011) due to the added role of shock heating. Results such as these, if robust, can then be incorporated with simulations of realistic cluster environments to demonstrate the effect of a powerful radio galaxy.

Studying the dynamics of these shocks are therefore vital to understand the role that radio galaxies play in the evolution of the ICM, and this requires deep X-ray observations of the cluster coupled with high-resolution radio observations of a powerful radio galaxy driving the shock, as obtained for 3C444. On a much smaller scale however, radio galaxies can also play a role in the overall evolution of the host galaxy through AGN feedback, as explained in the following section.

1.4.4 AGN feedback models

The process of AGN feedback describes how the cold gas material in a galaxy, which is used eventually for star formation as the gas contracts, feeds and triggers the onset of AGN activity via accretion. Consequent powerful jets then heat the remaining cold gas, thereby suppressing star formation and regulating the growth of massive galaxies. This is the so called 'radio mode' feedback model, suggested by Croton et al. (2006). Direct observations in support of this are scarce, and therefore analytical models provide the best solution to match with observational data for star formation rates. Other models for star formation suppression in galaxies in the past have often proved inconclusive, such as supernova feedback mechanisms where the energetic input was deemed insufficient to offset gas cooling (White and Frenk, 1991). Powerful radio galaxies with jets therefore could provide the cooling disruption necessary to explain star formation suppression in galactic disks (Kennicutt, 1989) including massive elliptical galaxies, where FR-II sources are mainly observed.

Other AGN feedback models include the 'Quasar mode'—where a galaxy merger can disrupt the bulge gas in a galaxy or directly deposit gas to the AGN, triggering AGN activity (Croton et al., 2006; Wylezalek and Zakamska, 2016). However, the radio mode feedback mechanism has been more widely accepted due to its ability to self-regulate growth in massive galaxies, whereas the quasar mode feedback is far less understood. For these feedback models it is of utmost importance that the power injected by radio galaxies is understood out to high-redshift, and therefore jet powers are crucial parameters in studies of powerful radio galaxies. I return to this vital point in Sections 1.7 and 1.8.

1.5 Relativistic Beaming and Superluminal motion

So far I have described the physics of radio galaxies on the assumption that they launch twin jets of radiation either side of the nucleus in the plane of the sky. In many cases however, particularly if one

side of the radio galaxy is inclined towards the line of sight, only a single jet is observed or that one of the jets is many times fainter than the other. This may be due to what is known as *Relativistic* or *Doppler beaming*, which arises due to the relativistic nature of the jets. Furthermore, a remarkable feature has been observed extensively where the some parts of the emission from the jets are shown to move at speeds greater than the speed of light, known as *superluminal motion*. This was proposed theoretically by Martin Rees (Rees, 1966), and can in fact be readily observed by modern day telescopes. Particularly for the radio galaxy 3C345, VLBI observations have shown that there are apparent 'blobs' of emission in the jet travelling away from the core at a speed of $\sim$ 14c (Bartel et al., 1986).

The peculiar phenomenon of superluminal motion can be explained using simple geometric arguments. Assuming that the jet is inclined at a large angle from the plane of the sky, so that the jet is almost inclined towards the observer, and that the blobs of emission are travelling at $v \approx c$, then the apparent separation velocity of the blob is given by

$$v_{sep} = \frac{v \sin\theta}{1 - \frac{v}{c}\cos\theta} \tag{1.19}$$

where v is the true speed of the blob and θ is the angle to the observers line of sight. For example, if the blob of jet emission has speed $v = 0.9c$ and the jet is inclined at $\theta = 10\,\text{deg}$ to the line of sight, then $v_{sep} = 1.37c$.

If we assume that all radio galaxies do indeed have double jets then the apparent observation of single sided jets can be explained by the phenomenon of *relativistic beaming*. Since the blobs in the jet are relativistic, the emission flux is affected by special relativistic considerations such as the Doppler factor. This results in the observed emission flux being boosted relative to the actual emission in the rest frame by a factor

$$D = \frac{1}{\gamma(1 - \frac{v}{c}\cos\theta)} \tag{1.20}$$

where γ is the Lorentz factor. Further factors of this Doppler factor are multiplied to the observed emission to consider the fact that the solid angle subtended by the radiation is different in the observed and emitted frames. Therefore, the emission from a relativistic blob from a jet inclined towards the line of sight is 'boosted' in flux. A blob from the opposite jet is receding and is therefore reduced in flux by the same factor. This gives the apparent nature of one-sided jets—since we cannot 'see' the other jet due to the approaching jet being boosted and the receding jet being stagnated in flux. Standard values for the angle to the line of sight and the speed of the jet can give a ratio of $\sim 10^4$ between the approaching and receding jet. High dynamic range radio imaging by modern day telescopes therefore becomes vital in the study of extended structure AGN such as radio galaxies. [2]

[2]Note that, these so called beaming effects should not be confused with dust obscuration—emission from the jet on the parsec scale that is obscured by the 'dusty torus' around an AGN through the line of sight.

The idea that AGN with one-sided jets are only apparent and actually do contain double jets due to the angle to the line of sight and relativistic considerations points to a more 'unified' approach—that *all* classes of AGN do in fact contain double jets and not just radio galaxies. This unification picture—where all classes of AGN are the same class which are all observed at varying angles to the line of sight is discussed below in Section 1.6.

1.6 Unification Schemes

As explained above, superluminal motion or beaming effects are only taken into account for objects at small angles to the line of sight, such that one of the jets is approaching the observer and the other receding. For very small angles, where the jet is almost directly beamed towards the observer, it would be difficult to distinguish between the approaching jet and the host galaxy, where the jet may completely dominate the emission. In these cases, one would observe the AGN as the known compact structures—quasars. Therefore the problem lies in that observed AGN could pose as any class from Blazars to extended double radio galaxies, depending on the jet orientation. A true double radio galaxy that is more inclined to the line of sight than the plane of the sky could appear to have only a single jet and show superluminal motion.

This argument was considered by Peter Barthel who, in 1989, produced a picture where all observed quasars are AGN that are beamed towards the observer and double radio galaxies are AGN that lie more in the plane of the sky, consequently not showing beaming—that the jet orientation is the reason for observing different characteristics of AGN (Barthel, 1989). This was particularly promoted by Barthel regarding radio-loud quasars and FR-II radio galaxies—the former is the same source just oriented close to the line of sight. This unification picture also included an optically thick 'dusty torus' regime, where a dense molecular torus formed from the material in the host galaxy surrounds the central AGN and obscures photons from the central nuclei. Therefore, some radiation can be more or less obscured for the observer depending upto the viewing angle—see Figure 1.3.

There has been some direct evidence for these tori obscuring radiation from an AGN, particularly for NGC 1068 where mid-infrared observations have spatially resolved a 'warm' dust structure surrounding a smaller, hotter nucleus (Jaffe et al., 2004). This dusty torus could also explain the observed distinction between Seyfert 1 (broad-line) and Seyfert 2 (narrow-line) objects. Those objects where the core can be observed directly in the line of sight are associated with Seyfert 1s whereas if the dusty torus shields the inner core due to our viewing angle then the broad lines are hidden and narrow emission lines are seen (see Figure 1.3). Although the basic unification picture regarded FR-II radio galaxies and radio-loud quasars as the same type of object, it could not explain why some AGN form FR-I's and some form FR-II's. As explained in Section 1.4, the environment could play a role with FR-I's having lower jet

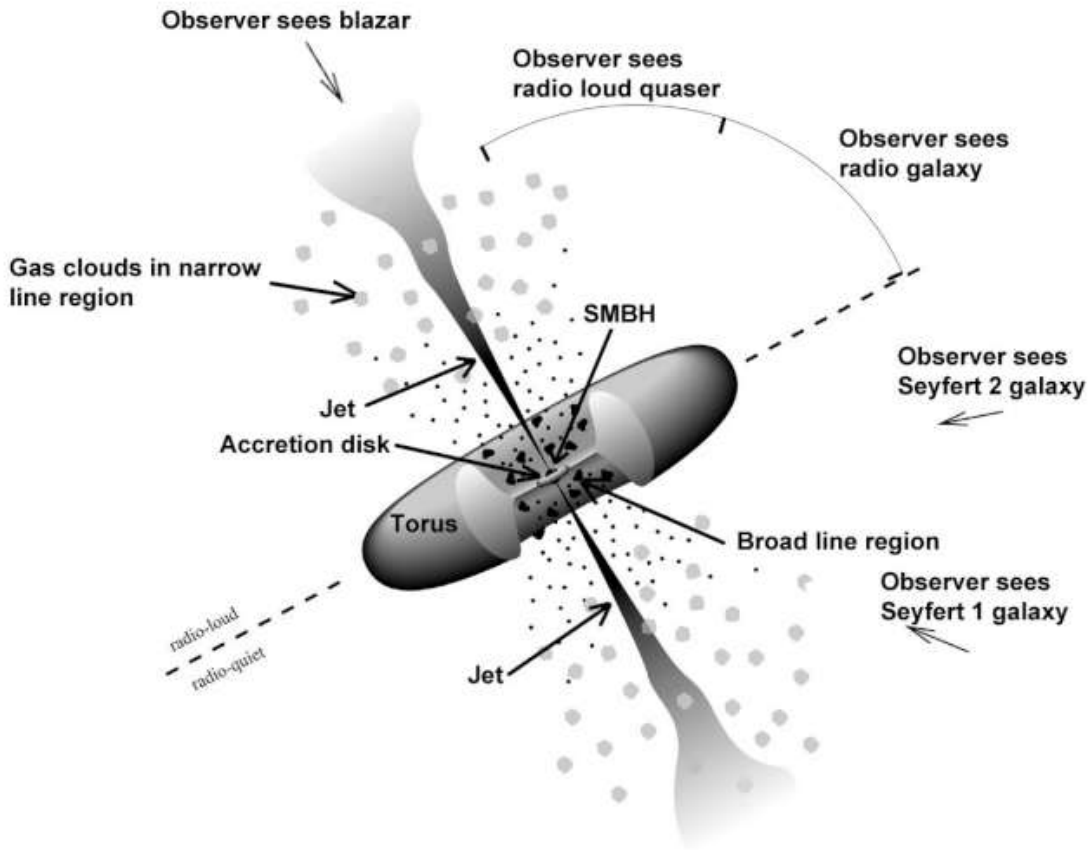

FIGURE 1.3: The basic unification picture, showing that the different classes of AGN can be shown to be variations of a single theme: a central accretion powered nucleus surrounded by a dusty torus of molecular gas, and jets emerging either side of the nucleus.

speeds and generally existing in rich cluster environments. Nevertheless there is currently much support in favour of unification models, and extensive work has been done in providing robust evidence for these models (Antonucci (1993); Urry and Padovani (1995); Elitzur and Shlosman (2006); Siebenmorgen et al. (2005); also see the review by Netzer (2015)).

1.7 Spectral Ageing

Radio observations have provided a useful means of probing the physics of the jets and lobes of radio galaxies. Of most importance is determining their energetics, and the jet power is a useful quantification of the rate of energy transfer to their environment. A crucial parameter in calculating the jet power of a radio galaxy is its age, and therefore the age of the radio source itself must be calculated as accurately as possible.

A useful tool that can been used to determine the ages of radio sources is *spectral ageing*. The spectral age is defined as the time taken for an electron in the lobes to radiate its energy through synchrotron

and inverse-Compton losses. When electrons get left behind as the hotspot advances and they fill the lobes, they are no longer being shock-accelerated and therefore go through radiative losses—with the higher energy electrons losing energy faster. This is evident by the curvature of the spectra of the lobes at high frequencies (Figure 1.5), and is characterised by the observed 'break' or turnover frequency in the synchrotron spectrum, past which the flux rapidly declines due to these losses. The spectral age, relating this break frequency and the magnetic fields present, is given by

$$t_{spec} = 2.6 \times 10^4 \frac{B^{1/2}}{B^2 + B_{CMB}^2} ((1+z)\nu_b)^{-1/2} \tag{1.21}$$

where B is the magnetic field in the lobe plasma, B_{CMB} is the magnetic field in the cosmic microwave background and ν_b is the break frequency (van der Laan and Perola, 1969).

Spectral ageing therefore uses the spectral break frequency and the magnetic field of the lobes of radio galaxies to determine its age. The spectrum of the lobes can be obtained by taking broad-bandwidth and high resolution data of a radio galaxy showing a clear lobe structure at radio frequencies. The physical interpretation of the break frequency is explained by a model where the lobes are adiabatically expanding and the hotspot advancing due to the jet continuously injecting the hotspot with 'new' electrons (Alexander, 1987; Carilli et al., 1991a). The electrons then 'age' in the lobes and therefore, an initial distribution of electrons at the hotspots described by a power-law would show a spectral break at later times after which the spectrum rapidly declines due to radiative losses. Determining the spectral age of the oldest electrons in the lobes therefore gives an accurate representation of how long the radio galaxy has been active. This connection between the radio spectrum and age of a radio source therefore became a powerful tool to determine source ages, and has been used extensively in the past (Burch, 1979; Alexander, 1985, 1987; Alexander and Leahy, 1987; Carilli et al., 1991a).

We know that the brightest points of an FR-II radio galaxy are the hotspots and therefore they coincide with the peak flux emission in a radio spectrum of the lobes. The observed decrease in flux must therefore happen in the lobes, as mentioned above. The physical interpretation of the flux decreasing at higher and higher frequencies is due to the nature of synchrotron radiation, where the higher energy electrons are depleted first, as is seen from Equation 1.6. As well as this there are also losses due to the adiabatic expansion of the lobes and inverse-Compton losses as electrons can lose energy by scattering photons external to the radio source to higher energies.

Radio galaxies are in a constant state of competition between energy injection by the jets and energy losses, and these high-energy processes play a crucial role in determining the age of a radio galaxy.

1.7.1 The physics of spectral ageing

Spectra of the lobes of radio galaxies have given insight into remarkable features and processes that determine their age (Hargrave and Ryle, 1974; Alexander, 1985, 1987; Carilli et al., 1991a). As shown in the spectral index map of 3C35, Figure 1.4, a spectral 'flattening' at the hotspots is observed, with a spectral index of around 0.5. This means that, at the hotspots, the flux is slowly decreasing with frequency with a gradient of 0.5 on a logarithmic plot of the spectrum. This is therefore the observed power-law spectrum of the hotspots associated with particle acceleration, and usually occurs at low GHz frequencies or even high MHz frequencies. Further from the hotspots, towards the core of the radio galaxy, the spectral index rapidly progresses to higher values, reaching values 2.0 or higher towards the base of the lobes. This spectral steepening in the lobes is characteristic of powerful radio galaxies emitting via the synchrotron process.

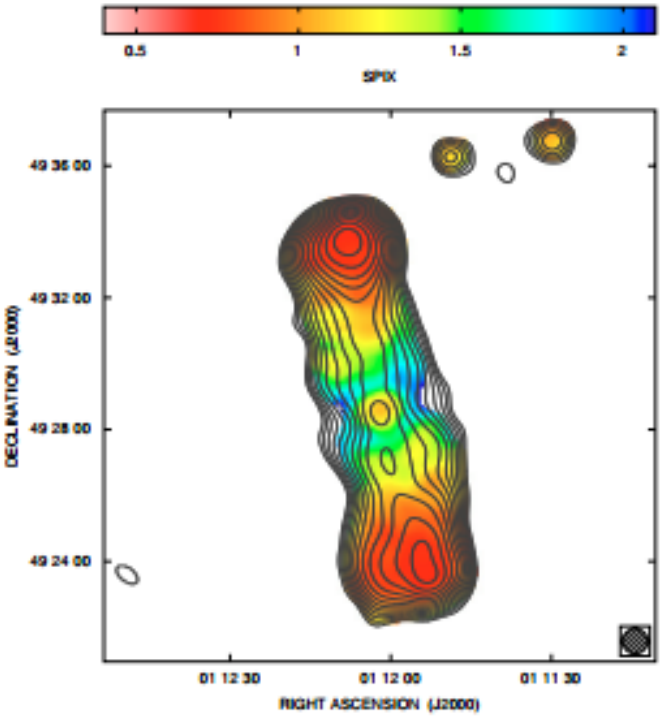

FIGURE 1.4: Spectral index map of 3C35 taken between 327 MHz and 1.4 GHz using the VLA (Condon et al., 1998; Orrù et al., 2010)

As given by Equation 1.6, the synchrotron radiation loss scales with time as (assuming constant magnetic field)

$$\frac{dE}{dt} = -aE^2 \tag{1.22}$$

where I have replaced the γ factor with E, the electron energy (since $E = \gamma m_e c^2$ and therefore $E \propto \gamma$). The characteristic time for this loss is then

$$\tau = \frac{E}{-\frac{dE}{dt}} = \frac{1}{-aE}. \tag{1.23}$$

Therefore, the highest energy electrons in the lobes are depleted first as mentioned previously. This leads to a progressive steepening of the spectrum at higher and higher frequencies, since in the lobes there is less flux from higher energy electrons as some of them would have already radiated their synchrotron radiation before the lower energy electrons. Spectral ageing models showing this high frequency spectral curvature due to radiative losses are shown in Figure 1.5.

The spectral age of a source can be recovered by fitting spectral ageing models to observed spectra. The process of obtaining observational data for FRII radio galaxies, fitting spectral ageing models to those maps and recovering source parameters such as spectral age and jet power has now become a common method of inferring the dynamics of these powerful radio sources (Harwood et al., 2013, 2015). A brief overview of contemporary spectral ageing models is given below.

1.7.1.1 Spectral Ageing Models

There are several models that describe the spectra of the lobes of powerful radio galaxies. They essentially describe the synchrotron emission from relativistic electrons traversing in magnetic fields initially from the hotspot down to the lobes where radiative losses occur, given by the emissivity of synchrotron radiation $J(\nu)$ in Equation 1.8. These models are briefly described below.

Using the standard synchrotron equations (Longair, 2011), the emissivity for a particular spectral ageing model can be given as (Harwood et al., 2013)

$$S_{model}(\nu) = \frac{\sqrt{3}e^3 B}{8\pi\varepsilon_o c m_e} \int_0^{\pi/2} \int_{E_{min}}^{E_{max}} F(x) \frac{1}{2} \sin^2\alpha N(E) dE d\alpha \tag{1.24}$$

and is therefore a function of the energy distribution of the relativistic electrons $N(E)$, given by

$$N(E) = N_0 E^{-2\alpha+1} (1-\beta)^{(2\alpha+1)-2}, \tag{1.25}$$

using the standard synchrotron loss theory (Section 1.3). The first terms on the right hand side, $N_0 E^{-2\alpha+1}$, represent the initial power-law form for the energy distribution at the hotspots, as was used to derive Equation 1.10. The remaining term $\beta^{(2\alpha+1)-2}$ represents the time-dependent energy losses at higher frequencies.

The two most widely used spectral ageing models that describe these losses in the lobes are the Kardashev-Pacholczyk (KP) model (1970) and the Jaffe-Perola (JP) model (1973). These two models differ in the β term from Equation 1.25, as described below:

- Kardashev-Pacholczyk (KP): Assumes the pitch angle of any given electron with respect to a fixed magnetic field is isotropic and constant over its radiative lifetime. The β term in Equation 1.25 for the energy distribution of electrons for the KP model goes as $\beta_{KP} \propto EB^2 \left(\sin^2 \alpha\right) t$, where E is the electron energy, B is the constant magnetic field and t is the time since initial acceleration.
- Jaffe-Perola (JP): Assumes the pitch angle is isotropic only on short time scales. Therefore the JP model instead uses a time-averaged value of the pitch angle of the electrons with respect to a fixed magnetic field in the lobe, where $\beta_{JP} \propto EB^2 \langle \sin^2 \alpha \rangle t$.

Exemplar KP and JP model spectra are given in Figure 1.5, and a more detailed description of these models is given in Leahy (1991).

Although the JP and KP models provide a reasonable description for the energies of the ageing electron population in the lobes of radio galaxies, they assume a fixed magnetic field strength throughout the source. This may be unlikely for structure on large scales such as radio galaxies where inhomogenieties may be common (e.g. Stawarz et al. (2013)). Furthermore, inverse-Compton measurements in the lobes of Pictor A have suggested that the magnetic field may vary on large spatial scales (Hardcastle and Croston, 2005). Tribble (1993) therefore proposed an ageing model, based on the standard JP losses, with instead a Gaussian random magnetic field. This allows a spatially non-uniform magnetic field in which the electrons age. The emission is then similar to Equation 1.25 with the JP losses and integrated over a Maxwell-Boltzmann distribution (Hardcastle, 2013), giving

$$S_{\text{Tribble}}(\nu) = \frac{\sqrt{3}e^3 B N_0}{8\pi\varepsilon_o c m_e} \int_0^{\infty} \int_0^{\pi/2} \int_{E_{min}}^{E_{max}} BF(x) \frac{1}{2} \sin^2 \alpha E^{(-2\alpha+1)} (1-\beta_{JP})^{(2\alpha+1)-2} \frac{B^3 \exp(-B^2/2B_0^2)}{B_0^3} dE d\alpha dB, \tag{1.26}$$

where B_0 is the mean magnetic field strength.

The idea is to, as explained above, fit the lobe fluxes of these models to the those from the observed data giving a best fitting spectrum for the lobes. The age, as given by Equation 1.21, that corresponds to the best fitting spectral model can then be recovered, as is explained in Section 2.5. We therefore need to observe broad-bandwidth radio data in order to constrain the flux at a broad range of frequencies, particularly at the higher frequencies where the spectral curvature/ageing is apparent.

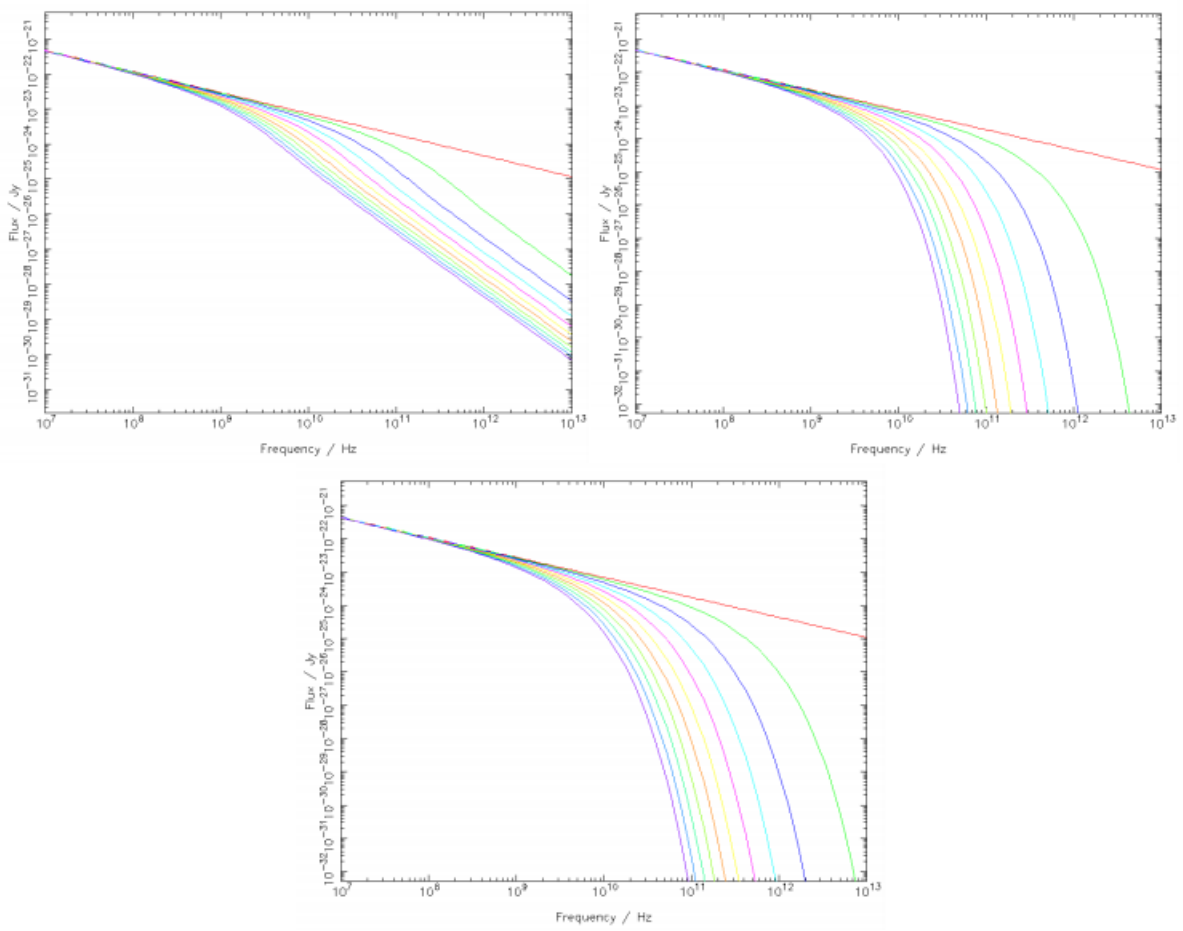

FIGURE 1.5: Synchrotron spectra of spectral ageing models for different spectral ages:KP (top left), JP (top right) and Tribble (bottom) between 10MHz and 10THz with injection index of 0.6. Each plot shows model ages between 0 (red) and 10 (purple) megayears (Harwood et al., 2013).

1.7.2 Problems with spectral ageing

The first observation of radio spectral index steepening in the lobes of FRII radio galaxies was published by Mitton and Ryle (Mitton and Ryle, 1969). However even today, after the advance in methods (Harwood et al., 2013) and instrumentation, there still remain concerns over the reliability of derived ages. The causes of these are listed as below:

- A major assumption made regarding spectral ageing models of the lobes of powerful FRII radio galaxies is the slope of the initial power law of its spectrum at low frequencies (during particle acceleration), which is governed by the injection index of the electron energy distribution α_{in}. Observations of hotspots have given values of around 0.5 to 0.6 (Meisenheimer et al., 1989; Carilli et al., 1991b)—and this is actually expected from shock theory (Longair, 2011). However, recent analysis of the lobes of FRII radio galaxies (Harwood et al., 2013, 2015) have yielded values of around 0.8. It therefore becomes apparent that further studies are needed to improve the robustness

of these findings to show whether this discrepancy is true for all FRII sources or simply a result of spectral analysis or uncertainties in the telescope observational data.

- Spectral ageing models such as those described in Sect 1.7.1 have been shown to produce varying results in model fitting. As shown by Harwood et al. (2013), out of the 3 models (JP, KP, Tribble), the JP model produces the highest χ^2 values whereas the KP model gives the lowest. On the other hand the JP model is more physically realistic than the KP due to its time-averaged pitch angle. Furthermore the Tribble model showed somewhat intermediate fitting results with a physically realistic description of the dynamics involved. Therefore the ideal model of choice when determining the age of radio galaxies is somewhat uncertain and further observational data is needed to draw more reliable conclusions.

- A significant problem in deriving the ages of these sources is the discrepancy between the ages derived from spectral age fitting and estimates of the dynamical age as inferred from X-ray observations. The dynamical age is given by the source lifetime as implied by a model of the lobe dynamics and the external environment of the source-i.e, using the lobe advance speed (see Sect 1.4.3). This disparity has been observed even when broad-bandwidth data at GHz frequencies have been used (Harwood et al., 2013, 2015). Spectral ages seem to be underestimated relative to their corresponding dynamical ages, and the investigations of causes for this disparity have been inconclusive (Eilek, 1996; Harwood et al., 2013, 2015). With the advent of the next generation radio interferometers such as the SKA, all radio-loud AGN will be identified out to high redshift. Deep and sensitive X-ray data, and therefore dynamical ages, will not necessarily be available for all of these sources and therefore it is essential therefore that spectral ageing methods yield reliable and accurate ages for the determination of jet powers. For current work, it is clear that low redshift sources with good enough X-ray data that clearly and reliably constrain the lobe dynamics, along with high resolution and broad-bandwidth radio data will need to be studied—these are the aims of the current project.

1.8 Project aims

This project is based on the use of broad-bandwidth radio and deep X-ray data to study the dynamics and energetics of radio galaxies, in order to probe the spectral age/dynamical age problem. The first half of the project is concerned with determining the spectral age of FR-II radio galaxies, since this is a crucial parameter in calculating the jet power of the source. The second half is concerned with dynamical age calculations in order to compare the derived spectral ages with dynamical ages—which we generally assume give the most reliable ages. I also discuss implications for the dynamics and energetics of the observed sources in the context of powerful radio galaxies in rich environments, in terms of the power output of the source and other derived parameters. The jet power is one of the most important parameters in AGN studies and is vital that they are derived accurately using spectral ageing, so that spectral ages

and jet powers of all radio loud AGN at high redshifts can be confidently derived, as will be observed using future instruments (Chapter 4).

The aims of this project are therefore to:

- Carry out the data reduction for the observed JVLA data of the proposed FR-II sources (3C444 and 3C320—discussed in Sect 2.1), producing high-fidelity broad-bandwidth radio maps of the sources.
- Use the images as flux data points for spectral analysis by fitting with spectral ageing models, as explained in Section 2.5. For the best fitting models the spectral age and the physical interpretation of the model can be tested against other worse fitting models.
- For the fitted spectral ages, check for discrepancies with dynamical ages of the same sources using corresponding X-ray data. The dynamical age will be calculated by analysis of the *Chandra* X-ray data available for the rich clusters surrounding 3C320 and 3C444, and analysing the shock properties (if a shock is seen at all in the X-ray).
- Calculate the jet power of the observed sources using derived ages, and interpret the results in the context of the dynamics of powerful radio galaxies in rich cluster environments. Other constrains such as lobe pressure-balance and magnetic field strengths will also be tested against previous studies on radio galaxies.

The results that will follow from this project will add further robustness in past work on FR-II sources and I aim to minimise the existing problems outlined in this section. The final section in this Chapter (Section 1.9) describes the two telescopes used in this project, as well as VLBI techniques on which extensive work in the past has been based. Chapter 2 presents the analysis of the dynamics and energetics of the two FR-II sources studied in this project, and a thorough discussion of the results is given in Chapter 3. I summarise my main findings in Chapter 4, and conclude with a brief outlook on future work in this field.

1.9 Telescopes and Interferometry

1.9.1 JVLA

The Karl G. Jansky Very Large Array (JVLA) telescope, located in New Mexico, is a 'radio interferometer'—meaning that it uses combinations of its 27 antennas to obtain the sky coverage. It is operated by the National Radio Astronomy Observatory (NRAO), and has an observable frequency range of 74 MHz to 50 GHz making it ideal for continuum observations over a broad frequency range (maximum bandwidth

of a single observation of 8 GHz). Each antenna is 25m in diameter, and the maximum diameter of the telescope is 36km.

Interferometers make use of multiple antennas to improve the resolution of the final radio maps. This is because the angular resolution goes as $\theta \approx \lambda/D$, where λ is the wavelength and D is the diameter of the dish and therefore very large diameters are needed to achieve the small resolution required. This can be provided by an interferometer by measuring the interference pattern between each pair of antennas in its array. The diameter is then the length of the longest *baseline*, which is the distance between the most separated pair of antennas in the array. The measured *visibilities* are related to the actual source structure, as seen in the radio maps in Figure 1.2, by a 2D Fourier transform (see Section 2.2). Note that the interferometer only measures 'samples' of the Fourier transform of the sky. This is because we cannot measure the complete sky everywhere, and therefore the observed data is only a sample of the complete sky coverage.

Deconvolution algorithms are then used to create an image of the source from the actual data (see Section 2.2.4). The JVLA's D-configuration is the most compact array for the antennas, which helps to observe large-scale, diffuse structure in the lobes of FR-II sources. The baselines can be expanded until the maximum distance in the A-configuration, giving information about compact structures such as hotspots that require high-resolution observations. The combination of observed data from multiple array-configurations to sample both small and large-scale structure of a source has enabled high fidelity images of radio galaxies to be obtained for the past 35 years (e.g. Carilli and Harris (1996); Carilli et al. (1991a)).

1.9.2 VLBI techniques

Very Long Baseline Interferometry (VLBI) uses similar techniques for observing radio galaxies as the JVLA, however there are several arrays located in Europe, Canada, the US, Russia, Korea, Japan, Mexico and Australia. The European VLBI network (EVN) is the most sensitive of the arrays, while the Very Long Baseline Array (VLBA) in the US has the largest baselines and therefore highest resolution. The combination of these arrays from different countries therefore gives a much higher resolution than any other astronomical instrument in the world (resolution in the order of microseconds). Extensive work on AGN has made use of the high-resolution obtained by VLBI techniques to probe very small scale structures, revealing bright knots associated with jets and aiding studies on superluminal motion (Pearson and Readhead (1988); also see reviews by Zensus (1997) and Saikia and Salter (1988)).

1.9.3 Chandra

The Chandra X-ray observatory was launched in 1999 by *NASA*, as its flagship X-ray observatory. The spacecraft orbits above the Earth's atmosphere detecting X-rays from hot regions of the Universe, and allows high-resolution images at small scales (~ 0.5 arcsec) to be obtained.

The high-energy X-rays are focussed onto the focal plane by sensitive grazing incidence mirrors inside the spacecraft. This is due to the fact that the high energy X-rays can penetrate normal mirrors that are otherwise used in optical telescopes to reflect incoming photons for focussing. The science instruments associated with the detections in the focal plane can provide information on the counts, position, energy and the time of arrival of the X-rays, enabling high-resolution images to be formed. These are two instruments, namely the High Resolution Camera (HRC) and the Advanced CCD Imaging Spectrometer (ACIS). The other two instruments in the telescope, the HETGS and LETGS, are placed near the front of the telescope behind the mirrors which can then 'swing' into the optical path of the photons. These detectors are used for diffracting X-rays—and are dedicated to high resolution spectroscopy. A schematic view of the Chandra spacecraft is shown in Figure 1.6. The data reduction process for *Chandra* data is given in Section 2.6.2

Since hot X-ray detections are ubiquitous in AGN studies, *Chandra* has been used extensively in the past to study radio galaxies. Inverse-Compton and thermal X-ray measurements can be made (e.g. Croston et al. (2005b); Massaro et al. (2013); Mingo et al. (2014)) in order to study the dynamics and energetics of radio-loud AGN and their environment.

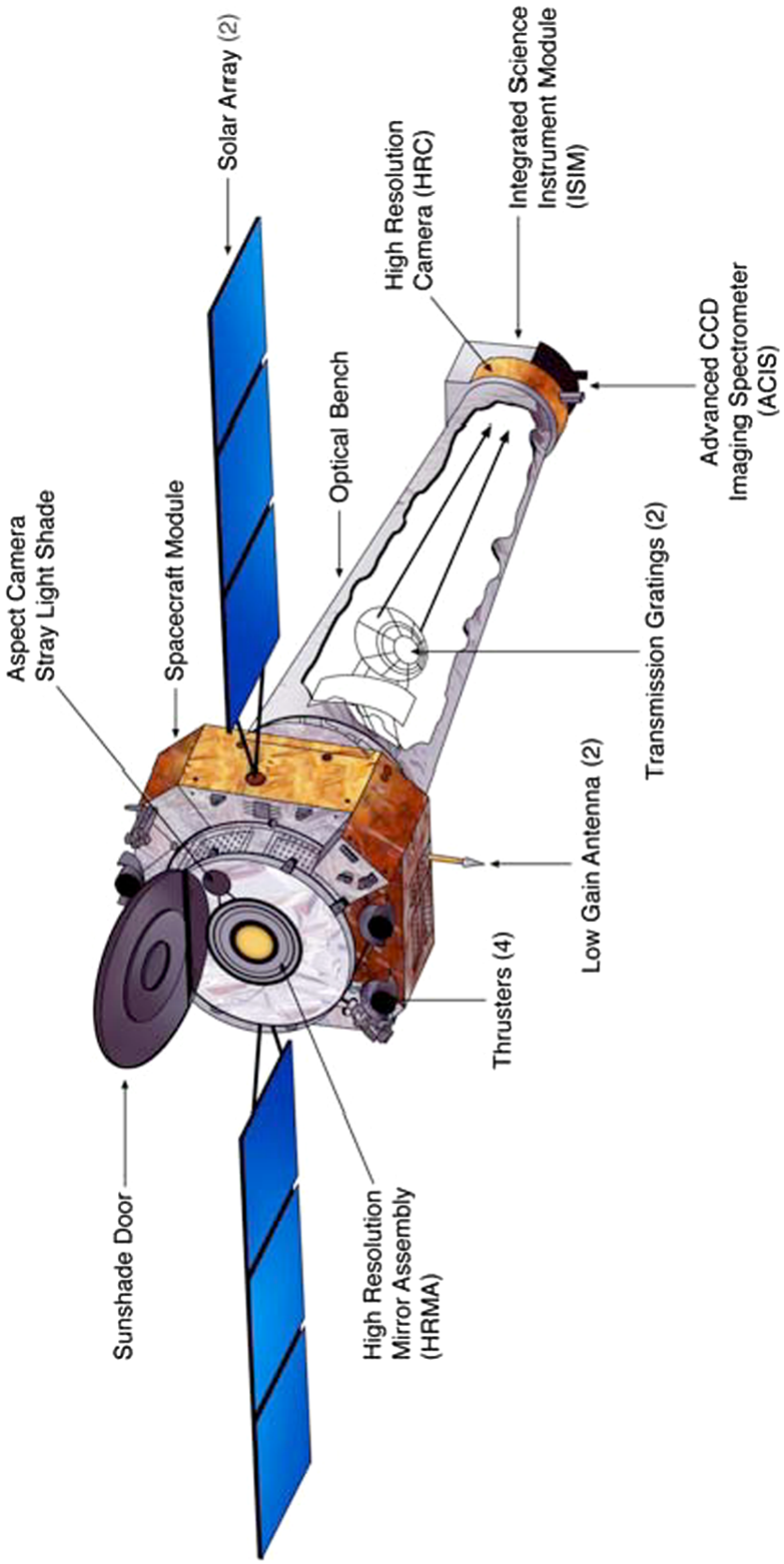

FIGURE 1.6: Schematic of the Chandra spacecraft.

FIGURE 1.7: Photo taken of the Jansky Very Large Array Telescope (JVLA) in New Mexico, USA. The configuration is in the D-array—the most compact (shortest baseline) configuration.

Chapter 2

Analysis

This chapter outlines the methodology, implementation and analysis techniques used to meet the aims of this project, as outlined in Section 1.8. In Section 2.1, I present the observational details of the two FR-II radio galaxies that were observed for this project. Following that section I describe and explain the data reduction methods used on the observed data sets. Section 2.3 presents the images obtained, followed by a description of the techniques used to determine the spectral ages of the two sources in Sections 2.4 and 2.5. In Sections 2.6 and 2.7 I describe the X-ray observations and analysis for 3C320. I then conclude in Section 2.8 outlining the full results obtained in regards to spectral and dynamical ages.

2.1 JVLA Observations

2.1.1 Source selection

In probing the spectral age/dynamical age problem, we implicitly assume that the dynamical ages are correct—in the sense that we obtain the age by directly probing their dynamics as given by their observations. Spectral ageing requires the careful extraction of the source spectra by obtaining fluxes at a broad range of frequencies and fitting them with spectral ageing models. Therefore, it is essential that for these studies we observe sources with well defined dynamics, such that we can trust their dynamical ages with a high degree of confidence. Then, with the best available radio maps across a broad frequency range, we may compare the spectral and dynamical ages and probe any discrepancies. To add to the complexity in choosing which sources to observe, the fact that not all radio galaxies with the best radio observations necessarily drive shocks in their external medium (and hence do not allow a direct calculation of dynamical age) means that the number of potential sources available to be observed is severely limited.

Two radio sources were selected for observation with the JVLA (for which ‘good’ existing radio data were previously unavailable) for spectral ageing studies, both of which are powerful FRII radio galaxies

TABLE 2.1: Information on observed JVLA targets—including the 178MHz luminosity and the largest angular size (LAS).

Source	z	Cluster kT (keV)	L_{178} $(W/Hz/sr)$	LAS (arcsec)	Size (kpc)
3C444	0.153	3.5	1×10^{26}	120	320
3C320	0.342	3.3	3×10^{26}	20	100

in cluster environments, namely 3C320 and 3C444 (Table 2.1). 3C320 is a low-redshift ($z = 0.342$) *brightest cluster galaxy* (BCG). This means that it has the highest surface brightness of all the galaxies in its cluster, lying in the (projected) centre of a cluster as has been detected in the X-ray (Massaro et al., 2013). 3C444 is also nearby ($z = 0.153$) (BCG) (Wyndham, 1965), with evidence for a strong shock being driven into its cluster environment (Croston et al., 2011). These targets were originally selected for potential radio follow-up observations from previous unbiased X-ray surveys of samples of powerful radio galaxies (Massaro et al., 2013; Mingo et al., 2014). The selection criteria were based on an identification of clear shock signatures in the X-ray, and the availability of X-ray data good enough to constrain the lobe dynamics. These sources have therefore been followed up by further deep *Chandra* X-ray observations which are used in this project to estimate their dynamical age—see Section 2.6.

2.1.2 Observation details

Both targets were observed at L-band (1-2 GHz) and C-band (4-8 GHz). With the JVLA's array configurations (see Section 1.9), the targets were observed in the A-configuration (longest baselines), B-configuration (shorter baselines) and C-configuration (even shorter baselines—3C444 only). Long baselines provide higher resolution than shorter baselines, while the shorter and more compact baselines provide more information on large scale structure, as explained in Section 1.9. The choice of which array configuration to use for observations at L or C-band is based on the resolution requirements of the source. Nearby sources often do not require the longest baseline observations as they are larger in angular size than sources that are further away that would require the longest baselines. Furthermore, since we require observations at L and C-band with the same resolution in order to produce spectral index maps, observations at different frequencies require different baselines. This is because the resolution $\theta \sim \lambda/D$, and therefore lower frequency (longer wavelength) L-band observations require longer baselines for a given resolution θ than C-band observations. The observation details are given in Table 2.2.

With its higher redshift of $z = 0.342$ and therefore smaller angular size than 3C444, observations of 3C320 required higher resolution than that of 3C444. Therefore this source was observed at L-band and C-band in the A-configuration. At shorter baselines (B-configuration) the source was observed in the C-band only—L-band frequencies in this array-configuration would give too low a resolution, such that fine scale structure in the lobes would be poorly resolved. However, higher resolution at L-band than that which the JVLA allows is still required in order to improve the sampling at these frequencies

TABLE 2.2: JVLA observation details of 3C320 and 3C444. The 'JVLA project ID' refers to the project name as used by NRAO. The 'Duration' refers to the approximate total observation time including all the calibrator sources.

Source	JVLA project ID	Array	Frequency band (GHz)	Observation date	Duration (hrs)	Flux Calibrator
3C320	15A-420	A	L, C	01/08/15	4	3C286
		B	C	15/02/15	1.5	
3C444	15A-420	A	L	18/06/15	3.5	3C48
		B	L, C	07/02/15	4	
		C	C	31/01/16	1.5	

to include as much small-scale structure as possible. I therefore submitted a proposal for 3C320's L-band data with e-MERLIN—which has much longer baselines available for observations. This proposal was later accepted, and I am currently waiting for the observation to take place. When this data becomes available, they will be reduced and combined with the JVLA A-configuration data to yield well sampled, and therefore high fidelity images of 3C320 at L-band. For 3C444, with its larger angular extent, L-band frequencies were sampled in the A and B-configuration. At C-band, observations were made at B and C-configuration. A visual representation of the sampling of the JVLA at the A and B-configuration is shown for 3C444 in Figure 2.1.

The JVLA observations are available in a format known as a *measurement set* (MS). In this format, the MS is used as a directory, and the data and metadata such as the visibilities, antennae information, weather etc. are stored in tables and subdirectories within the main directory. Each MS obtained, one for each array configuration at L and C-band, was reduced and imaged—see Sections 2.2 and 2.3. The observational data in the different array-configurations were then combined to produce well sampled maps at L and C-band. For example, for 3C444 at L-band, both A and B-configuration MSs were reduced individually, and then combined when imaging. The data reduction methods and processes are outlined below in Section 2.2.

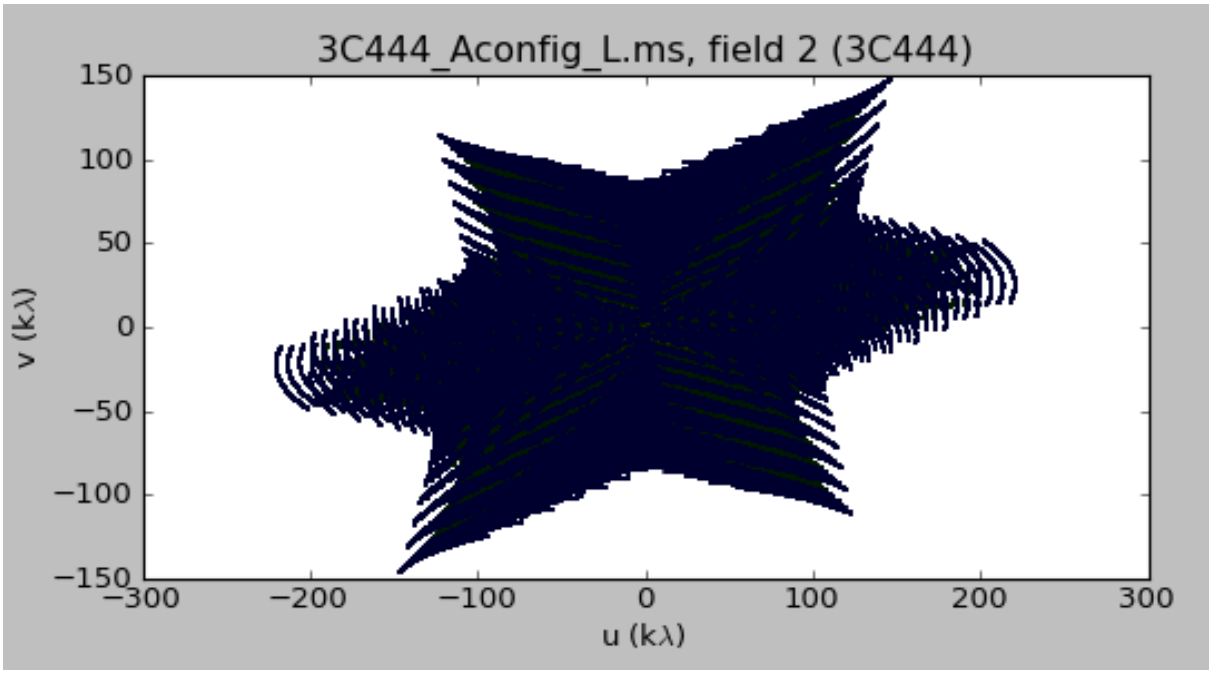

(A) 3C444 A-configuration L-band

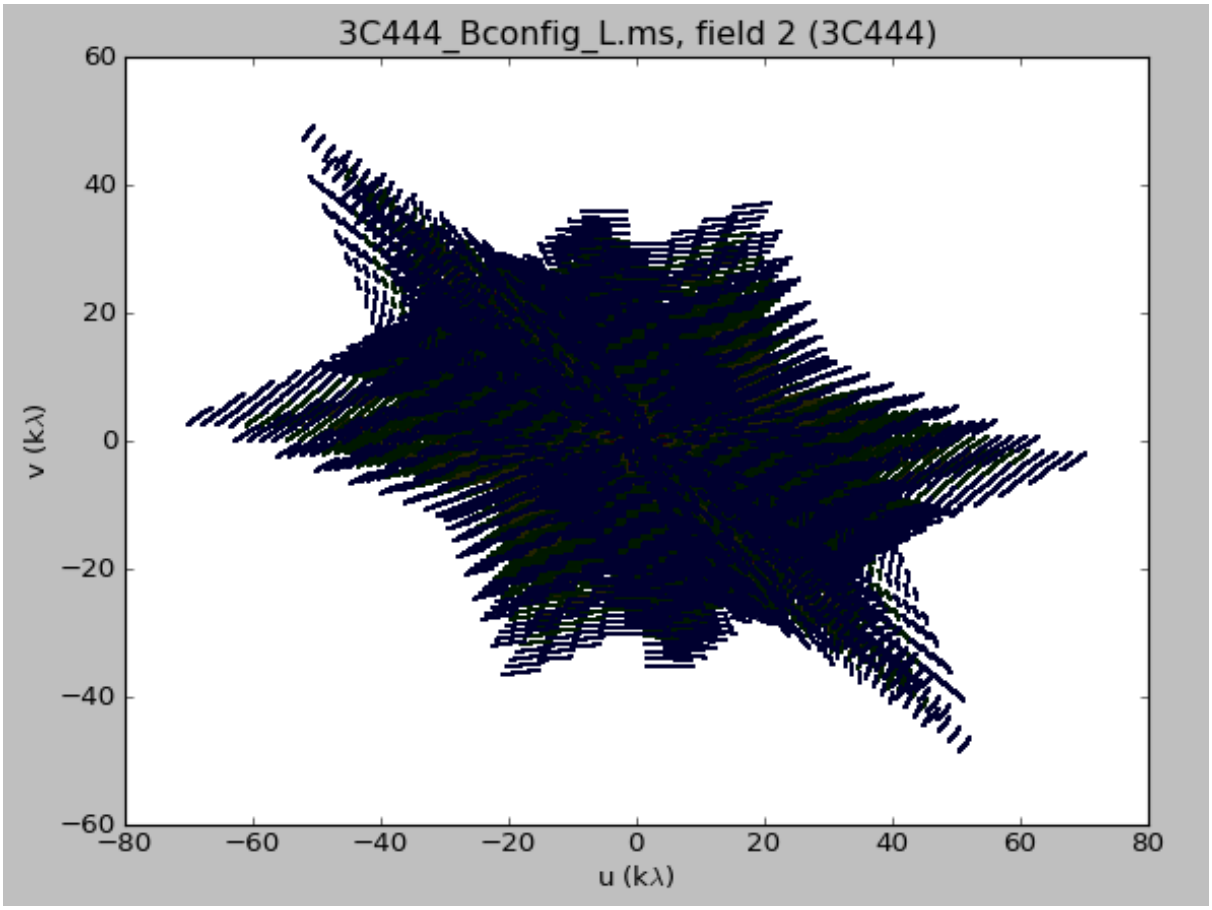

(B) 3C444 B-configuration L-band

FIGURE 2.1: Sampling of 3C444 at L-band with the JVLA: the x and y axes are the baseline vectors in wavelength units. Note the longer baselines for the A-configuration array.

2.2 Data Reduction

2.2.1 CASA

The CASA (Common Astronomy Software Application) package was developed primarily for the data reduction process of the next generation radio telescopes such as ALMA and the JVLA. The data reduction processes for the JVLA MSs have therefore been performed using CASA.

CASA operates under an iPython wrapped interface which allows the user to write a set of data-reduction tasks on the command line of a terminal. Therefore the data reduction tasks can either be executed as a set of manual commands, or through a python script which can be run as a regular python file on the interface. For the purposes of learning radio data reduction as a first experience, and since the targets are complex extended structures, I completed the data reduction process manually using step-by-step commands. As standard, the data-reduction process for radio data consists of data *flagging*, *calibration*, *deconvolution* and *self-calibration*—as described and explained in the proceeding sections. For the current work, CASA version 4.5.0 has been used, however note that the older version 4.3.1 was also used for some MSs that were reduced before version 4.5.0 became available to download.

2.2.2 Initial Flagging

The data sets observed are broad-bandwidth radio data at GHz frequencies (L and C-band). The initial stages of the data-reduction consisted of flagging any bad data. This could originate from a range of factors such as antennas with poorly known baseline positions at the time of observation that could not be calibrated, poor weather and radio frequency interference (RFI) from signals in Earth's atmosphere. Before calibration, I therefore used the 'AOFLAGGER' software package (Offringa et al., 2012) on all of the MSs to automatically flag RFI from the data. The data were then inspected using '$uv-$plots' of the measurement sets (a plot of the measured visibilities in amplitude against the baseline length) using the CASA command `plotms` to manually identify any remaining bad data. Baselines and/or antennae were flagged using the command `flagdata` prior to calibration. The identification of RFI in this way was based on anomalous spikes in the $uv-$data, although I also used the 'rflag' mode in the command `flagdata` to automatically flag outliers in the data.

Antennae with poor baseline positions were stated on the observers log which also informed of data lost by the antennae during the observing run as a result of technical faults. However, with most of the data reduction, known bad antennas stated in the observer's log were not flagged until poor solutions from those antennas appeared during calibration, in order to prevent the unnecessary flagging of potentially

good data.

The task `listobs` was then used which displays information on the particular measurement set such as basic observation information, scan times, spectral window information and antenna positions. Often the first scans of the observation, which are usually of the calibrator source, are used to configure the antennas or used as a test and are only a few seconds in duration. These scans were identified and flagged. Note that the flagging process occurs throughout the data reduction as more and more bad data are identified. Before producing an image, the $uv-$data were checked again for bad antennae or baselines.

2.2.3 Calibration

In general for radio interferometry, the observed visibility $V'_{i,j}$ for a pair of antennas i and j is related to the true visibility $V_{i,j}$ by

$$V'_{i,j}(u,v,f) = b_{ij}(t)\left[B_i(f,t)B_j^*(f,t)\right] g_i(t)g_j^*(t)V_{i,j}(u,v,f)e^{i\left[\theta_i(t)-\theta_j(t)\right]} \tag{2.1}$$

where u,v are the spatial baseline co-ordinates in frequency space, g_i and θ_i are the amplitude and phase complex gains of the antennas, B_i is the complex bandpass which is the instrumental response as a function of frequency f and $b(t)$ is the baseline term used to correct for recently updated antenna positions. The process of calibration is therefore to solve the above equation for the bandpass, amplitude and phase gains, which is possible if we also observe a source of known flux density—known as a calibrator source. The flux density values for the amplitude calibrators 3C286 and 3C48, for 3C320 and 3C444 respectively, were provided using the task `setjy`. Applying the calibration will then bring the observed visibilities as close as possible to the true visibilities.

The first stage of calibration consists of correcting the data for antenna elevation offsets and baseline positions, which may be inaccurate during the actual observation. The baseline position terms u,v need to be known as accurately as possible (as seen in Equation 2.1), and shortly after an array-configuration change the antenna positions corresponding to the visibilities $V(u,v)$ may then be slightly different during observation. Since NRAO monitors these baseline positions on a regular basis, the potential corrections to the antenna positions may be available after the observation has taken place. These corrections were found using the task `gencal` and used a set of latest known offset positions from the VLA baseline correction database are used to correct for this. The changes are output in the CASA logger, and the first calibration table is created automatically with the correction factors.

General calibration is then performed—part of which consists of an initial phase gain calibration which is used to 'weed' out bad data before bandpass (B_i) calibration. This is because there may be phase gain variations between different scans of the bandpass calibrator, particularly if the scans are at very different elevations. Therefore, the phase gains for the bandpass calibrator are derived, using the command `gaincal`, and stored in a calibration table. Extreme phase variations for any antennae were identified as showing suspicious behaviour for potential flagging, or flagged immediately.

Then, delay calibration is performed for the relative antenna-based delays, again using `gaincal`. After the phases have been calibrated, the complex bandpass B_i corrections can then be solved for using the task `bandpass`, using an observed bandpass calibrator which is usually a bright, flat-spectrum source at the observing frequency. Bandpass calibration is necessary since there may be frequency-dependent gain variations. For example different spectral windows may have slightly different amplitudes and phases as a function of frequency for an observed bandpass calibrator which should have constant amplitude.

Once the bandpass is solved, complex gain calibration (g_i and θ_i) is then performed using calibrator sources. The absolute magnitude of the gain amplitudes g_i are measured by observing a flux density calibrator (can be the same as the bandpass calibrator) and comparing the measured values with known values. In order to minimise atmospheric differences between the line of sight and the target source, the gain amplitudes of the phase calibrator (usually much closer to the target source) is also measured. The two sets of gain amplitudes are then compared using the task `fluxscale` to determine the absolute flux density scale which can then be appropriately used to determine the complex gains of the target source.

The phase gains θ_i are measured using the phase calibrator, which was also observed. A phase calibrator is usually a point source observed at the phase centre. The expected amplitude of the phase calibrator is therefore constant and the expected phase is zero. Therefore after the observation any non-zero phase difference between any two antennas must be due to the antennas themselves, and must be accounted for. This initial phase calibration was also done using the task `gaincal`.

For these JVLA observations, the flux density and bandpass calibrators used were 3C286 and 3C48, as stated in Table 2.2. Other calibrators such as J1602+33326 were used as amplitude and phase gain calibrators. The calibration tables produced were then applied on the target source using the task `applycal`. Prior to applying the calibration tables any sign of bad data such as extreme gain phases and variant amplitudes were flagged.

2.2.4 Deconvolution

After calibration the next step is to use a deconvolution algorithm to produce an image from the data. As explained previously, the interferometer measures the *uv* data (or complex visibilities) which are samples of the Fourier transform of the sky (measured in units called baseline vectors u and v), and is represented by

$$V'(u,v) = V(u,v)S(u,v) \tag{2.2}$$

where $V'(u,v)$ are the measured visibilities and $V(u,v)$ are the true visibilities. The term $S(u,v)$ represents the *uv coverage*, also called the *sampling function*. On the image plane this corresponds to the *dirty beam*. Taking the inverse Fourier transform of the measured complex visibilities $V'(u,v)$ from Equation 2.2 gives

$$\mathscr{F}^{-1}\left(V'(u,v)\right) = \mathscr{F}^{-1}\left(V(u,v)\right) \otimes \mathscr{F}^{-1}\left(S(u,v)\right), \tag{2.3}$$

by the properties of the convolution theorem. The next step is to deconvolve Equation 2.3 in order to get the real sky brightness distribution, which is $\mathscr{F}^{-1}\left(V(u,v)\right)$.

The most popular deconvolution algorithm used in recent decades is the Clean algorithm developed by Högbom (Högbom, 1974), which is available in CASA using the task `CLEAN`. `CLEAN` parameters such as `cellsize` and `imsize` were modified depending on the resolution of the data in the MS. It was ensured that, as a general rule of thumb, there were around 5 pixels per synthesized beam in the image.

2.2.5 Self-calibration

The calibration stage before imaging may be insufficient in many cases. The complex gains are derived from calibrator sources that are in different locations from the source where the troposphere and ionosphere can be variable, and hence may give unreliable gain solutions.

Therefore, instead of using a point source for calibration, self-calibration uses a model image of the source itself (produced by an initial clean) that is assumed to be a 'perfect' representation of the source. Here the model image is produced by CASA using `clean` and is a collection of the brightest points taken from the dirty map. The procedure then uses that model of the target source to solve for improved values for the complex gains of the individual antennas. Similar to Equation 2.1, the self-calibration equation then becomes

$$V_{i,j}^{'}(t) = g_i(t)g_j^*(t)e^{i[\theta_i(t)-\theta_j(t)]}V_{ij}^{model}(t) \tag{2.4}$$

where $V_{ij}^{model}(t)$ represents the visibilities of the model image of the source. The updated complex gains are then applied to the data, to produce a set of improved calibrated data. The level of improvement depends on the quality of the model—how well the model represents the true source. This process uses

the tasks `gaincal` and `applycal`. Another `CLEAN` from the newly calibrated data is performed to produce an improved image and consequently a new model for further self-calibration. This technique was applied mostly for the phase only complex gains. Amplitude self-calibration may be prone to errors due to potential flux deficiencies in the model image. Therefore, deriving amplitude solutions for the data based on the model may give incorrect complex gains. This is also true if off-source noise is added to the model image during cleaning. Caution was therefore taken with amplitude self-calibration, and it was made sure that the model image contained as much source flux as possible with a high signal to noise ratio. Antennas or baselines with relatively variant phase or amplitude gains were flagged. This procedure is performed iteratively until the calibration solutions converge-i.e. the phases are comparatively flat and do not get any flatter with more self-calibration iterations. All the measurement sets for 3C444 and 3C320 were self-calibrated in this project to varying iterations.

2.3 Total Intensity maps

The CASA data-reduction for 3C320 was performed for:A-configuration L and C-bands, and B-configuration C-band. The A and B-configuration C-band data were subsequently imaged together to produce a combined A+B-configuration image in the C-band. The combination of JVLA data of their configuration arrays is a common process in radio astronomy, since the added data further completes the sampling of the data in frequency space and gives the image small scale structure details (from A-configuration) and the more diffuse large scale structure (from B-configuration)—see Section 1.9. For 3C444 the images produced are at:A,B-configuration L-band and B,C-configuration C-band. Below I present the images obtained after the data reduction process of these two sources below. For all images the beam shape is shown in the bottom left-hand corner, and the colour scale for the flux on the right-hand side.

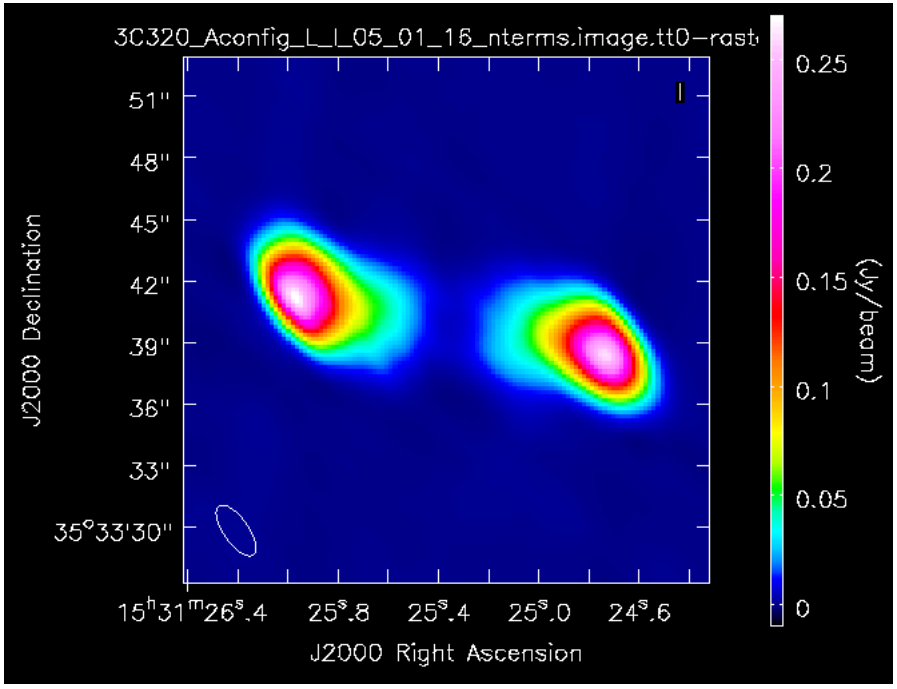

FIGURE 2.2: 3C320 A-configuration L-band map. Note the elongated elliptical beam size on the lower left by which CASA convolves the image. This beam is internally calculated by CASA and is based on the sampling of the source. This beam may have arisen due to the source being at a low elevation during the observation and therefore the sampling being sparse in a certain direction.

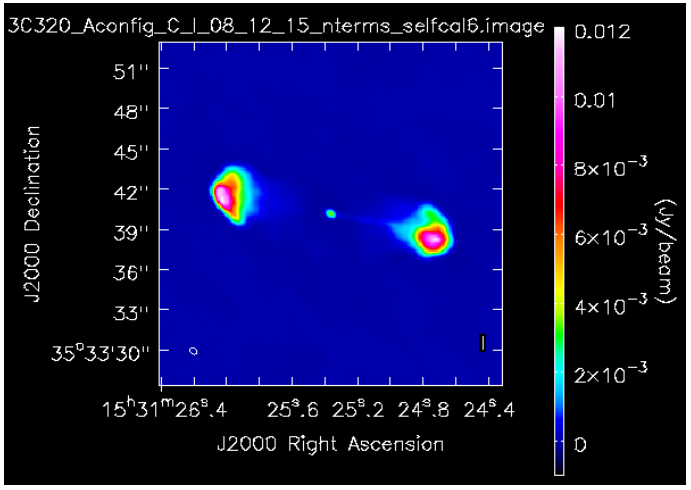

(a) A-configuration

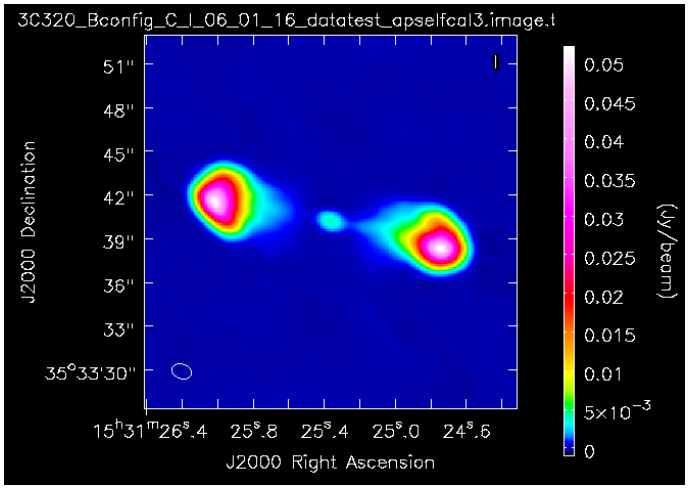

(b) B-configuration

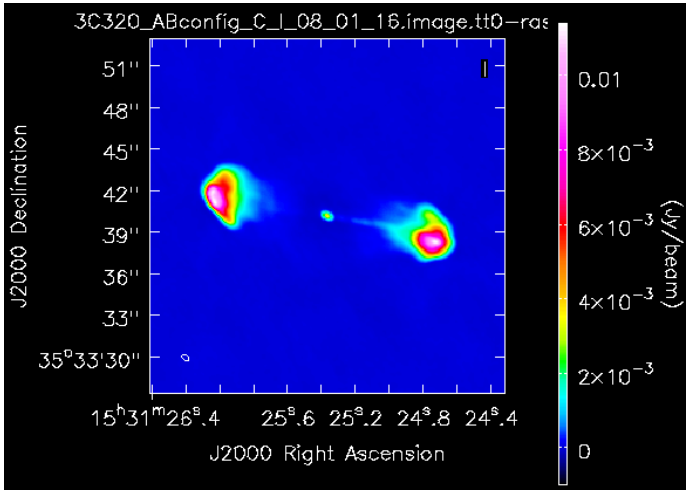

(c) A+B configuration

FIGURE 2.3: 3C320 C-band maps

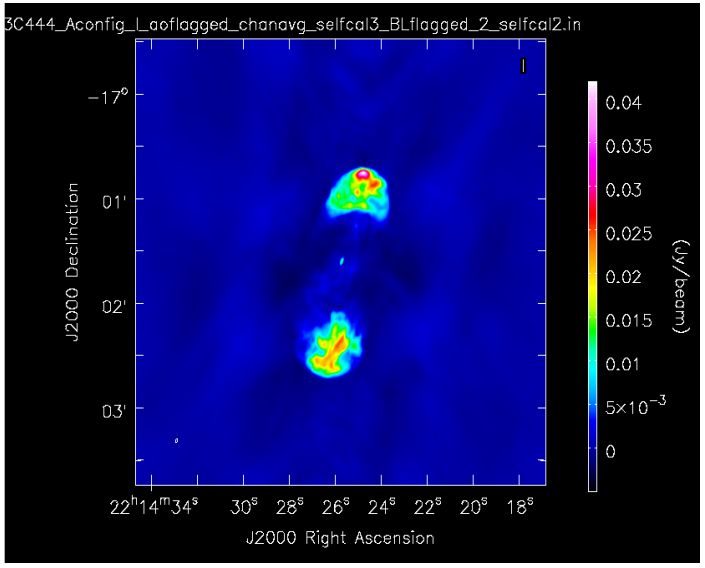

(a) A-configuration

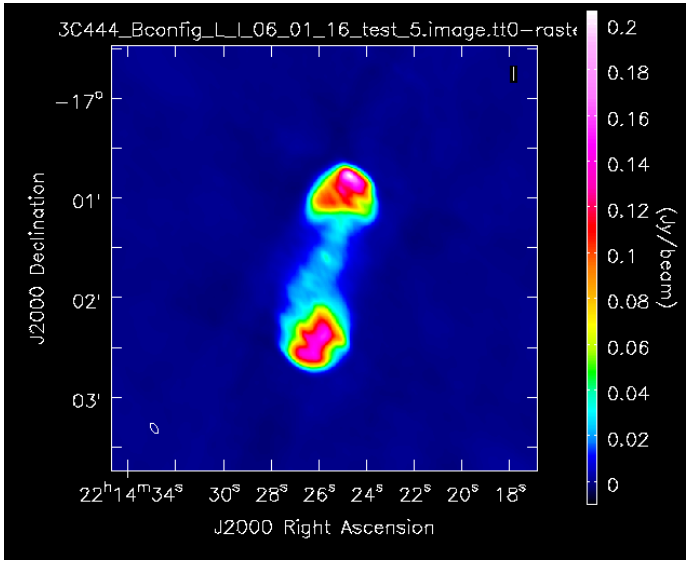

(b) B-configuration

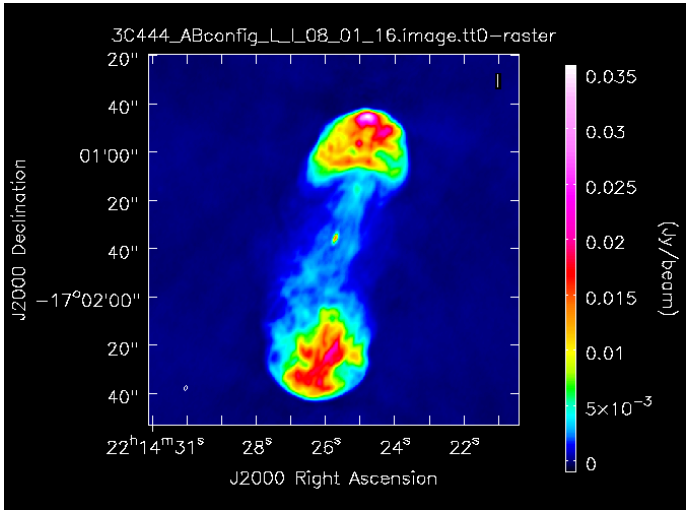

(c) A+B configuration

FIGURE 2.4: 3C444 L-band maps

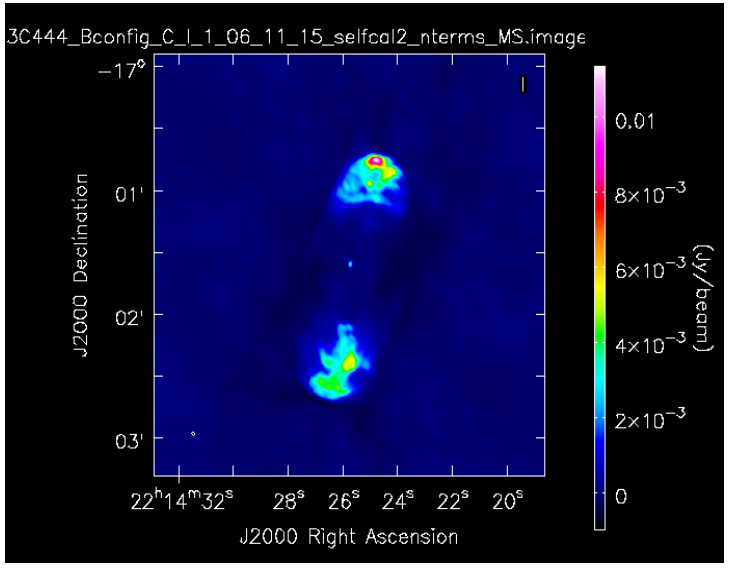

(a) B-configuration

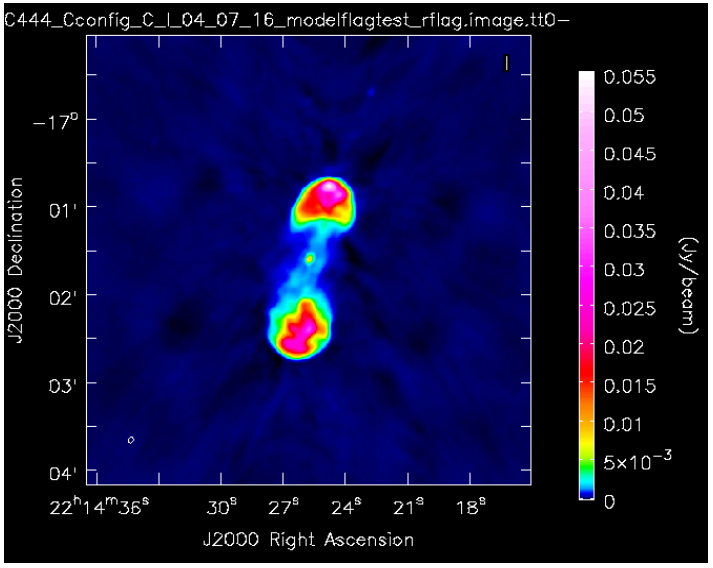

(b) C-configuration

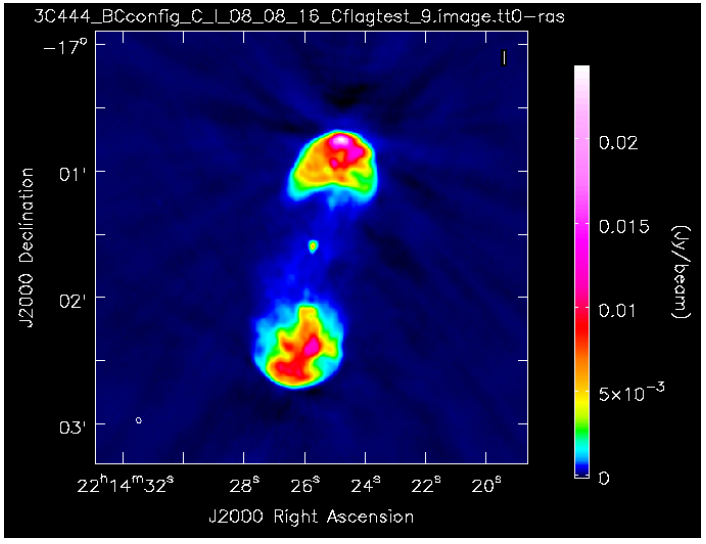

(c) B+C configuration

FIGURE 2.5: 3C444 C-band maps

2.4 Intermediate-frequency maps

The JVLA data have provided high fidelity broad-bandwidth images at L and C-band as shown in Section 2.3. The idea is to then produce a spectrum of the lobes which will be used to constrain the high frequency spectral curvature—allowing the age to be calculated by fitting the spectrum with a spectral ageing model (details of this are given in the proceeding section). Therefore, the source fluxes S_{ν_i} at each intermediate frequency i must be determined. This was achieved by imagining the sources at each intermediate frequency, and determining the source flux from each map to produce a spectrum. The software package BRATS (Broad-band Radio Astronomy Tools) (Harwood et al., 2013) was the tool of choice to extract the source spectrum from the intermediate frequency maps. Further information on the procedures taken in BRATS is given in Section 2.5.

For simplicity in choosing which intermediate frequencies to image, I imaged the data at each spectral window. For example, the L-band data contained 16 spectral windows corresponding to the intermediate frequencies within 1-2 GHz. An image was therefore produced using the task `CLEAN` in CASA (see Section 2.2) for each spectral window. For the imaging, both L and C-band images at each spectral window were imaged at the same dimensions and resolution. The beam size that I forced all the spectral window images to be convolved with were circular, and its size chosen based on a trade-off between the resolution used for the broad-band L and C-band images in Figures 2.2-2.5. Generally at lower frequencies a lower resolution is used since the structure is larger-scale, whereas at higher frequencies a higher resolution is needed for imaging. Since the resolution must be matched for all spectral window maps across both L and C-band, various beam sizes were tested to find the optimum resolution to image the entire frequency range at L and C-band. The intermediate frequency maps created using CASA and loaded onto the image viewing tool *ds9* are shown below in Figures 2.6 and 2.7. Inspecting the radio images, we can clearly see the ageing of the lobes, where the flux decreases with increasing frequency (while at the point of the hotspots it remains almost unchanged).

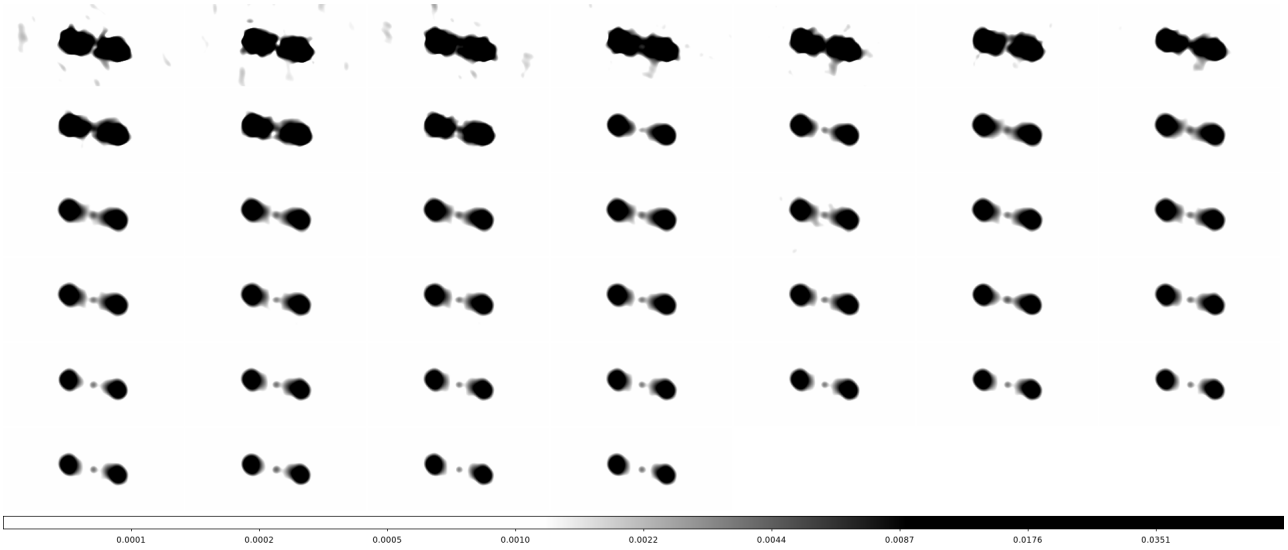

FIGURE 2.6: 3C320 narrow band maps at L-band and C-band—increasing frequency from left to right. Flux scaled to show radio emission as clearly as possible using ds9. Note that some maps were not included due to poor image quality, as can be seen with the low frequency L-band maps.

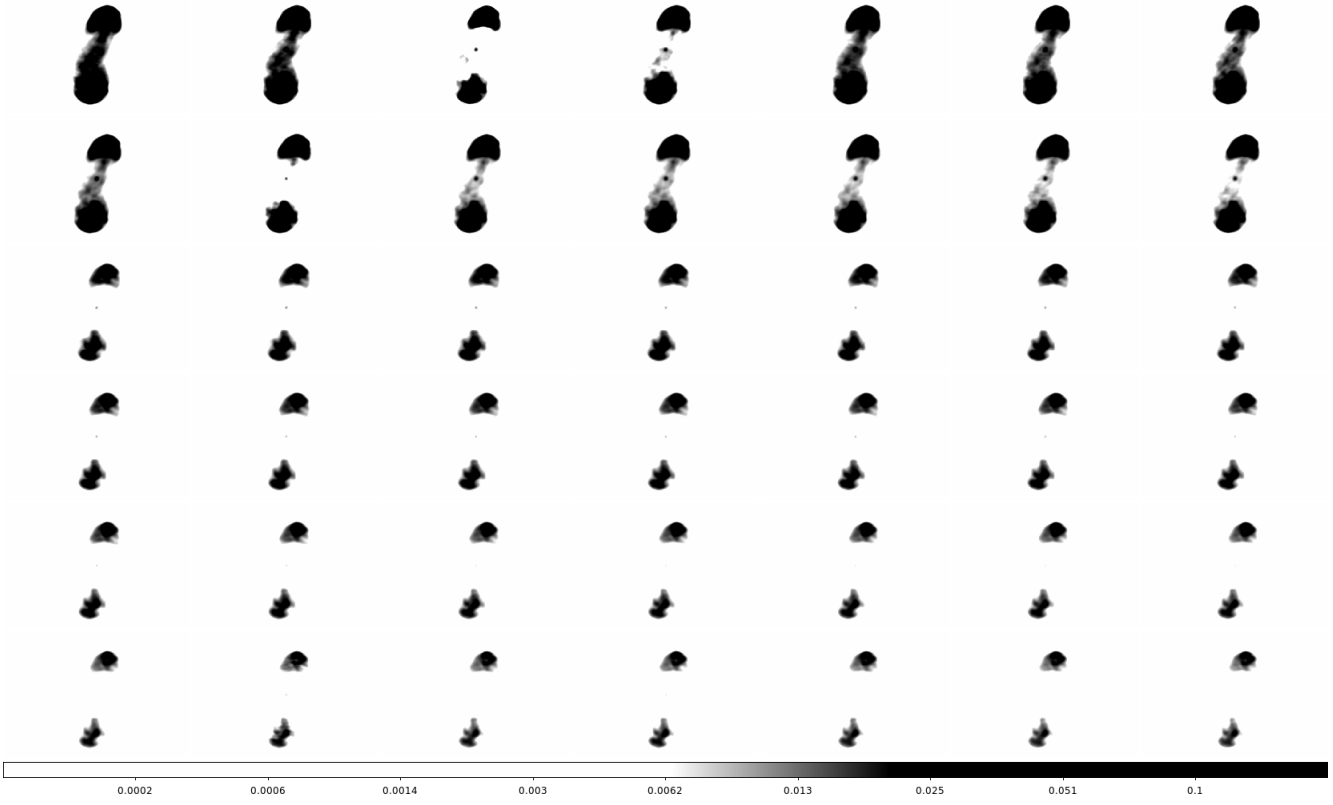

FIGURE 2.7: 3444 narrow band maps at L-band and C-band—increasing frequency from left to right, shown in ds9.

2.5 Spectral Ageing analysis

2.5.1 BRATS introduction

BRATS was developed specifically for the analysis of spectral energy distributions over broad-bandwidths (Harwood et al., 2013). The usage of BRATS for radio spectral analysis from the next-generation radio interferometers such as the JVLA itself, as done in Harwood et al. (2013, 2015), is therefore set to become common practice.

BRATS is written in the C programming language and uses subroutine libraries such as `PGPLOT` for graph-visualisation. The main features of BRATS that I have made use of for this project include fitting of spectral ageing models to the data, determination of the goodness-of-fit and determination of model parameters such as the injection index. A description of these fitting processes is given in the following sections.

2.5.2 Loading data

`BRATS` requires a background region file and a source region file as input files while loading the data, which it uses to calculate rms noise values. This is used to determine the level of flux detection to use for the spectral analysis for the source. For example, a 3σ detection level will use the total flux of the source at each frequency down to three times the noise level. The background and source regions were defined also using ds9. In choosing which map to use to define these regions there is a trade-off between selecting all extended structure and including noise artefacts mistaken for flux from the source. I therefore used the L-band maps of both sources at the highest frequency (spw 15) in order to include all possible extended structure as provided by low frequency observations, as well as identifying the actual source regions correctly. The background regions were taken as a large square area away from the sources, so as to determine the most reliable noise level for the images. These two region files, for both sources, were saved into the same directory as the multiple frequency maps. The source detection maps for 3C320 and 3C444 were chosen at 3σ as a standard detection level, and flux density maps were output as standard by BRATS once the data is loaded. These are shown in Figure 2.8.

2.5.3 Setting regions

The next step was to set the regions of the source to which the ageing models are to be fitted. The main advantage of using BRATS over other, older spectral ageing tools becomes apparent here. BRATS is able to fit models onto the data on a pixel by pixel basis, rather than onto large regions as had been done

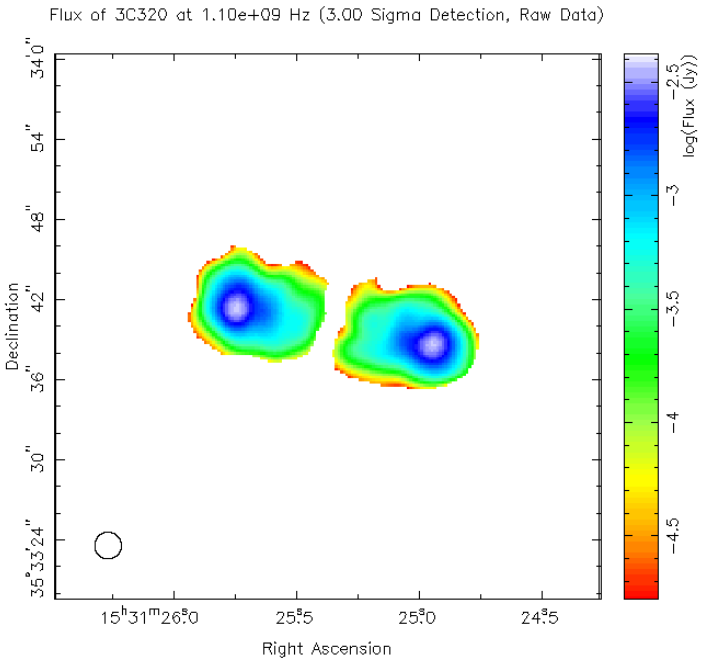

(A) 3C320 source flux

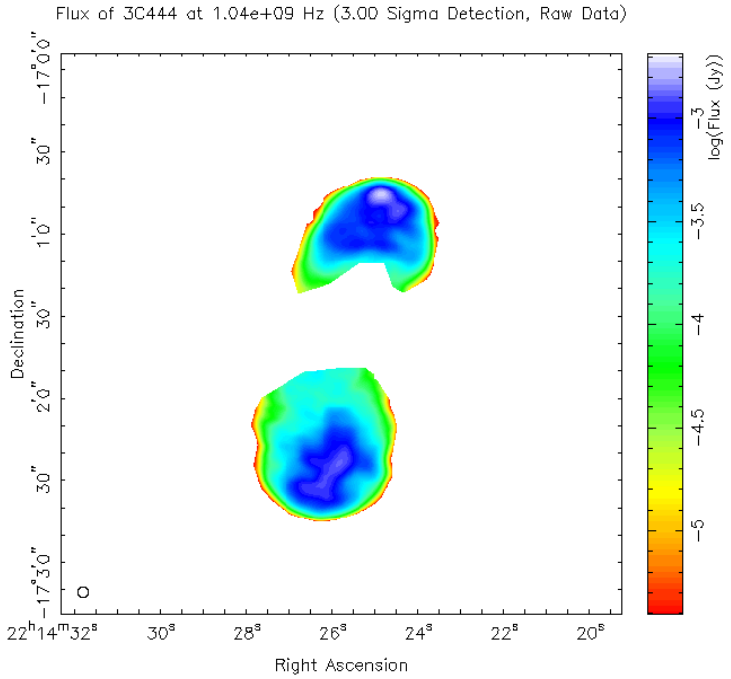

(B) 3C444 source flux

FIGURE 2.8: Source flux detection maps at 3σ at 1GHz, output by BRATS. Only the lobe regions were taken for source detection.

in the past (Alexander and Leahy, 1987). The idea is to have regions that have a good signal to noise ratio—which historically led to large spatial regions for fitting. With the advance of the new generation radio telescopes such as the JVLA, image fidelity and *dynamic range* has improved greatly, and therefore smaller regions can now be used which have the required signal to noise ratio—to allow ageing models to be fitted for each pixel.

As well as improving the resolution of the fitting process onto each spatial region, the reliability is also improved in determining the true spectrum from each region—as uncertainties can arise when a region contains a superposition of spectra since we are integrating the flux along the line-of-sight through the source (see Harwood et al. (2013) for further details). The commands `searcharea` and `signaltonoise` were set such that the regions for fitting are all 1 pixel in size. Note that for older and poorer quality data, larger spatial regions may still have to be used rather than single pixels. The flux errors for each region are set by default to to the 2% flux calibration error for JVLA data at these frequencies. These errors in flux density are due to contributions from thermal noise due to the sensitivity of the JVLA array or problems with calibration and deconvolution processes (e.g., (Perley et al., 1989; Leahy et al., 1989)). The regions for fitting were then set using the command `setregions`. This pixel detection technique determines whether each pixel in the source is set to a region, based on the criteria that (Harwood et al., 2013)

$$S_{reg} \geqslant R_{SN} \left\{ (J \times S_{RMS}) \sqrt{n_{reg}/a_{beam}} \right\} \tag{2.5}$$

where S_{reg} is the flux density of the source, R_{SN} is the user defined signal to noise ratio, J is the thermal noise multiplier, S_{RMS} is the thermal RMS noise, n_{reg} is the number of pixels already in a region and a_{beam} is the primary beam area. A thorough definition explanation for these terms and input parameters are given by Harwood et al. (2013), however for the current work the default parameters were used.

The region maps were then outputted, shown in Figure 2.9. Note the difference between the region map for 3C320 and the actual 3σ flux map in Figure 2.8. In the region map some flux is missing at the tip of the western lobe and the overall region is smaller. This discrepancy may be due to pixel alignment issues. Between all the images created from the data at 1-2 and 4-8 GHz, there may be small variations in the alignment of the maps at different frequencies—where the positions of some structures such as the AGN core may change slightly as a function of frequency (known as *core-shift* (Lobanov, 1998)). Generally the method used to solve this alignment issue is to use compact *optically thin* objects that are observed in all the maps as reference points to calibrate any changes in position for the source structure. These can be background quasars, for example, that are seen as point sources in the images, and are assumed not to change their positions as a function of frequency. The L-band maps of 3C320 however, have no such point source and therefore it was not possible to implement pixel-alignment between the L and C-band maps. As explained previously I submitted a proposal for e-MERLIN observations of 3C320 at a higher resolution than the current JVLA L-band map which, if the proposal is successful, should give

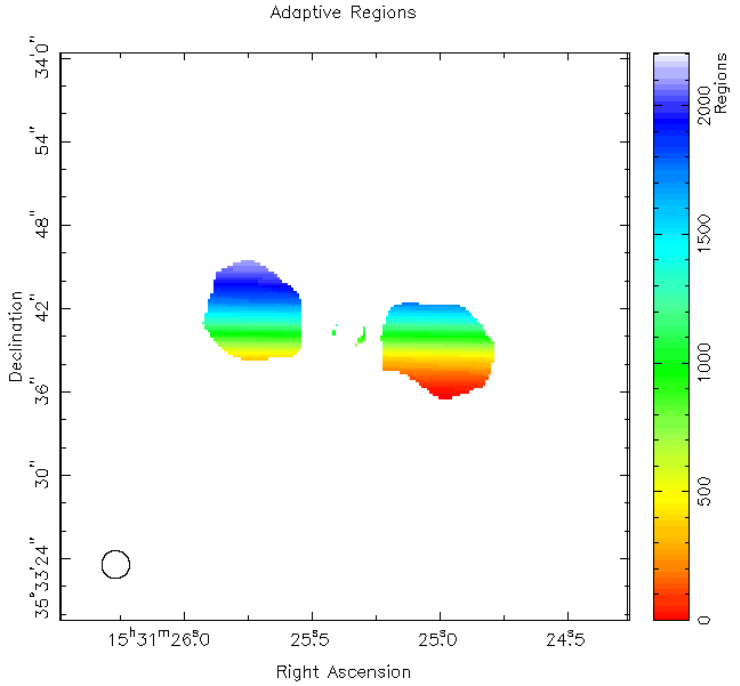

(A) 3C320 region map

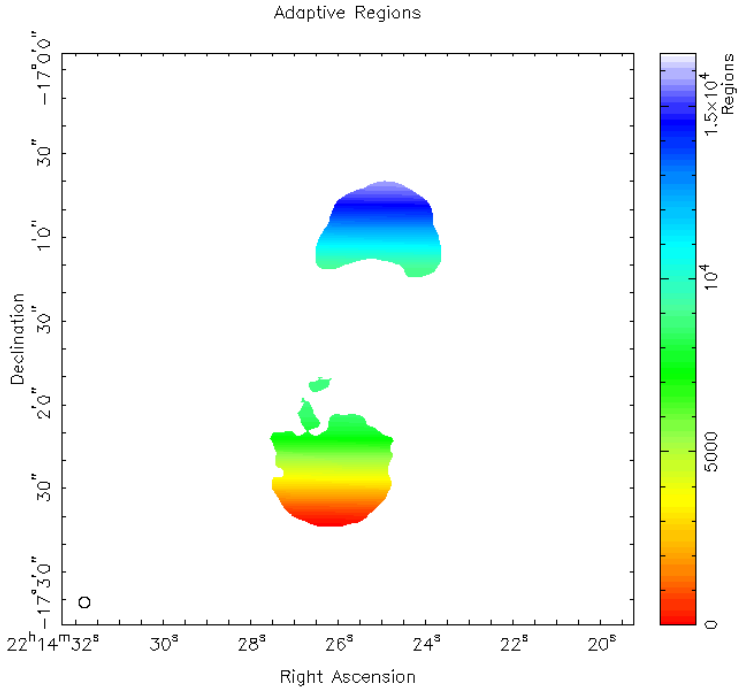

(B) 3C444 region map

FIGURE 2.9: Source region maps selected on a pixel by pixel basis using *adaptive regions*. Note the contrast between the region maps and the source detection maps in Figure 2.8. These regions are then selected for the fitting process.

the opportunity to see point sources at L-band which are otherwise seen in the current C-band images of 3C320.

2.5.4 Injection index fitting

The injection index α_{inj} describes the slope of the spectra at low frequencies of the initial distribution of the electron population at the hotspots, as explain in Section 1.7. However, since the hotspots have a very small spatial region relative to the lobe, these regions can be affected by convolution effects—the beam, which is convolved with the `CLEAN` components to produce the image, can be many times larger than the physical size of the hotspot and therefore the flux from these regions may not give a reliable spectral index. The spectral age fitting requires a fixed value for the injection index and therefore `BRATS` includes the `findinject` command which fits the ageing models to the low frequency power-law spectrum of the data, and minimises the χ^2 values after fitting to each pixel, to find the best fitting injection index. This is done by determining the spectral index from the data so that the data flux for any frequency can be obtained. The model fluxes are then determined using the standard synchrotron equations (see Section 1.3), and then compared to the observed fluxes using the χ^2 statistic

$$\chi^2 = \sum_{\nu=1}^{N} \left(\frac{S_{i,\nu} - S_{model,\nu}}{\Delta S_{i,\nu}} \right)^2, \tag{2.6}$$

where $S_{i,\nu}$ is the observed flux density at region i. Thus this process is repeated for all regions, and the minimum χ^2 giving the best fitting injection index is determined.

`Findinject` also requires a value for the magnetic field in the lobes as an input parameter, since the strength of the magnetic field governs the synchrotron loss rate (see Section 1.3). The magnetic fields in the lobes of 3C320 were estimated using existing *Chandra* data—as described in Section 2.7.5. From this analysis, an *equipartition* field strength of 4.44×10^{-9} T was calculated and an upper limit inverse-Compton measurement corresponding to a field strength of 0.5×10^{-9} was made. This constraint therefore gives a range of possible magnetic field strengths in the lobes. Therefore, the injection index fitting was performed for 3C320 using 3 magnetic field strengths—at 4.44×10^{-9} T, 1.00×10^{-9} and 0.50×10^{-9} T. For 3C444, X-ray analysis of the lobes were taken from Croston et al. (2011) where the magnetic field strengths lie in the range 0.5×10^{-9} T to 1.05×10^{-9}. Injection indices for 3C444 were therefore fitted at 0.5×10^{-9} T, 0.74×10^{-9} T and 1.05×10^{-9} T. From shock-acceleration theory (Section 1.3.1), we expect to find injection indices between 0.5 and 1.0, and these were the minimum and maximum values set before fitting, respectively. The best-fit injection indices for these field strengths are tabulated in Section 2.8.1.1.

For 3C320, the fits gave somewhat varying results between models and magnetic fields. For the JP model, values of $\alpha_{inj} \approx 0.65$ were obtained for all three magnetic field strengths, with $\chi^2_{red} \approx 6.26$ for 37 degrees of freedom. This result of a relatively flat injection index agrees with previous observations of radio galaxies (Meisenheimer et al., 1989; Carilli et al., 1991b), but is in contrast to the results of Harwood et al. (2013, 2015) where much steeper injection indices of >0.8 were found for their sources which were also FR-II radio galaxies. The KP model, describing a constant pitch angle for the electrons over its radiative lifetime, gave only slightly better fit results, agreeing with the work of Harwood et al. (2013, 2015). The injection indices here were $\alpha_{inj} \approx 0.6$ with $\chi^2_{red} \approx 5.5$ with the exception of the fit using a field strength of 4.44×10^{-9} T, giving $\alpha_{inj} \approx 0.77$ with $\chi^2 \approx 12$. The Tribble model gave best fitting indices of $0.60 \leqslant \alpha_{inj} \leqslant 0.65$ with the same goodness-of-fit as the JP.

For 3C444, the injection index fits gave consistent results with both the JP and KP fits giving $0.65 \leqslant \alpha_{inj} \leqslant 0.70$. These injection indices were not fitted to a higher precision due to the large amount of CPU time required for processing compared to 3C320, since 3C444 had almost 5 times more regions than 3C320. Furthermore, for the same reason, the Tribble injection index fit was not performed and the JP injection indices were used instead. This is a reasonable assumption to make since the injection index is expected to be ~ 0.65, as is given by both the JP and JP fits, and that the Tribble model is based on the JP losses itself.

2.5.5 Spectral Age fitting

Prior to fitting a spectral ageing model to the data, various parameters such as the injection index and the lobe magnetic field were set to their appropriate values. For example, if fitting the JP model at 4.44×10^{-9} T then the best fit injection index for these parameters was set, as fitted beforehand using *findinject*. The maximum age was set using the command *myears* to 50 Megayears as a default—although this can be increased if the fitted ages reach this limit. I fitted the ageing models, using the three field strengths mentioned above, to both sources using the commands `fitjpmodel`, `fitkpmodel` and `fittribble`. The best-fit ages for all three magnetic fields for all three ageing models for both 3C320 and 3C444 are given in Tables 2.12 and 2.13.

Once completed, a spectral ageing map showing the best fit ages as as function of position can also be plotted. I display the maps for the JP, KP and Tribble models for 3C320 and 3C444 at 1.00 nT and 0.74 nT respectively, along with their χ^2_{red} maps in Figures 2.10-2.13.

FIGURE 2.10: 3C320 spectral ageing maps at 1.00 nT with the JP model (left), the KP model (right) and the Tribble model (bottom). Contours are at 6.81 GHz

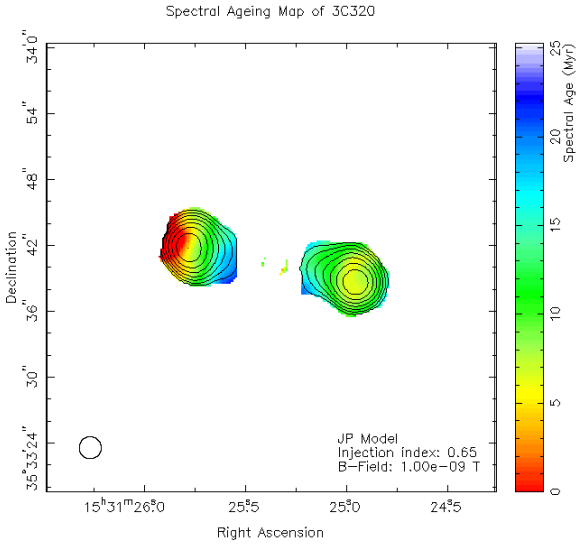

(a) A-configuration

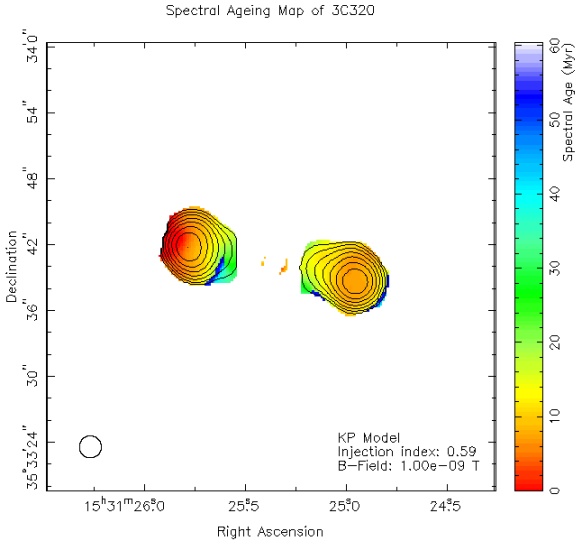

(b) B-configuration

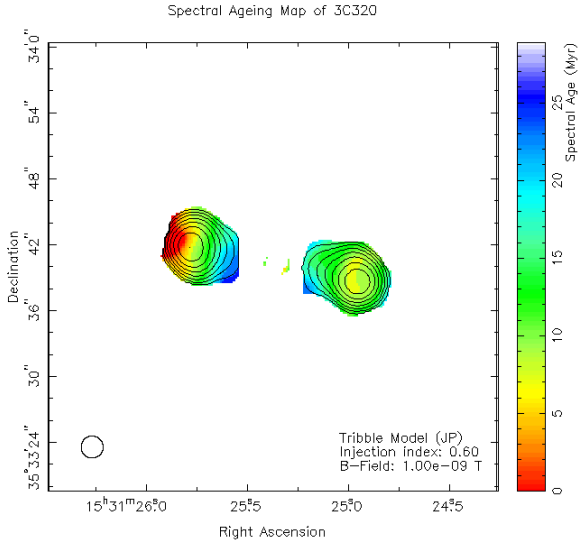

(c) A+B configuration

FIGURE 2.11: 3C320 $\chi^2_{\rm red}$ maps at 1.00 nT with the JP model (left), the KP model (right) and the Tribble model (bottom). Contours are at 6.81 GHz.

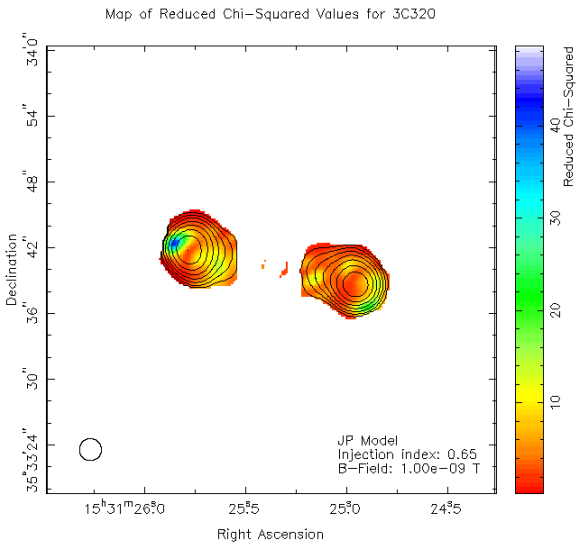

(a) JP

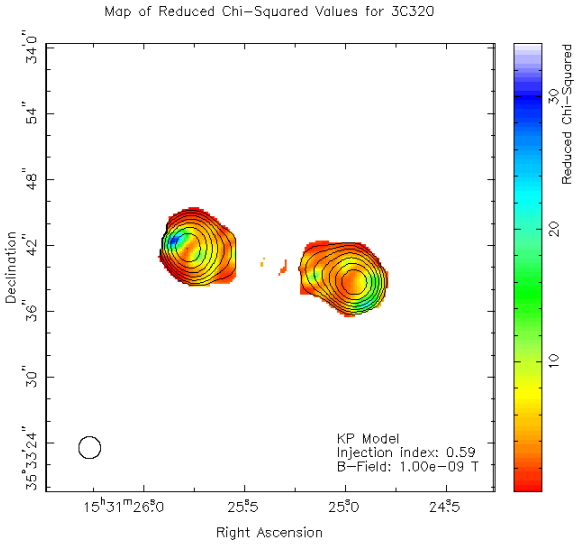

(b) KP

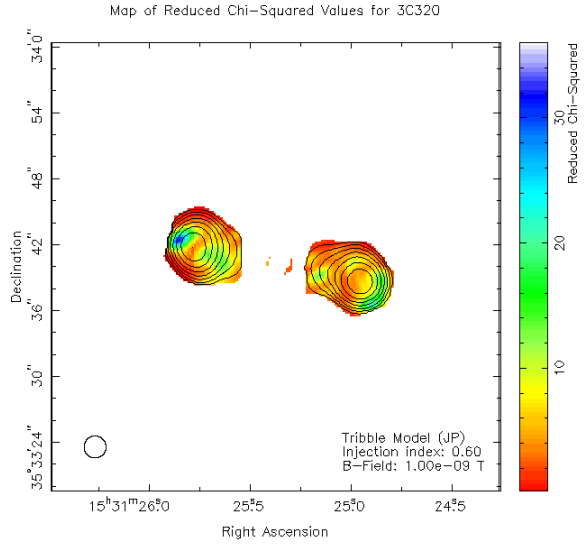

(c) Tribble

FIGURE 2.12: 3C444 spectral ageing maps at 0.74 nT with the JP model (left), the KP model (right) and the Tribble model (bottom). Contours are at 6.04 GHz.

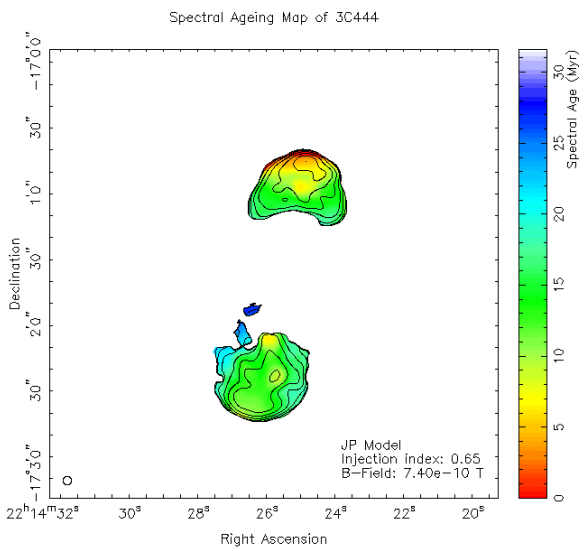

(a) JP

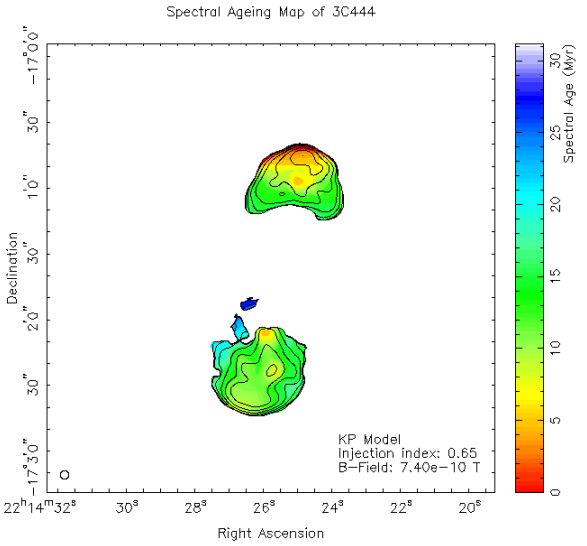

(b) KP

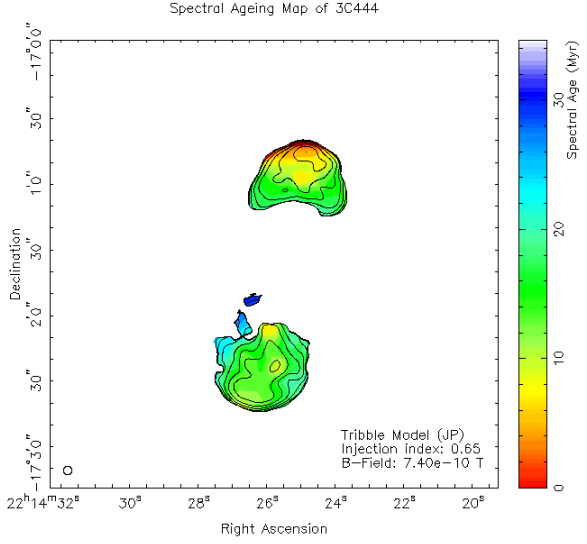

(c) Tribble

FIGURE 2.13: 3C444 $\chi^2_{\rm red}$ maps at 0.74 nT with the JP model (left), the KP model (right) and the Tribble model (bottom). Contours are at 6.04 GHz.

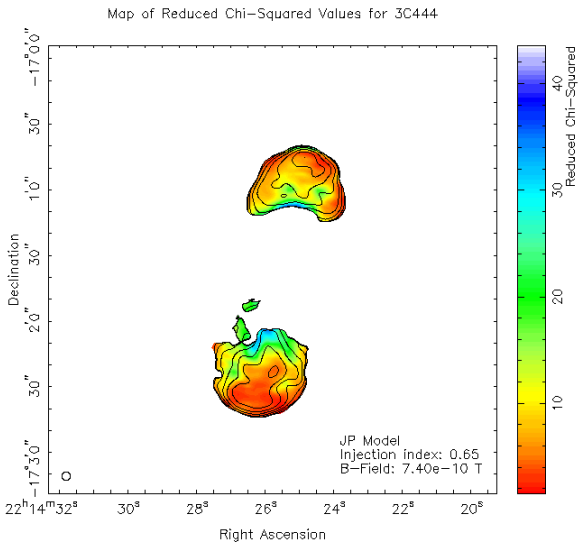

(a) JP

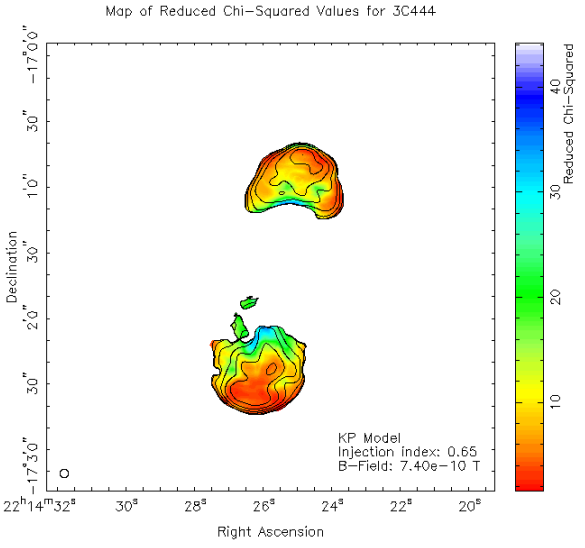

(b) KP

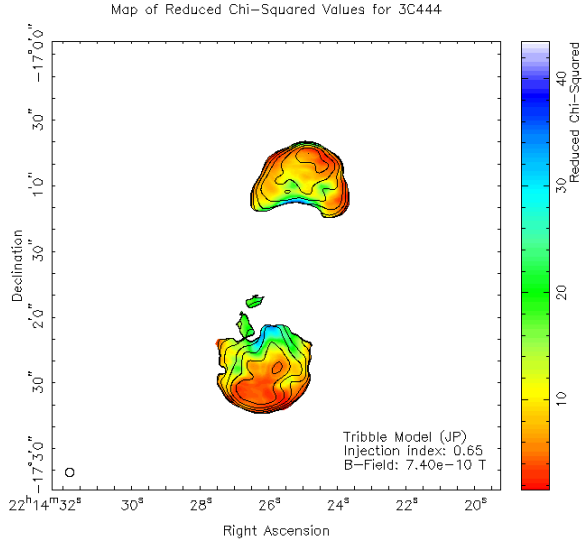

(c) Tribble

2.6 *Chandra* X-ray Observations

Since powerful radio galaxies are rare at low redshift, initial radio surveys followed by deep X-ray observations is the most efficient way of identifying strong shocks in a cluster, as has been done with 3C320 and 3C444 (Croston et al., 2011). For the purposes of this project, X-ray data for the cluster emission around 3C320 and 3C444 are important for two main reasons: calculating the dynamical age for comparisons with spectral age and for constraints on the lobe magnetic field—as is required in order to determine a spectral age, as explained in Section 1.7. In this section, I present the analysis of the *Chandra* observations obtained of the cluster environments of 3C320—in order to constrain its dynamics. For 3C444 the existing X-ray analysis is used, as published by Croston et al. (2011).

2.6.1 Technical observation details

The calculation of the dynamical age requires an accurate determination of the properties of the driven shock in the thermal X-ray emitting gas of the cluster. In particular, as explained in Section 1.4.3, a test for the shock model requires the measurement of the density, pressure and temperatures of the shocked and un-shocked environment of the cluster. Deep and sensitive X-ray observations are therefore needed to observe such a surface brightness jump, and drive the observing requirements detailed below.

The observational set-up from previous snapshot observations for 3C320 were retained—the X-ray image of which is shown in Figure 2.14. The source was observed on the ACIS-S3 chip of *Chandra*, using the 'VFAINT' mode. *XSPEC* simulations were used to estimate required exposure times, and it was found that 3C320 required around 110 ks, roughly 10 times the exposure from the previous snapshot data in Figure 2.14.

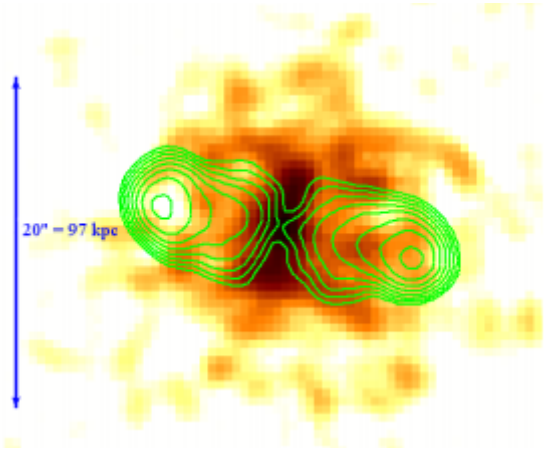

FIGURE 2.14: Previous best X-ray snapshot image of the X-ray emission around 3C320

2.6.2 Data reduction

In contrast to *JVLA* data reduction, *Chandra* observations are initially reduced using a pipeline before the data is available to the end user. This pipeline consists of three stages, or Levels.

Level 0 is the initial stage where raw data from the *Chandra* spacecraft is sent to the observatory and converted into Flexible Image Transport System (FITS) files. Then, in Level 1, instrumental corrections such as aspect solutions are applied to the data. The aspect solution corrects for an accurate determination of the celestial position of an event. Level 2 event files are then created by filtering the data from Level 1. These filters are based on what are known as 'status bits' and 'Good Time Intervals' (GTI). The status bits are contained in the 'status column' containing 32 bits in an event file. These bits indicate potential bad pixels or cosmic rays for example, and are labelled as either good or bad. GTIs represent time filters used to constrain the data, based on the active times of the CCD's during the observation, the quality of the aspect solutions etc.

2.7 X-ray data analysis

2.7.1 Spectral Extraction and Fitting

The first step after data reduction was to extract the spectrum from the calibrated data. This was done using a python code, which extracts the spectral information from the event files for the region of interest. This requires the region files, and therefore regions where the cluster emission lies were defined using ds9, as well as a background region away from the source to subtract background flux in the spectra. Cluster regions were taken to analyse the spectra of the shocked and unshocked regions, and the regions where the lobes of 3C320 are located were also taken for the potential detection of an X-ray inverse-Compton component in order to calculate a magnetic field strength in the lobes (see Section 2.7.5). The extent of the cluster emission from the observation is shown in Figure 2.15, while the regions taken for analysis and model fitting are shown in Section 2.7.7. Using the *Chandra Interactive Analysis of Observations* (CIAO) software package for data analysis of X-ray observations, the appropriate files can be loaded after extracting the spectrum from the data, and plotted. Spectra for two regions enclosing the entire cluster emission taken from the X-ray image are shown in Figures 2.21 and 2.22. The *Sherpa* application was then loaded which allows the user to fit models to spectra—such as a thermal plasma model to the cluster region.

Bad data were removed using the `ignore_bad()` command which ignores bins based on bad data flags such as status bits. Spectra from 0.5—5.0 keV were allowed only for all regions—spectra at higher energies had anomalous data points and gave bad fits. Background emission was subtracted by defining

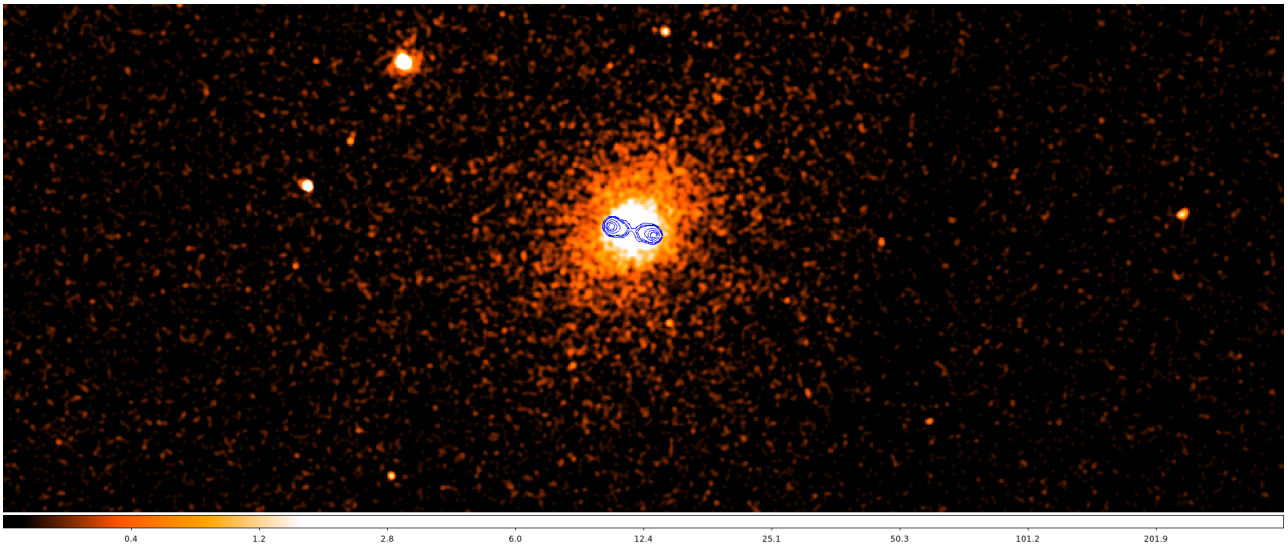

FIGURE 2.15: *Chandra* 110 ks observation of the X-ray cluster emission with 4 GHz radio contours of 3C320 overlaid, provided by the JVLA observations.

a background region and subtracting this from the data. These background regions were made both off-source (a circular region away from the cluster) and on-source (an annulus around source region) for both the shocked and unshocked regions using ds9, as can be seen in Section 2.7.7. It was found during the stage of region testing that the on-source thermal background gave relatively better fit results and is more physically plausible. This is because it accounts for foreground cluster or other thermal emission through the line of sight that may contaminate the spectra. For example, for the shocked region as shown in Figure 2.18, the region also contains the foreground unshocked cluster material and thus needs to be subtracted. For the shocked and unshocked regions therefore, the background region is an annulus around the specified on-source region (see Figures 2.18-2.22). For the shocked region three backgrounds were made to test—off-source, tight on-source around region, and a looser on-source background that is the same as that used for the unshocked region.

2.7.1.1 Defining shocked regions

The region that I denote the 'shocked region' was chosen so as to encompass the extent of the region of very high surface brightness relative to the outer regions of the cluster, shown as the whiter regions in Figure 2.15. As per the shock conditions presented in Section 1.4.3, a shock requires a high-density region and observed X-ray emission scales as the square of the density, thus this strong surface brightness region gives strong evidence for a shock. Other regions for the shocked environment were tested beforehand such as using smaller and larger circular regions and elliptical regions. However, the selected shock region was chosen based on the χ^2 of the fits, errors on the fitted temperature, having a good physical basis in relation to 3C320's radio structure and the shape of the brightest emission structure shown by the X-ray data. A few background regions regions were also tested: an off-source background region, an on-source background close to the region and an on-source background that is the same background

region as used for the circular unshocked region (Figures 2.18-2.20). The latter two background regions have the advantage in that they account for the line of sight X-ray emission immediately in front of the cluster.

2.7.1.2 Defining un-shocked region

Similar reasoning was applied when choosing the best regions to encompass the unshocked environment of the cluster. The background regions were chosen by taking an annulus outside the selected un-shocked region to account for line of sight foreground emission. Two unshocked cluster regions were tested—a circular region outside the circular shocked region and an elliptical region which encompasses the extent of the elliptical surface brightness emission of the cluster, as can be seen clearly in Figures 2.21 and 2.22. This elliptical region has the advantage that it follows the overall shape of the actual surface brightness given by the data. Although naively we would expect standard thermal cluster emission to encompass a spherically symmetric region since the heating is due to gravitational forces toward the centre of the cluster, the true density profile depends on the dark matter potential of the cluster which may not be spherically symmetric, e.g after a cluster merger.

I verified that no sign of bad data (extremely high errors and groups of anomalous data points) remained by plotting the spectrum, before final fitting. A model(s) was then fitted to the data based on the physical emission. A variety of models were used to describe the type of emission being seen in a particular region, and were tested by fitting them with the data. With *sherpa* the user is able to fit more than one model to a single data set as an additive component.

2.7.1.3 X-ray emission models

For each region created, a thermal *APEC* model was fitted. This describes a thermal emission spectrum from collisionally-ionized diffuse gas, using an *APEC* code, and such a spectrum is expected from the X-ray emitting gas of the intra-cluster medium. This *APEC* model was therefore fitted to the defined un-shocked regions. A photo-electric absorption model was also added as a multiplicative component to the *APEC* model to account for the absorption of X-ray photons by foreground atomic matter such as hydrogen atoms in cold gas.

A photon power-law model was also tested for the shocked regions and in the lobes of 3C320. A power-law spectrum is expected for radiation from shocks, as explained in Sections 1.3 and 1.7, however, in the plasma of the cluster we also expected thermal emission either mixed with the power-law photons or due to foreground emission. Therefore, with power-law models the thermal *APEC* model was also added.

2.7.1.4 Fixing model parameters

The absorbing column density was fixed at 1.64×10^{20} atoms/cm^{-2} (based on previous observations) as well as the redshift at 0.342. The elemental abundance for the thermal component was left as a free parameter and fitted to the unshocked region, however the 3σ confidence interval was much too broad for the best fit value and un-physical. Therefore an abundance of $0.3\times$solar was chosen, since the expected value for cluster environments is 0.3-0.5$\times$ solar (Mushotzky et al., 1978; Mushotzky, 1984). Values of 0.5 and 0.7 $\times$solar were also tested, although varying results were obtained between both lobes (statistics improved for the western lobe for increasing abundance, while the opposite was true for eastern lobe). A fixed abundance of $0.3\times$ solar was therefore used, as there is no *a priori* reason to use other values. The only free parameters for the thermal model were the temperature and thermal normalisation. The best fit values for these parameters were then used, by fitting them to both the shocked and un-shocked regions, to test the shock conditions. To check the consistency of the *APEC* model, a thermal *mekal* model was also fitted. This is a similar model to *APEC* in that it models the spectra from hot diffuse gas, but also incorporates line emission from several components. Similar statistics for this model were obtained, giving further confidence to the application of the *APEC* model.

A power-law component theoretically should have better fit statistics near the core of the cluster at the location of the radio galaxy, since we would expect a non-thermal emission contribution due to Inverse-Compton scattering and/or Synchrotron Self-Compton scattering. An absorbed thermal + power-law model was therefore fitted to the shocked region, with a fixed shock temperature from the previous temperature only fit. The data were an acceptable fit with a χ^2 $\sim$0.9 and a similar normalisation to the temperature only fit (see Table 2.3), although the power law normalisation was consistent with zero and therefore an absorbed thermal component only was considered for the shocked region.

Further regions were also created at the location of the lobes (aided by overlaying the JVLA L-band radio contours of 3C320 over the Chandra X-ray data) with an off-source background and fitted with the various models. The power-law fit gave significantly better fit results for the lobes than a power law + thermal model and only a thermal model. The fitted steep photon index of $\gamma \sim 2.0$ for the lobes of 3C320 agrees with that obtained for Suzaku X-ray satellite observations of Centaurus A (Stawarz et al. 2013). The fit statistics for a power-law model also agree with the expectation that there is predominantly non-thermal emission from the lobes. Consequently I also tested the shock region masking out the lobes and fitting a thermal model, which we would expect to yield better results if the lobes do indeed contain predominantly non-thermal material. However, I do not include these results here since masking out the lobe regions removes a significant amount of cluster emission through the line-of-sight, and therefore this region was subsequently discarded from my results. Note that the fit statistics with the mekal model were more or less similar to those with the *APEC model*, and subsequently the mekal model fitting was

dropped.

On a physical basis however, there may be a component of thermal emission in the lobes, as detected for the lobes of Centaurus A by Stawarz et al. (2013). Furthermore, it is difficult to entirely remove thermal foreground cluster emission in front of the lobes using only background subtraction. Therefore a power law plus thermal model is expected to provide the best physical description of the lobe region. Tests were made prior to this fit with the absorbed power-law plus thermal model component, but with a fixed photon index for a range of photon indices to see whether a variation in photon power-law index would give varying results for the other parameters. The other parameters such as temperature and thermal normalisation were also left free. Photon indices of $\gamma = 1.5, 1.75$ and 2.0 were used to fit to the spectrum of the lobes. The corresponding results are shown in Table 2.6. Then, the fits were made using a single fixed photon index of 1.75, corresponding to a synchrotron injection index of 0.75. This was a reasonable assumption to make since, as seen in Table 2.6, a change in the photon indices did not produce a significant difference in the fit statistics or the values of the fitted parameter. Furthermore, the lobe temperatures were fixed at the shocked temperature of $kT = 3.560$ from Table 2.3. These fit results are shown in Table 2.7, and were used to detect an inverse-Component component in the lobes—explained in Section 2.7.5.

TABLE 2.3: Statistics, fitted parameters and calculated parameters for tight shock regions.

Region	χ^2_{red}	kT (keV)	Norm ($\times 10^{-4}$)	n_e ($\times 10^2$ cm^{-3})	Vol ($\times 10^{70}$ cm^3)	Pressure ($\times 10^{-11}$ Pa)
Off-source background	1.006	$3.569^{+0.502}_{-0.409}$	$2.683^{+0.154}_{-0.150}$	1.84 ± 0.0521	2.033	2.364 ± 0.312
Tight on-source background	0.841	$3.488^{+0.700}_{-0.542}$	$2.138^{+0.176}_{-0.164}$	1.64 ± 0.0652	2.033	2.059 ± 0.375
Loose on-source background	0.885	$3.560^{+0.553}_{-0.450}$	$2.482^{+0.160}_{-0.153}$	1.77 ± 0.0560	2.033	2.268 ± 0.327

TABLE 2.4: Statistics, fitted parameters and calculated parameters for unshocked regions with tight shocked region masked and modelled as a cylinder. Note all background regions are taken as an annulus just outside selected region.

Region	χ^2_{red}	kT (keV)	Norm ($\times 10^{-4}$)	n_e ($\times 10^2$ cm^{-3})	Vol ($\times 10^{70}$ cm^3)	Pressure ($\times 10^{-11}$ Pa)
Circular	0.927	$3.740^{+3.589}_{-1.460}$	$0.573^{+0.131}_{-0.124}$	0.482 ± 0.0538	6.353	0.649 ± 0.427
Elliptical	1.031	$2.773^{+2.260}_{-0.852}$	$0.633^{+0.134}_{-0.136}$	0.428 ± 0.0456	8.890 ± 0.00295	0.427 ± 0.244

TABLE 2.5: Statistics, fitted parameters and calculated parameters for lobe region fitted with an absorbed thermal *APEC* model. Note a circular on-source background region was taken in the vicinity of the cluster emission (Figure 2.23).

Region	χ^2_{red}	kT (keV)	Thermal norm ($\times 10^{-5}$)
Both lobes	0.613	$3.384^{+0.923}_{-0.610}$	$10.181^{+1.012}_{-0.999}$
Western	0.657	$3.600^{+1.779}_{1.016}$	$5.805^{+0.800}_{-0.731}$
Eastern	0.843	$2.943^{+1.187}_{-0.756}$	$4.383^{+0.669}_{-0.659}$

TABLE 2.6: Statistics, fitted parameters and calculated parameters for lobe region fitted with a power-law plus thermal APEC model with fixed values of γ. γ is defined in the sense $A(E) \sim E^{-\gamma}$. Note a circular on-source background region was taken (Figure 2.23).

Region	χ^2_{red}	γ	PL norm ($\times 10^{-5}$)	kT (keV)	Therm norm ($\times 10^{-4}$)
Both lobes	0.600	1.50	$0.349^{+0.646}$	$3.117^{+0.528}_{-0.762}$	$0.851^{+0.149}_{-0.179}$
Both lobes	0.601	1.75	$0.488^{+1.018}$	$3.223^{+0.437}_{-0.652}$	$0.815^{+0.188}_{-0.286}$
Both lobes	0.604	2.00	$0.245^{+1.207}$	$3.393^{+0.292}_{-0.260}$	$0.885^{+0.123}_{-0.314}$
Eastern	0.915	1.50	$0.000204^{+0.291}$	$2.915^{+0.315}_{-0.795}$	$0.449^{+0.0593}_{-0.0838}$
Eastern	0.915	1.75	$0.00^{+0.445}$	$2.912^{+0.332}_{-0.715}$	$0.448^{+0.0590}_{-0.123}$
Eastern	0.915	2.00	$0.00^{+0.557}$	$2.911^{+0.361}_{0.451}$	$0.448^{+0.0585}_{-0.157}$
Western	0.511	1.50	$0.644^{+0.297}$	$2.769^{+1.442}_{0.652}$	$0.289^{+0.170}_{-0.107}$
Western	0.505	1.75	$0.976^{+0.559}_{-0.931}$	$3.317^{+0.931}_{-1.01}$	$0.178^{+0.255}_{-0.134}$
Western	0.512	2.00	$0.929^{+0.553}$	$4.393^{+0.880}_{-0.771}$	$0.178^{+0.282}_{-0.0900}$

TABLE 2.7: Statistics and fitted parameters for the east and west lobe regions fitted with an absorbed power-law plus thermal APEC model with fixed values of $\gamma = 1.75$, thermal abundance at $0.3\times$ solar and the temperature at the shocked temperature of 3.560 keV from Table 2.3. γ is defined in the sense $A(E) \sim E^{-\gamma}$. Note that the power-law normalisation was set such that it returns the 1 keV flux density in units of μJy.

Region	χ^2_{red}	PL norm (μ Jy)	Therm norm ($\times 10^{-4}$)
Eastern	0.973	$0.000^{+0.0022681}$	$0.420^{+0.050}_{-0.176}$
Western	0.653	$0.000771^{+0.00522}$	$0.531^{+0.113}_{-0.531}$

2.7.2 Calculations of physical parameters

In this section I give a description of the calculations used to determine the electron number density, the distance to 3C320, the lobe volume, and the pressure as stated for the tables in the previous section.

2.7.2.1 Number density of electrons

The normalisation (the number of photons observed at 1 keV) is also a free parameter of the APEC model fit and is given, by the XSPEC guide, by

$$norm = \frac{10^{-14}}{4\pi(D_A(1+z))^2}\int n_e n_H dV. \tag{2.7}$$

Rearranging for the electron density n_e gives

$$n_e = \sqrt{\frac{10^{14}\cdot 4\pi(D_A(1+z))^2\cdot 1.2\cdot norm}{V}}, \tag{2.8}$$

where D_A is the angular diameter distance, V is the volume of the region that has been fitted and we have used the assumption that $n_e \sim 1.2 n_H$. We therefore need to calculate the distance and region volume in order to calculate the electron density.

2.7.2.2 Distance Measurement to 3C320

The quantity $D_A(1+z)$ represents the transverse co-moving distance, which translates to the usual co-moving distance for flat space (k=0), which is given by $d_M(z) = d_H \int \frac{dz'}{\sqrt{\Omega_m(1+z)^3+\Omega_\Lambda}}$ where $d_H = \frac{c}{H_0}$ is the Hubble distance. This is easy to calculate since we know the redshift of 3C320 and for $H_0 =$ 71 kms^{-1}Mpc^{-1}, $\Omega_m = 0.27$ and $\Omega_\Lambda = 0.73$ gives the co-moving distance to 3C320 as $d_{M,3C320}(z) = 4.129\times 10^{27}$cm.

2.7.2.3 Region Volumes

The region dimensions were obtained using ds9. The radius of the regions, both circular and elliptical for the shocked and un-shocked environments, are in units of arc seconds, which was then converted to parsec units since we know the angular size distance (using online cosmology calculator - Wright (2006, PASP, 118, 1711)). At a redshift of 0.342, for 3C320 the linear scale is then given as 4.833 kpc/", and thus the projected linear size in SI units for the radii were calculated.

The shocked region is a circle thus the spherical volume was calculated, as $V_{shocked} = 4/3\pi r^3$, using the region radius on ds9 which was converted from arcseconds to cm using the linear scale mentioned above.

The cold bar region which was masked out (see Figures 2.18-2.20) from the centre of the source, is not believed to contain thermally shocked material from the radio source as it is at the location of the AGN core. The volume of this small region was therefore subtracted from the volume of the sphere. This region is an ellipsoid with the length and width as given by ds9. The depth radius of the ellipsoid was estimated as the same radius of the sphere. This is because I masked this region from the model fitting, and therefore all emission through the line-of-sight is neglected in these calculations—thus the neglected depth is that of the shocked sphere outside of it. The lobe volumes of 3C320 were also subtracted from the total spherical volume, since we do not expect any thermal plasma in the lobes themselves to be shocked. The volume of these lobes were calculated by defining ellipses at the locations of the lobes using ds9, and calculating their volumes. The total subtracted volume calculated for the shocked region was $2.033 \times 10^{70}\text{cm}^3$.

2.7.2.4 Un-shocked

For both regions defined for the un-shocked environment—circular and elliptical, the shocked region within were masked with a circle. In 3-D however, a 90 degrees rotated view would show the un-shocked sphere or ellipsoid with a cylindrical hole through, since by masking the regions with a circle for the shock we have neglected all the X-ray counts within the line of sight. Therefore, this cylindrical hole must be removed in the volume calculations.

For the elliptical un-shocked region with a circular shocked region masked, the most accurate volume calculated required further work. Simply removing the volume of the cylinder to account for this hole may potentially be inaccurate since the top of the cylinder may overlap the surface of the ellipsoid and therefore removing the volume of a cylinder of this size would underestimate the true volume of this region. The true total volume is therefore difficult to calculate analytically, thus the 3-D region was modelled using Python as an ellipsoid with a hole through it. A Monte-Carlo simulation was created by generating a grid of points, which was bound by only including points within the radii of the ellipsoid, while not including points at the location of the cylinder. Then, the fraction of grid points that were in the modelled ellipsoid and the number of grid points of the completely filled ellipsoid was determined. The simulation was run until this fraction converged to a value of 0.6295 ,which was then multiplied as a fractional decrease to the actual observed ellipsoid volume. The systematic errors gained through this method were of the order 0.03%. This error was obtained through analytically calculating true masked volume of the sphere through the use of triple integrals, giving an exact volume, and modelling it through the python code. The error was then obtained by comparing these two volumes, and applying this fractional error to the modelled ellipsoid volume.

2.7.2.5 Pressure

The pressure within a region of X-ray emitting gas can be found by considering kinetic theory for a non-relativistic ideal gas, and is given by

$$P = 3.6 \times 10^{-16} n_e kT \text{ Pa}, \tag{2.9}$$

where n_e is the number density of electrons in m^{-3} and kT is the temperature in keV (Worrall et al. 2012). We have the number density n_e as given by Equation 2.8 and the fitted temperature kT, and therefore we can calculate the pressure trivially. The fit results, fitted temperature, density, volume and pressure of each of the regions used is given in Tables 2.3 and 2.4.

2.7.3 Mach number

Given that the measured densities, temperatures and pressures for the shocked and un-shocked environment of the cluster surrounding 3C320 are reliable, we can use these parameters to test the shock model using Equation 1.18 and obtain a Mach number for the shock.

Since I have characterised both the density and temperature ratios, I can obtain a Mach number best describing both parameters. Although the pressure ratio can be used to determine the Mach number, I did not use this in this analysis since the pressure is a function of the temperature and the density themselves, given by the ideal gas law. Independent measurements of the densities and temperatures would give a more reliable estimate of the shock. I obtained the Mach number by reducing a χ^2 statistic for a range of possible Mach numbers. Providing that I have a set of predicted and actual values for the density and temperature ratios, and assuming that the predicted ratios are Gaussian distributed around the actual ratios, the joint probability density function (pdf) is given by the product of the two gaussian functions for the densities and temperatures. The predicted values for the density and temperature ratios are given by the shock equations (Equation 1.18), which are parametrized by the Mach number. Minimising the logarithm of the joint pdf therefore gives a 'best-fit' Mach number. The logarithm of the joint pdf, which gives the χ^2 statistic, is therefore additive. This is known as the *maximum likelihood minimization* method. The χ^2 statistic becomes

$$\chi^2_{Mach} = \frac{\left(\left(\frac{\rho_1}{\rho_2}\right)_{\text{predicted}} - \left(\frac{\rho_1}{\rho_2}\right)_{\text{actual}}\right)^2}{\sigma^2_\rho} + \frac{\left(\left(\frac{T_1}{T_2}\right)_{\text{predicted}} - \left(\frac{T_1}{T_2}\right)_{\text{actual}}\right)^2}{\sigma^2_T} \tag{2.10}$$

where the subscript 'predicted' denote the values obtained using a range of possible Mach numbers from shock equations as given by Equations 1.18 and the subscript 'actual' denotes the actual ratios as measured from the X-ray data. The errors of the test statistic σ are given by the individual 3σ errors of the

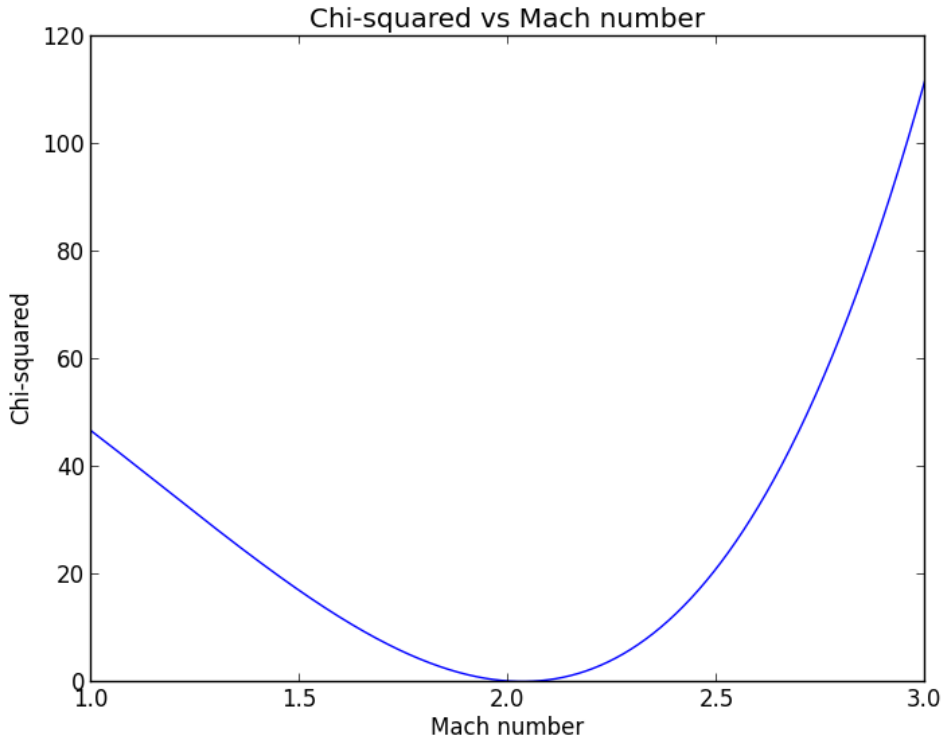

FIGURE 2.16: Plot of the χ^2 test statistic against Mach number, following the maximum likelihood minimization method.

actual measurements.

This χ^2 statistic, which is a function of the Mach number, was then plotted to test the minimization method—shown in Figure 2.16. Note that this analysis is in contrast to that in Croston et al. (2011) where only the temperature measurements were used to obtain a Mach number for the shock surrounding 3C444. The minimum χ^2 squared value of 0.146 gave a Mach number of 2.033. This implies that, since $\mathscr{M} = v/a_{sound}$, the advancing shock in the cluster around 3C320 is travelling at approximately twice the speed of sound in the local medium. The shock is therefore supersonic. The error on the Mach number was derived using 3σ upper and lower limits from the χ^2 plot of Figure 2.16, as was done to find the upper limit of an inverse-Compton detection in Section 2.7.5. This gave upper and lower limits of $2.033^{+0.314}_{-0.372}$.

2.7.4 Dynamical age of 3C320

Given that we have a Mach number that reliably constrains the dynamics of 3C320, we can then obtain the shock advance speed v_{shock} using the definition of the Mach number

$$v_{shock} = a_{sound}\mathscr{M} \tag{2.11}$$

where a_{sound} is the speed of sound in the external medium to the radio source. Using standard fluid dynamics this is given by

$$a_{sound} = \sqrt{\frac{\Gamma kT}{m_p}} \tag{2.12}$$

where Γ is the adiabatic index such that $p \propto \rho^{\Gamma}$, and m_p is the particle mass in the medium. The particles in the medium are non-relativistic and therefore, using simple thermodynamics we have the standard result that $\Gamma = 5/3$. Furthermore we assume that the plasma is ionized hydrogen so that the medium is abundant in protons and electrons so that m_p is the averaged mass of the electron and proton—$m_p = \frac{m_{\rm proton}+m_{\rm electron}}{2} \approx \frac{m_{\rm proton}}{2}$. Furthermore, kT is the temperature of the un-shocked medium as obtained from the *Chandra* X-ray observations, which is 2.773 keV. This gives $a_{sound} = 941$ kms^{-1}. The error in the sound speed is given by the general rule for the measurement error for a function $a = f(b)$ of one variable b

$$\Delta a = \left|\frac{df(b)}{db}\right| \Delta b. \tag{2.13}$$

For the speed of sound this gives

$$\Delta a_{\rm sound} = \left|\frac{1}{2}\frac{a_{\rm sound}}{kT}\right| \Delta kT. \tag{2.14}$$

Therefore, we have $a_{\rm sound} = 941.057^{+383.482}_{-144.569}$ kms^{-1}. Multiplying this with the Mach number, while propagating the errors on the Mach number and the speed of sound, I obtained $v_{shock} = 1.913^{+0.834}_{-0.351} \times 10^6$ ms^{-1}. (These results are tabulated with their errors in Section 2.8).

The length of the source was measured using the highest frequency L-band map of 3C320 on CASA. This gave a length of ≈9.9", and using the distance conversion factor at the redshift of 3C320 to SI units (1"=4833 pc), this gave a length of 1.48×10^{21}m. Thus taking the ratio of the shock speed and the length of the radio source, the dynamical age (with errors from the shock speed) is then

$$t_{dyn,3C320} = 24.452^{+10.661}_{-4.487} \text{ Myrs}. \tag{2.15}$$

This is the first such dynamical age estimate of the radio galaxy 3C320, and is well within the range of ages expected for FR-II radio galaxies, and also within the range of the dynamical ages formed from a sample of FR-II radio galaxies using dynamical models (Machalski et al., 2007).

2.7.5 Inverse-Compton detection

As explained in Section 1.3.2, the combination of observed lobe synchrotron and inverse-Compton emissivities allows the determination of the lobe magnetic field. This is a crucial parameter in determining an accurate spectral age, as inferred by Equation 1.21, and therefore its determination must itself be as accurate as possible. Inverse-Compton detections allow an independent estimate of the lobe magnetic field, in contrast to equipartition estimates which are based on the assumption of equal energy densities

of radiating particles and the magnetic field. These two methods for obtaining the lobe magnetic field allow useful constraints to be obtained on the true magnetic field. For FR-II sources in rich cluster environments, there has been some evidence for a departure from equipartition (Croston et al., 2005b, 2011). It becomes clear that more robust measurements must be made to determine the exact departure from equipartition estimates, and to investigate whether environmental effects play a role in determining lobe magnetic fields as suggested in Croston et al. (2011).

I used the `SYNCH` code by Hardcastle et al. (1998) to determine the equipartition magnetic field for 3C320, while for 3C444 the pre-existing X-ray analysis presented by Croston et al. (2011) was used. As explained previously in Section 2.7, I used the CIAO software to fit an absorbed inverse-Compton power-law plus *APEC* thermal model to the lobes of 3C320 individually. The X-ray inverse-Compton flux density obtained from the fit can therefore be used in conjunction with the radio synchrotron flux densities as provided by the JVLA radio maps, to determine a magnetic field strength—-as explained in Section 1.3.2.

The plasma in the lobes may also contain thermally emitting material, as well as a possible inverse-Compton non-thermal component. Furthermore, the emission from regions chosen are also expected to contain foreground cluster emission and therefore a thermal model must also be fitted, as explained in Section 2.7.1. Therefore, I fixed the lobe temperature to the pre-fitted shocked region temperature of $kT = 3.560$ keV, as outlined in Section 2.7.1. Fixing a parameter reduces the number degrees of freedom, which would improve the fitting process. The results for the photon power-law normalisation, given in units of flux density, are shown in Table 2.7. The results for both lobes are consistent with a non-detection of inverse-Compton emission. Therefore, in the absence of an inverse-Compton detection, the 3σ upper limit of the normalization of the power-law component was taken. An upper limit from the fit was taken to extract the strongest possible detection, since physically this would give the longest range of possible magnetic fields in the lobes—the higher the inverse-Compton flux the lower the lobe magnetic field and traditionally inverse-Compton magnetic fields are lower than equipartition estimates (Croston et al., 2005b). This upper limit was obtained by stepping through the parameter space for the normalisation fit for each value of χ^2, until the 3σ confidence level corresponding to $\chi^2_{\text{upper lim}} = \chi^2_{min} + 9$ for 1 degree of freedom was given. The flux density values for both lobes at this value of χ^2 was then chosen as the upper limit.

For the eastern lobe an upper-limit flux of 2.268 nJy was estimated, and the western lobe gave a limit of 6.000 nJy. These are within the range of inverse-Compton fluxes obtained for the lobes of FR-II galaxies (e.g Erlund et al. (2006);Goodger et al. (2008)). These flux density values, as well as the JVLA L-band and C-band data were added as input data to the `SYNCH` code, individually for each lobe. The equipartition field strength was then estimated, based on its energy being the same as that from the radiating

TABLE 2.8: Equipartition estimates and inverse-Compton lower limits on the magnetic fields for the lobes of 3C320 and 3C444. The field strengths for 3C444 were obtained from Croston et al. (2011).

Lobe	Equipartition estimate (nT)	Inverse-Compton limit (nT)
Eastern	4.413	0.6
Western	4.470	0.35
3C444 (both lobes)	1.05	0.5

electrons. This also gave an inverse-Compton flux prediction based on the equipartition field strength, as seen in Figure 2.17, and was much lower than the actual upper limit measured. The magnetic field was then decreased from the equipartition value, increasing the inverse-Compton prediction until it was consistent with the measured upper limit. The corresponding magnetic field is then the assumed lobe magnetic field based on inverse-Compton constraints. This then gave an upper and lower limit to the true lobe magnetic field, and these limits can be tested with the spectral ageing models. The values for the equipartition magnetic field strengths and inverse-Compton field strengths for each lobe are given in Table 2.8.

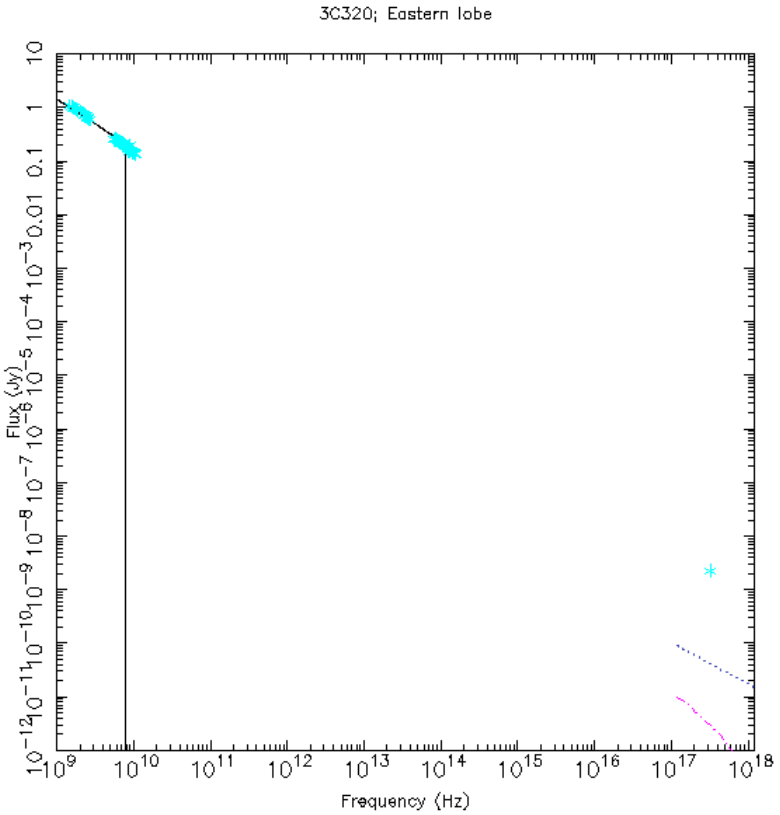

FIGURE 2.17: Spectrum of the eastern lobe of 3C320 containing the JVLA L-band and C-band flux points and the measured upper limit inverse-Compton flux (cyan) using SYNCH. The predicted inverse-Compton (dark blue) and synchrotron self-Compton flux (magenta) are also shown.

As can be seen based on the current measurements for 3C320, the inverse-Compton constraints are at

a large departure from equipartition. Three magnetic field values in between the inverse-Compton and equipartition estimates were input for the spectral age calculations, giving a range of possible ages for the spectral age. A lower limit field, accounting for both lobes, of 0.5 nT, an upper limit based on equipartition of 4.44 nT and an intermediate value of 1.00 nT was used to test the spectral age of 3C320. The magnetic field for which the dynamical and spectral ages agree would then give evidence for the true lobe magnetic field, and hence the magnitude of the departure from equipartition estimates, if any. This spectral age test was also done for 3C444, using the range of field strengths obtained in Croston et al. (2011) using similar analysis. The results for the spectral ages for each of the tested lobe magnetic fields are tabulated in Section 2.8.

2.7.6 Lobe internal pressure

Based on dynamical models for FR-II radio galaxies, the lobes must be *strongly* overpressured with respect to the external medium in order to drive such a supersonic expansion Kaiser and Alexander (1997); Alexander (1987). At minimum therefore, throughout the life time of the source the lobes must be pressure-balanced. The internal pressure inside the lobes of 3C320 can be calculated using

$$p_{int} = \frac{1}{3} u_T \tag{2.16}$$

where u_T is the total energy density in the lobes. This is the sum of the energy densities in the radiating particles and the magnetic field. We assume that there is no contribution in the lobes from non-radiating particles such as protons, as suggested for a sample of FR-II radio galaxies in Croston et al. (2005b); Kataoka and Stawarz (2005), in contrast to the FR-I population (Croston et al., 2008; Belsole et al., 2007). Croston et al. (2011) found however, that the lobes of 3C444, which resides at the centre of a rich cluster environment, are in fact *under-pressured* relative to its environment—suggesting the existence of a significant population of non-radiating particles in the lobes. I therefore tested this pressure condition for 3C320 which, as explained previously, also exists in the similar condition of being at the centre of a rich cluster.

The internal lobe pressure was found based on the calculations of SYNCH. The magnetic field contribution to the total energy density u_T is based on the lobe magnetic field strength—somewhere in between the estimated equipartition upper limit and the lower limit based on inverse-Compton constraints. This then gives a range of possible internal lobe pressures depending on the magnetic field strength in the lobes. These results, as well as the external cluster pressure from Table 2.4, are given below in Table 2.9. We see that for 3C320 the lobes have higher pressures than the external medium, although within the errors for the external pressure, they may be slightly under-pressured. The implications for these pressures, and those for 3C444, are discussed further in Chapter 3.

TABLE 2.9: Lobe and external pressures for 3C320 and 3C444. The values for 3C444 were obtained from Croston et al. (2011).

Lobe	Equipartition(10^{-11} Pa)	Inverse-Compton (10^{-11} Pa)	External pressure (10^{-11} Pa)
3C320 east	0.563	13.732	0.427 ± 0.244
3C320 west	0.578	35.726	0.427 ± 0.244
3C444 north	0.036	0.210	0.840
3C444 south	0.0230	0.130	0.490

2.7.7 Spectral extraction regions

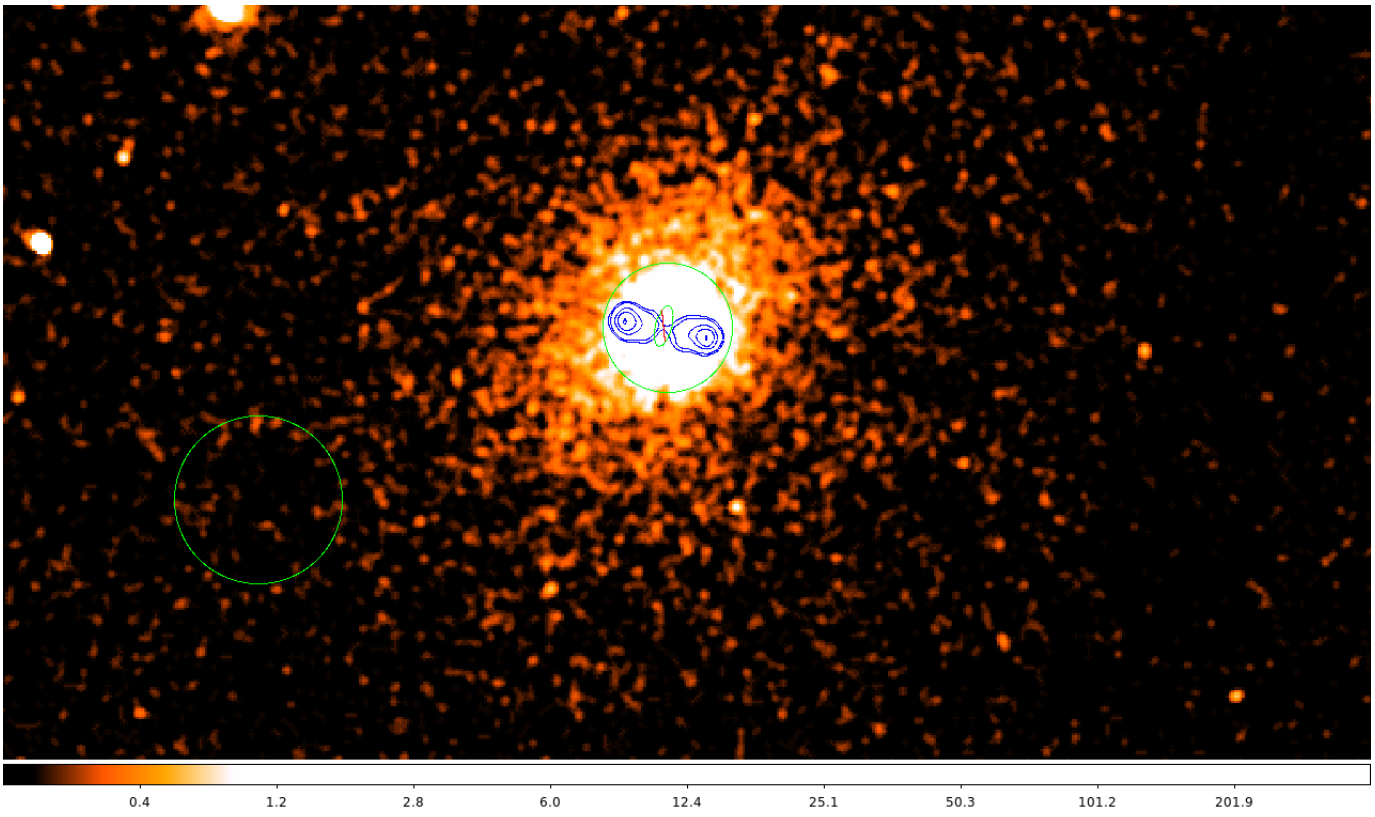

FIGURE 2.18: Region for shocked environment with off-source background

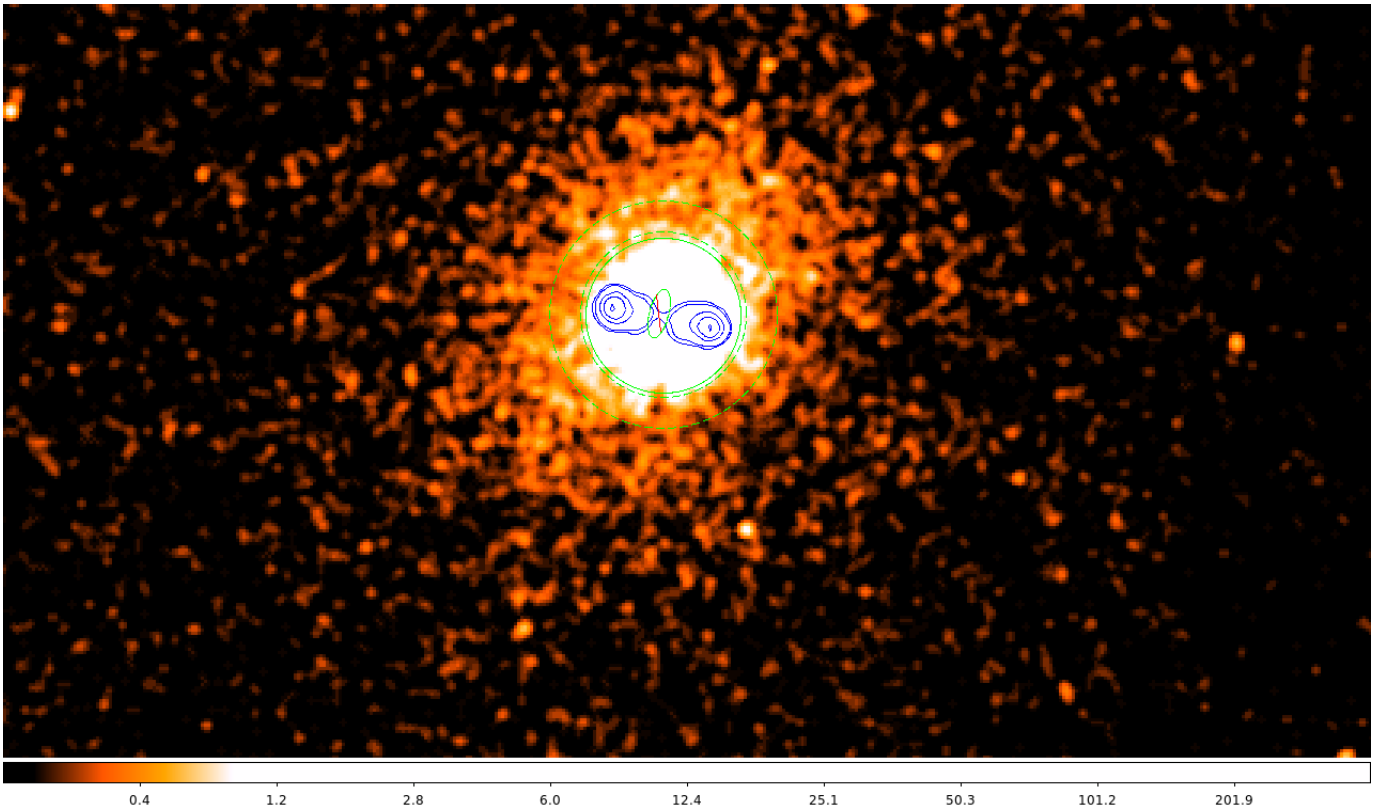

FIGURE 2.19: Region for shocked environment with tight on-source background

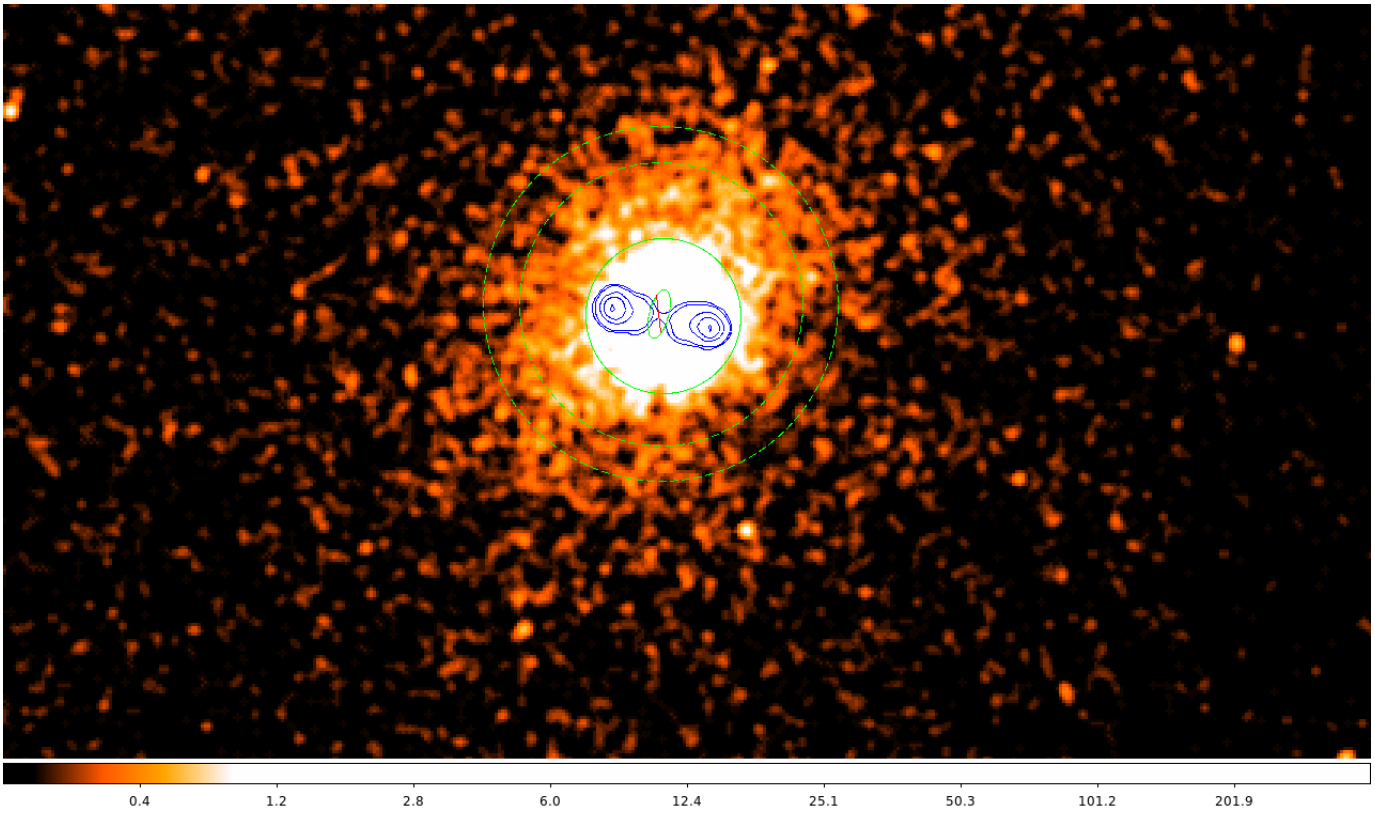

FIGURE 2.20: Region for shocked environment with loose on-source background.

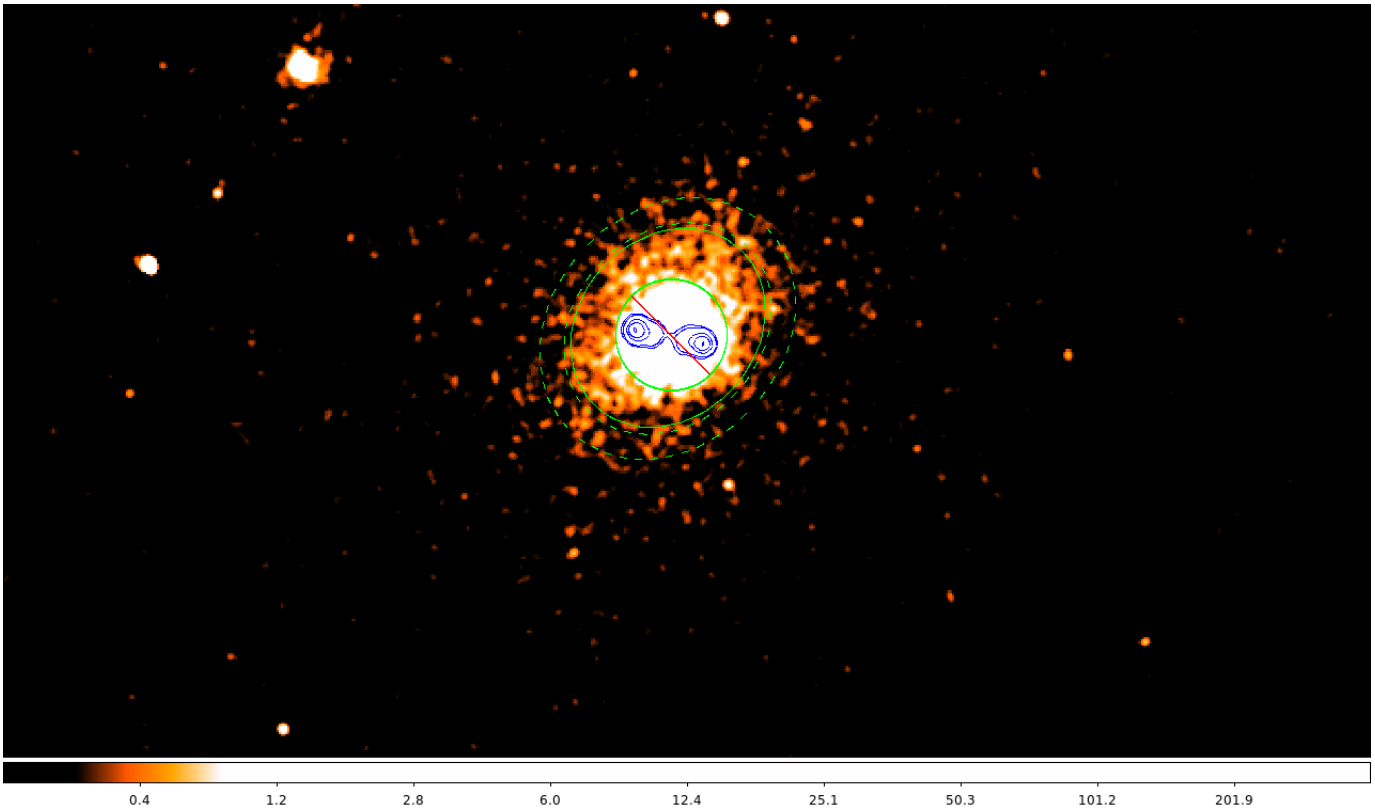

FIGURE 2.21: Region for elliptical unshocked environment.

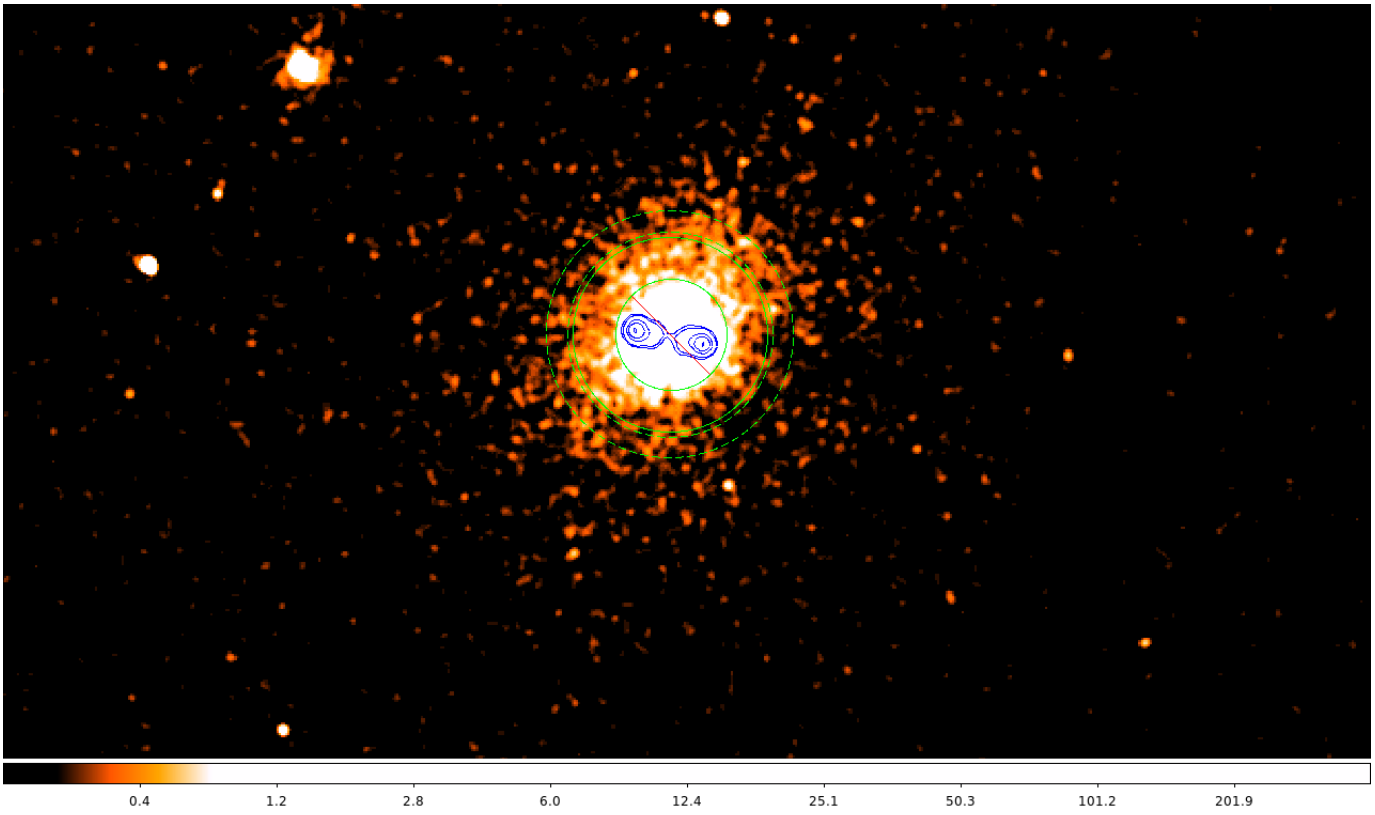

FIGURE 2.22: Region for circular unshocked environment.

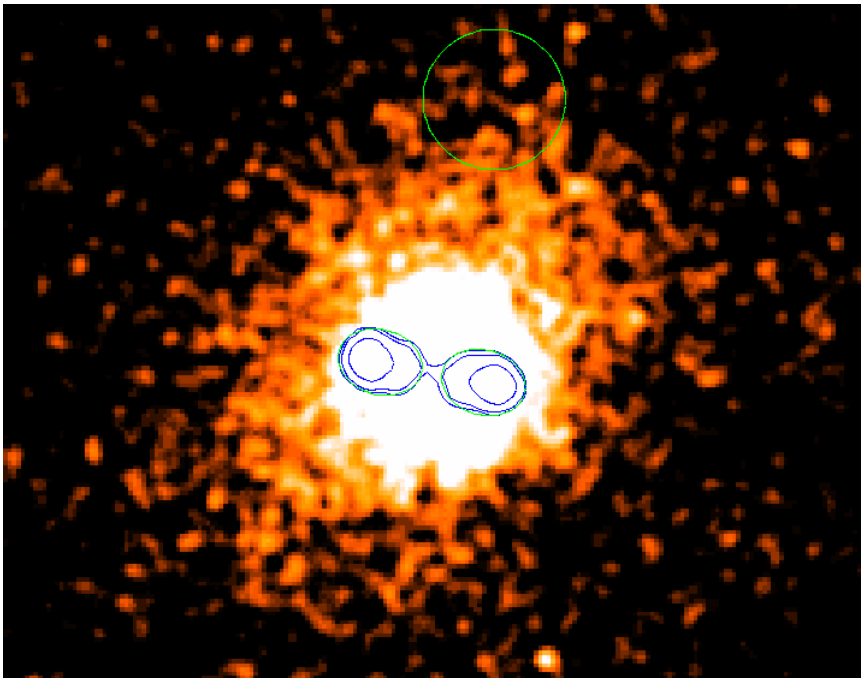

FIGURE 2.23: Region for lobes.

2.8 Results

Here, I present the main results of the project-namely the spectral and dynamical ages of 3C320 and 3C444. A discussion and the interpretation of these results are given in Chapter 3.

2.8.1 Spectral Age

The fitted results using BRATS are presented below. For the fitting, the three spectral ageing models used were the JP, KP and the Tribble model, fitted using three magnetic field strengths constrained by equipartition and inverse-Compton measurements.

2.8.1.1 Injection indices

The injection index is the value of the power-law index for the initial synchrotron spectrum at the hotspots. The JP, KP and Tribble models were fitted, as done in recent spectral ageing studies (Harwood et al., 2013, 2015), between indices of 0.5 and 1.0 which are the theoretical minimum and maximum respectively for a synchrotron power-law. Note that for 3C444, the injection indices for the JP model fits were used, due to the large amount of computing time required. This is a reasonable assumption to make since, the Tribble model is based upon the JP model and that a slight variation in the injection indices do not affect the ages significantly .

TABLE 2.10: Best-fit injection index values for 3C320 using the JP, KP and Tribble models. Values are given at 3 magnetic field strength values ranging from the inverse-Compton to equipartition.

Model	0.50 nT	1.00 nT	4.44 nT
3C320 (JP)	0.65-0.66	0.65	0.65-0.66
3C320 (KP)	0.77-0.78	0.59-0.60	0.60
3C320 (Tribble)	0.60-0.65	0.60-0.65	0.60-0.65

TABLE 2.11: Best-fit injection index values for 3C444 using the JP, KP and Tribble models. Values are given at 3 magnetic field strength values ranging from the lower to upper measured limits. Note that the fits for the Tribble model were not performed and the JP fitted injection indices are given for this model.

Model	0.50 nT	0.74 nT	1.05 nT
3C444 (JP)	$0.65-0.70$	$0.65-0.70$	$0.65-0.70$
3C444 (KP)	$0.65-0.70$	$0.65-0.70$	$0.65-0.70$
3C444 (Tribble)	$0.65-0.70$	$0.65-0.70$	$0.65-0.70$

2.8.1.2 Best-fit maximum spectral ages

TABLE 2.12: Best-fit maximum spectral ages for 3C320 and 3C444, for 3 ageing models. Values are given at 3 magnetic field strength values ranging from the lower to upper measured limits. Ages are given in units of megayears. The ages are given using the lower bound of the fitted injection indices from Table 2.10. Note that the KP model did not produce upper bound errors and gave the same maximum ages—discussed in Section 3.1

Model	0.50 nT	1.00 nT	4.44 nT
3C320 (JP)	$35.48^{+0.74}_{-0.82}$	$21.98^{+0.32}_{-0.63}$	$3.05^{+0.08}_{-0.07}$
3C320 (KP)	$52.53^{+0.00}_{-0.33}$	$52.53^{+0.00}_{-0.81}$	$52.53^{+0.00}_{-4.38}$
3C320 (Tribble)	$42.90^{+0.44}_{-1.99}$	$25.10^{+0.31}_{-0.23}$	$3.78^{+0.03}_{-0.10}$

TABLE 2.13: Best-fit maximum spectral ages for 3C444, for 3 ageing models. Values are given at 3 magnetic field strength values ranging from the lower to upper measured limits. Ages are given in units of megayears. Note that the ages are given using the lower bound of the fitted injection indices from Table 2.11. Also note the same ages fitted for the KP model—this is discussed in Section 3.1.

Model	0.50 nT	0.74 nT	1.05 nT
3C444 (JP)	$38.00^{+0.28}_{-0.20}$	$27.48^{+0.06}_{-0.50}$	$18.48^{+0.06}_{-0.13}$
3C444 (KP)	$38.90^{+0.14}_{-1.45}$	$27.10^{+0.08}_{-0.22}$	$18.90^{+0.04}_{-0.23}$
3C444 (Tribble)	$42.90^{+0.09}_{-1.03}$	$30.10^{+0.10}_{-0.23}$	$20.86^{+0.05}_{-0.09}$

2.8.2 Dynamical Age

TABLE 2.14: Mach number, lobe advance speed and dynamical age of 3C320 and 3C444. The values corresponding to 3C444 are taken from previous work by Croston et al. (2011).

Radio galaxy	Mach number	Lobe advance speed ($\times 10^6$ ms^{-1})	Dynamical age (Myrs)
3C320	$2.033^{+0.314}_{-0.372}$	$1.913^{+0.834}_{-0.351}$	$24.452^{+10.661}_{-4.487}$
3C444	1.7±0.4 [a,b]	1.823±0.447 [b,c]	90.00±22.07 [c]

[a] This was based on analysis of the temperature jump of ~ 1.7 between the shocked and un-shocked medium near the edges of the northern lobe only. Note that a $\mathscr{M} \sim 3$ was calculated based on the density jump, but was not considered for the lobe inflation timescale, in contrast to the work in this project for 3C320 where both temperature and density ratios were used to find the Mach number.
[b] Errors are given at 1σ.
[c] This was calculated by multiplying the Mach number by the speed of sound, which was calculated using the unshocked cluster temperature of 3.6 keV as presented by Croston et al. (2011).

2.8.3 Jet powers

2.8.3.1 3C320

The jet power is calculated as the ratio of the total energy input by the radio galaxy and its age,

$$Q_{\rm jet} = \frac{U_T}{t}. \tag{2.17}$$

The total energy input is inferred by the total internal energy contained in the lobes, i.e the sum of the energies in radiating particles and the magnetic field.

The total energy density in the lobes is output by SYNCH, as was used to determine the lobe pressures in Section 2.7.6. For the eastern lobe I obtain energy densities of 1.688×10^{-11} Jm^{-3} and 4.120×10^{-10} Jm^{-3} using the upper and lower limits to the magnetic field from equipartition and inverse-Compton measurements, respectively. For the western lobe I obtain energy densities of 1.734×10^{-11} Jm^{-3} and 1.072×10^{-9} Jm^{-3}. For the calculation of the jet power, an average of the energy densities in the eastern and western lobe was used. The total energy is simply these energy densities multiplied by the lobe volume. The lobes were modelled as ellipsoids, and their dimensions were input into the SYNCH code to output their volumes as 1.169×10^{62} m^3. The jet powers for 3C320 are tabulated below; for the range of possible energy densities described above, for the spectral ages at the upper and lower limit field strengths and for the derived dynamical age.

TABLE 2.15: Derived jet powers for 3C320 based on constraints on the lobe magnetic field energy density, spectral and dynamical ages.

Magnetic field	U_T ($\times 10^{60}$ ergs)	Jet power (spectral age) ($\times 10^{45}$ ergs s^{-1})	Jet power (dynamical age) ($\times 10^{45}$ ergs s^{-1})
Equipartition	0.020	0.208 (JP)	0.0259
		0.012 (KP)[a]	
		0.168 (Tribble)	
Inverse-Compton	1.735	1.551 (JP)	2.250
		1.047 (KP)[a]	
		1.282 (Tribble)	

[a] The KP spectral ages, as noted in Table 2.12, are incorrectly fitted, giving incorrect spectral ages. These jet powers are therefore presented for completeness only.

2.8.3.2 3C444

As for the previous dynamical analysis for 3C444, the work I present here is based on that published by Croston et al. (2011). Here, the energy injected by the radio galaxy is based on the energetics immediately surrounding the northern lobe where shock heating is suggested to occur, where the energetic input is derived from the 'excess' energy over the pre-shock temperature of 3.6 keV. Using this analysis, they estimate the total energetic input from the expanding radio lobes at 8.2×10^{60} erg, which I use to calculate the jet powers as given below in Table 2.16.

TABLE 2.16: Derived jet powers for 3C444 based on constraints on the lobe magnetic field energy density, spectral and dynamical ages. Note that, since the total energy U_T is not based on a determination of the magnetic field in the lobes (as explained above), the jet powers based on dynamical age are unchanged.

Magnetic field	U_T ($\times 10^{60}$ ergs)	Jet power (spectral age) ($\times 10^{45}$ ergs s^{-1})	Jet power (dynamical age) ($\times 10^{45}$ ergs s^{-1})
Equipartition	8.2	14.070 (JP)	2.900
		13.758 (KP)[a]	
		13.249 (Tribble)	
Inverse-Compton	8.2	6.843 (JP)	2.900
		6.684 (KP)[a]	
		6.061 (Tribble)	

Chapter 3

Discussion

The validity of spectral ageing used as a tool to derive the ages of radio galaxies has, in the past, been called into question due to the number of poorly constrained parameters required (Eilek, 1996; Eilek and Arendt, 1996; Blundell and Rawlings, 2001). However, recent developments in spectral ageing methods (Harwood et al., 2013) and the advance of high-resolution telescopes such as the *JVLA* and *Chandra* have given us the opportunity to probe the spectral age/dynamical age problem in greater detail.

The aim of this project was to probe the spectral age/dynamical age problem using high resolution multi-frequency observations of two powerful radio galaxies driving shocks into their environment. Both 3C320 and 3C444 are powerful FR-II radio galaxies in rich cluster environments based on previously existing images, and are clearly driving shocks as seen in previous *Chandra* observations for 3C444 (Croston et al., 2011). They are thus a representative sample for the population of FR-IIs in rich clusters, and are ideal objects to study the physics governing radio-loud AGN and the effect on their environment.

The objectives of this project were therefore to; produce sensitive, high-fidelity radio maps (which in combination with existing X-ray data of the cluster emission can give a detailed visualisation of both spectral ageing and driven cluster shocks), probe the spectral age/dynamical age problem, test the application of spectral ageing models in light of the results of previous similar work (Harwood et al., 2013, 2015) and calculate jet powers for 3C320 and 3C444. These objectives have been achieved, as detailed in Section 2.8. Here, I interpret my results and give their implications for powerful radio galaxies in rich cluster environments.

3.1 Interpretation of Results

3.1.1 3C320

For 3C320 I have found that, within their errors, the spectral and dynamical ages can agree, as seen in Tables 2.12 and 2.14. This agreement is based on selecting particular physical parameters; the lobe magnetic field constrained by equipartition and inverse-Compton measurements, the magnetic field strength which leads to an internal lobe pressure that is pressure balanced with the external medium and the choice of spectral ageing model used to describe the radiative losses in the lobes. These constraints, in the context of FR-II radio galaxies in cluster environments, are discussed below.

3.1.1.1 Lobe magnetic fields

For 3C320 I have found that, for the ages given by both the JP and Tribble models as shown in Table 2.12, the spectral and dynamical ages (Table 2.14) can *only* agree based on a relatively large departure from equipartition magnetic field strengths in the lobes (4.44 nT). That is, a magnetic field in between 0.5 nT (the inverse-Compton lower limit) and 1.00 nT gives the best agreement between the ages. Particularly for the JP model, a 0.5 nT field gives a spectral age ($35.48^{+0.74}_{-0.82}$ Myrs) that is consistent with the upper error bound on the dynamical age ($24.45^{+10.66}_{-4.49}$ Myrs). Given that these are 3σ errors, this represents an excellent agreement between spectral and dynamical ages.

The lobe magnetic field that gives an exact age agreement would be $\sim 0.9-1.1$ nT depending on the JP or Tribble model respectively. This would mean a departure from equipartition by a factor of $B \approx 0.2B_{eq}$ for 3C320—greater than that estimated for other samples of FR-II radio galaxies (Hardcastle et al., 1998, 2002), particularly more than the median ($B = 0.7B_{eq}$) of a sample studied by Croston et al. (2005b). Reconciling with the work from Harwood et al. (2013), a maximum spectral age occurs when $B = B_{CMB}/\sqrt{3}$ (based on differentiating Equation 1.21), leading to a field strength of $\sim 0.25B_{eq}$ for 3C436. This is also a large departure from their assumed equipartition field strengths, and would drive their spectral ages into more of an agreement to their older derived dynamical age for this source. This may suggest a common departure of $B \approx 0.2B_{eq}$ for powerful radio galaxies in rich environments, but more generally that equipartition between radiating particles and magnetic field does not occur in the lobes of powerful radio galaxies, in contrast to the results of Croston et al. (2004). This is not physically unrealistic since there is no *a priori* reason to believe that equipartition fields are the true field strengths in the lobes of radio galaxies, other than that they are close to the field strengths for which the total energy content in the lobes is minimized and that they are easy to calculate if we have the energy density from radiating particles.

Although the agreement between spectral and dynamical ages is based on the derived lower-limit magnetic field of 0.5 nT, by modelling the lobe emission with absorbed thermal and power-law components, it is not derived based on the *true* emission from the lobes since a robust detection of inverse-Compton emission was not made. Inverse-Compton and thermal emission is expected from the cluster regions where the lobes reside, however there may not be thermal emission from the lobes themselves. Foreground thermal cluster emission in front of the lobes was taken account of using a background region for these fits, which was chosen arbitrarily as a small region away from the shocked cluster medium so as to encompass some thermal cluster emission and some off-source noise. These counts were subtracted from the data, but this may not give an accurate representation of the actual amount of foreground emission needed to be subtracted from the data to accurately model the lobe regions. This is reflected in the large errors obtained for the best-fit temperatures for all regions—as given in Tables 2.3-2.6. The best fit thermal normalisation from the lobes therefore, may be an under or over-estimate of the true lobe thermal emission, if any. Consequently, the derived upper-limit power-law normalisation may also be an under or over-estimate, since these are the only two free parameters for the fit. However, since the upper limit of the inverse-Compton measurement does lead to magnetic field constraints using which the spectral and dynamical ages do agree, and further that, the fits to the lobe regions gave acceptable statistics ($\chi^2_{red} \sim 0.8 - 1.0$), I conclude that we can rely on the derived lobe magnetic fields as order of magnitude estimates, given the uncertainties on the X-ray measurements.

3.1.1.2 Ageing models

One of the assumptions used to model the spectra from the lobes of radio galaxies is that the initial energy distribution of the electrons takes the form of a power-law, and consequently the low-frequency spectra of the synchrotron emission is also a power-law (Equation 1.10). This, as explained previously, is governed by the injection index. For spectral ageing studies this was traditionally assumed to take on values around $\sim 0.5 - 0.7$ (e.g. Carilli et al. (1991a)). More recent studies by Harwood et al. (2013, 2015) tested these assumptions using BRATS and found much steeper injection indices at $\sim 0.80 - 0.85$.

In this project however, the best fit injection indices are flatter and closer to the historically found values of $\sim 0.60 - 0.65$. This suggests that the broad-band low-frequency data used in this project, in contrast to Harwood et al. (2013, 2015) where only a single data point at low-frequencies was used, is vital in order constrain the low-frequency power-law spectra sufficiently. This is important since steeper injection indices cause younger ages to be derived, thereby increasing the discrepancy with its dynamical age. On the other hand, Konar and Hardcastle (2013) found a strong positive correlation between the injection index and jet power for a sample of radio galaxies. Therefore, it is possible that the lower injection indices derived for 3C320 (as well as 3C444) compared to those in Harwood et al. (2013, 2015) are due to a lower jet power. A robust determination of the jet power based on the dynamical age using deep X-ray data is not given for these sources however, in contrast to 3C320, and therefore jet powers and

injection indices cannot be compared. Since both 3C320 and 3C444 have similar flat injection indices, it is unlikely that these sources were coincidentally selected with lower jet powers and those in (Harwood et al., 2013, 2015) all have higher jet powers. Although a model in which higher jet powers drive steeper injection indices cannot be neglected, the physical reality of this is somewhat uncertain, since a higher jet power implies a higher jet momentum which could also lead to a stronger shock at the jet termination point—hence a flatter injection index (see the discussion of Konar and Hardcastle (2013)). I therefore suggest that, since the sources in Harwood et al. (2013, 2015) are similar to 3C320 and 3C444 in their morphology and environment, the flat injection indices found in this work is solely due to the broad-band low frequency data obtained.

For 3C320 the JP and Tribble models gave spectral ages that were approximately consistent with each other (see Table 2.12), albeit with $\chi^2_{\rm red} \approx 6$, giving an excellent agreement between the spectral and dynamical age of 3C320 while assuming a constant lobe magnetic field of ~ 1 nT. This gives strong evidence to suggest that the JP, and particularly the Tribble model which provides a physically realistic description of the source with a varying magnetic field, may be the models of choice for spectral ageing. This was also suggested by Harwood et al. (2013, 2015), since the KP model assumes a constant pitch angle for the electrons with respect to the lobe magnetic field which is unlikely for such a large scale source. However, they found better χ^2 statistics for the KP model.

In this work, the KP fits did not provide significantly better statistics than the JP and Tribble models (lower by a factor ~ 1.1 in the average χ^2_{red}). However, the KP model produced somewhat erroneous fits to the data. An age of 52.53 Myrs was fitted for all three magnetic field strengths without any upper errors. Increasing the input age parameter to from 50 to 500 Myrs then produced ages of ~ 511 Myrs, again without upper errors. Steeper injection indices of ~ 0.9, which would give a younger age, did also not rectify this problem. I therefore investigated the fits using a small region in the eastern lobe where the fitted ages seemingly show a discontinuous jump to very high ages, shown in Figure 3.1.

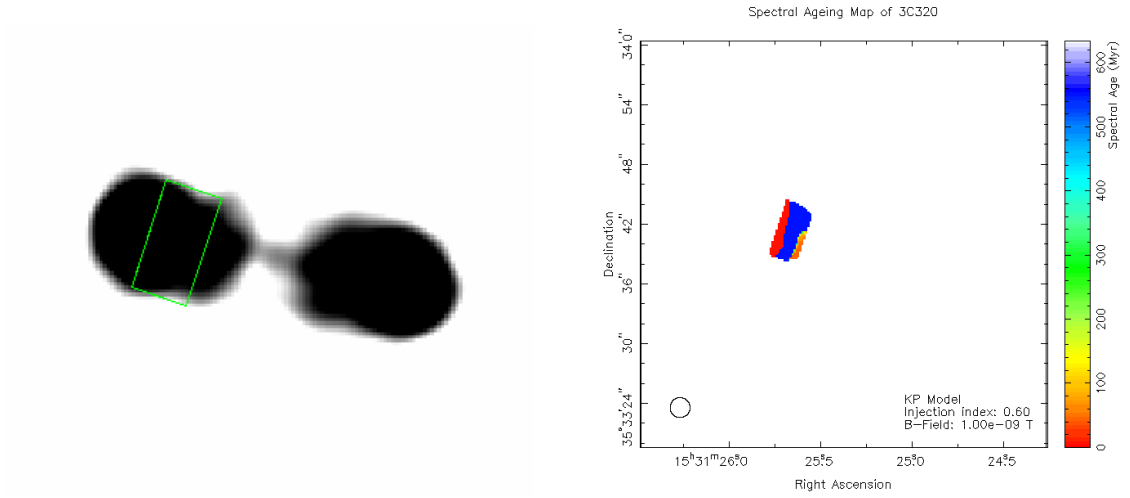

(A) Defining a small region of the eastern lobe using ds9.

(B) Spectral age fits.

FIGURE 3.1: Testing the KP model fitting using a small region where large age jumps are fitted, as seen above in Figure 3.1B. The maximum age parameter is at 500 Myrs and the magnetic field at 1.00 nT.

As shown by the spectra for these regions in Figure 3.2, it can clearly be seen that the KP model is not well fitted at these regions to the higher frequency C-band data. The best-fit line passes through none, or only a few, of the C-band flux points, although this can also be seen for the L-band data albeit with a better fit. This implies that the model intrinsically rejects high frequency curvature at these regions, and is only fitting a power-law to both low and high-frequencies with a spectral break frequency lower than the lowest observed frequency at L-band. As a consequence, this would give a physically implausible ageing process with a maximum age at some value > 500 Myrs. Spectra are shown for two regions also from the same spectral ageing map in Figure 3.1, although fitted with physically realistic young and old ages, and it can be seen in Figure 3.3 that the KP model fits reasonably well to the high-frequency data. This suggests that at some level the KP model is inconsistent with the data for 3C320 at the regions shown in Figure 3.1, although it is uncertain to what extent.

A further region was created only including the bottom of the eastern lobe away from the blue areas as shown in Figure 3.1, where the oldest electrons are expected to reside, and the KP model was fitted at 1.00 nT. As predicted, this gave an age of $30.83^{+1.45}_{-0.60}$ Myrs with a good fit of $\chi^2_{\text{red}} = 3.52$. This is ~ 5 Myrs older than that given by the JP and Tribble model at this magnetic field strength, although much more consistent than previous fits. The much lower χ^2 value obtained compared to the JP and Tribble models is noticeable, and similar to what was found by Harwood et al. (2013, 2015), although this may be due to the much smaller region size used (45 regions compared to 2100 for the JP and Tribble). Therefore, given the uncertainties associated with the fitting of the KP model as well as its unphysical description of a constant pitch angle, I suggest that the JP and Tribble models should be the models of choice for future spectral ageing studies.

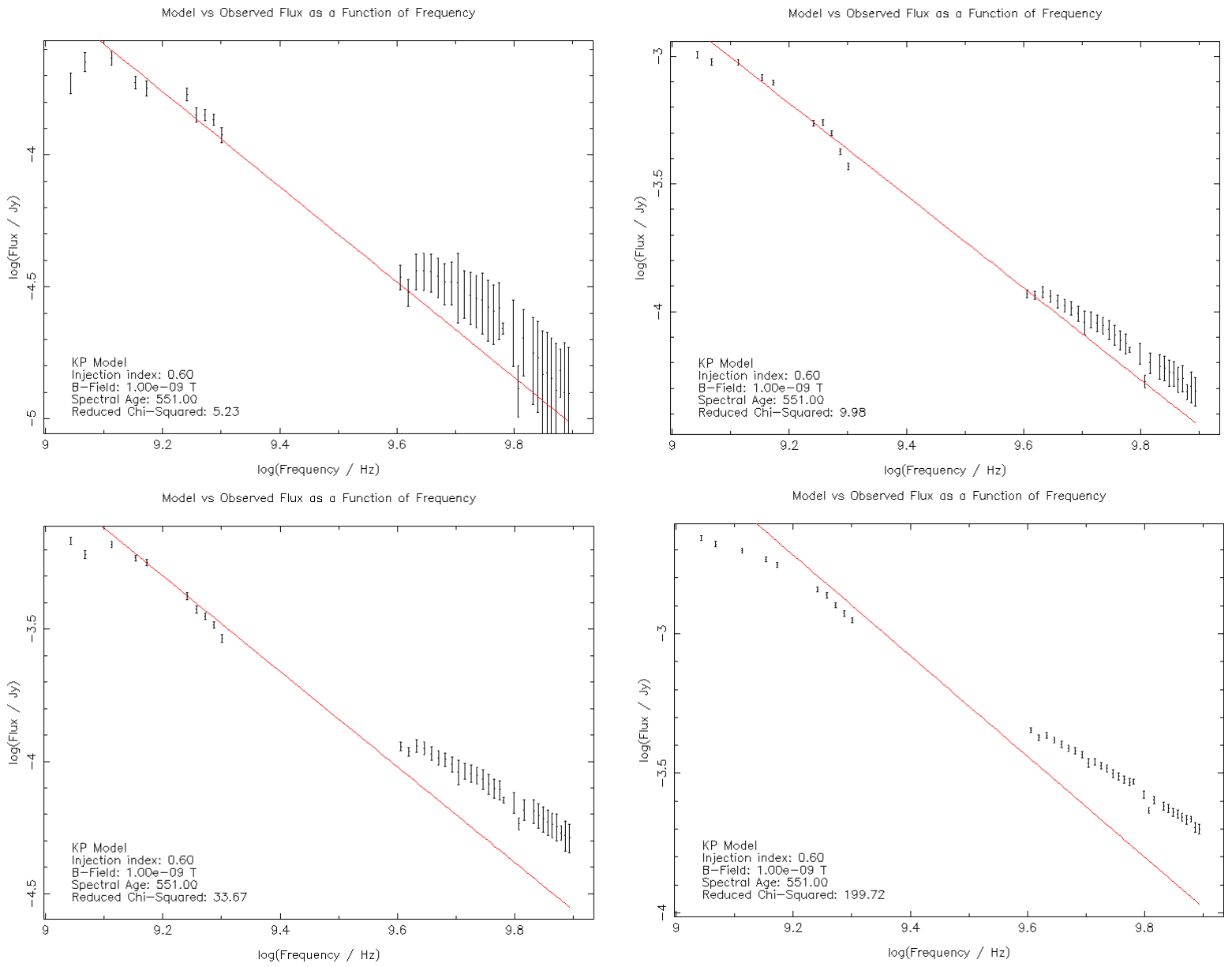

FIGURE 3.2: Spectra for the lobe region of 3C320 defined in Figure 3.1, fitted with the KP model at 1.00 nT. Fitted spectra from individual regions with increasing χ^2_{red} from left to right.

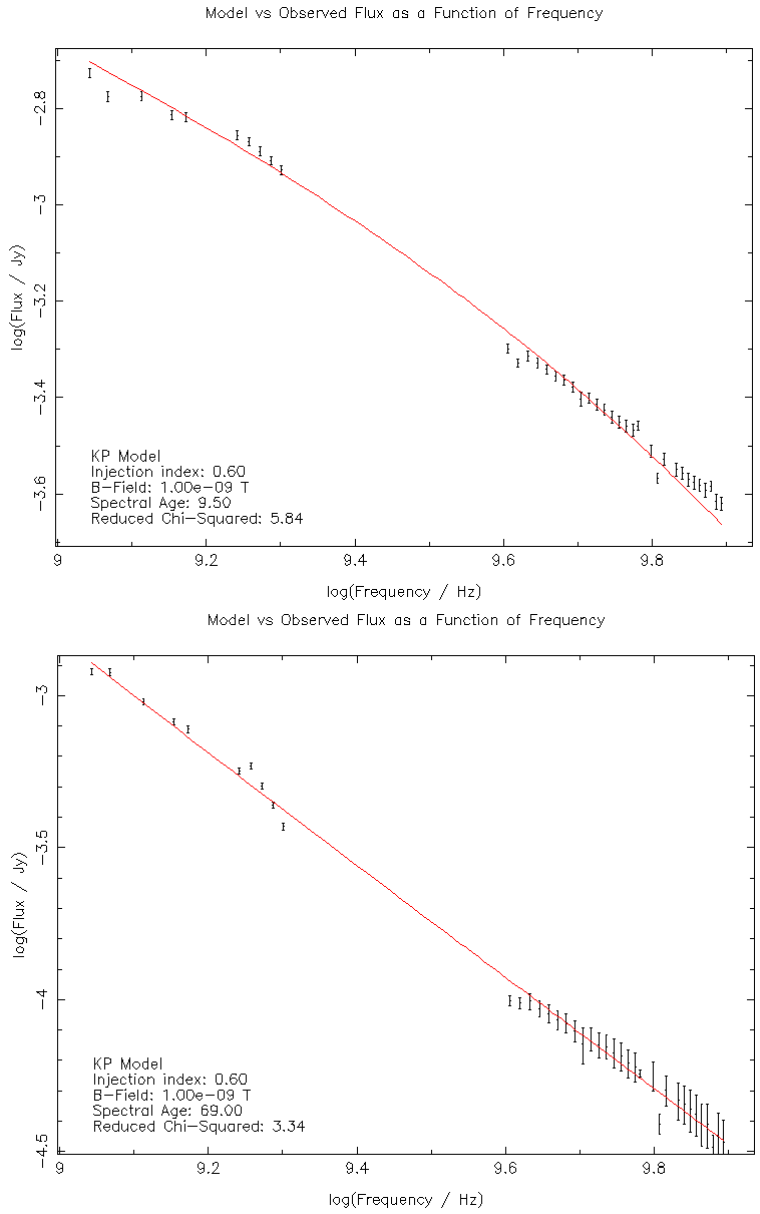

FIGURE 3.3: Spectra for two regions of 3C320 fitted with reasonable ages ($\leqslant$ 100 Myrs).

Nevertheless, and notwithstanding the strange behaviour of the KP model, all regions are still rejected at the 3σ confidence level for all three models based on the medium binning method (Harwood et al., 2013), and this is a cause of concern. The errors on the flux points from the radio images may be underestimated, which would result in high χ^2 values. Although a standard 2% flux calibration error was applied prior to fitting, they are only assumed and may be larger. The large χ^2 may also be due to issues with pixel alignment which wasn't performed for 3C320 due to poorly resolved L-band images, as explained previously. Pixel alignment will therefore be implemented once the higher resolution e-MERLIN data is obtained, which may improve the region selection by BRATS and also the quality of the data at L-band.

3.1.1.3 Pressure balance

In many models for the dynamical evolution of powerful radio galaxies, it is evident that the internal pressure of the lobes must be much greater than the external pressure of the medium (Scheuer, 1974; Kaiser and Alexander, 1997), particularly for supersonically advancing lobes. As a minimum condition for FR-II sources to exist therefore, the pressures between the lobe and the external medium must at least be balanced.

As explained previously in Section 2.76, the internal lobe pressure is the sum of the contributions from radiating particles (electrons) $p_{\rm rad}$, non-radiating particles (e.g protons) $p_{\rm nr}$ and the pressure from the magnetic field p_B so that $p_{\rm int} = p_{\rm rad} + p_{\rm nr} + p_B$. Equivalently this can be given by $p_{\rm int} = \frac{1}{3}u_T$ where u_T is the total energy density in the lobes (energy per unit volume). For FR-II sources it is not generally expected that there is a significant contribution from ultra-relativistic non-radiating particles in the lobes (Belsole et al., 2007) and so $p_{nr} \ll p_{rad}, p_B$, as was assumed for 3C444 by Croston et al. (2011). I therefore did not include a contribution to the total energy density from non-radiating particles. The pressure, or equivalently the energy density, in radiating particles was found using a combination of the synchrotron emissivity, lobe magnetic field and lobe volume (see Equation 1.8). The magnetic field pressure is defined as $p = \frac{1}{3}u_B = \frac{1}{3}\frac{B^2}{2\mu_0}$ and is therefore trivial to calculate from the magnetic field strength. I therefore obtained a range of lobe internal pressures based on the range of possible magnetic field strengths used in this work for 3C320. The total internal lobe pressures for 3C320 were calculated using SYNCH.

According to the results in Table 2.9, I find that for 3C320 the lobes are, at minimum, pressure balanced. Considering the propagated 3σ upper bound error on the external pressure however, the lobes may still be under-pressured if we consider the equipartition field (4.44 nT) as the true lobe magnetic field. Potentially therefore, there may be a requirement of extra pressure such as that from relativistic non-radiating particles, if the equipartition magnetic field is used. For the lower limit field strength (0.5 nT), there is a significant overpressure in the lobes by 2 orders of magnitude. For the field strength at which the spectral and dynamical ages agree (1.00 nT), there will still be a significant overpressure in the lobes, which is what is required by dynamical models for a supersonic ($\mathscr{M} \approx 2$) shock for a powerful radio galaxy. This pressure balance constraint therefore agrees with the agreement between the spectral and dynamical ages.

This result for 3C320 however, represents a deviation from the conclusions of Belsole et al. (2007); Hardcastle and Croston (2010) regarding the relationship between particle content and environment of FR-IIs—that the lobes of rich cluster FR-IIs tend to be underpressured unless a significant contribution from non-radiating particles (protons) is present. The apparent under-pressure may be associated with

some other intrinsic physical mechanism in the lobes. Since entrainment is unlikely for high power radio galaxies, it is possible that the existence of non-radiating particles in the lobes may be insufficient (or may not be true at all) to explain the apparent pressure imbalance for rich cluster FR-IIs found in previous studies. It is possible however that 3C320 is an isolated case, and therefore could represent the existence of peculiar physical processes relative to previously sampled rich-cluster FR-IIs.

3.1.1.4 Energetic impact

The jet powers calculated for 3C320 based on the derived spectral and dynamical ages are presented in Table 2.15. Based on the JP and Tribble models only, the jet power for the equipartition field is $\sim 2 \times 10^{44}$ ergs s^{-1}, while the power for the lower limit field is almost an order of magnitude higher. These are well within the values expected for FR-II sources based on dynamical models (Kaiser and Alexander, 1997). Since we have an agreement between spectral and dynamical ages, although the dynamical age has a large upper bound error of ~ 10 Myrs, this calculated jet power is a reliable estimate of the true energetic impact of 3C320 into its environment.

3.1.2 3C444

For 3C444, the dynamics are based on the work of Croston et al. (2011) and are only discussed briefly compared to 3C320.

3.1.2.1 Lobe magnetic fields

Similar to the X-ray analysis performed in this project, Croston et al. (2011) found constraints on the range of possible magnetic fields for the lobes of 3C444 using an equipartition estimate (1.05 nT) and a field strength leading to an upper-limit inverse-Compton measurement (0.5 nT). Note that this upper-limit was made at the 1σ confidence level, giving a flux of 9 nJy at 1 keV. I therefore used these field strengths as upper and lower limits to the true lobe magnetic field to test the spectral ageing models, while also using an intermediary field strength of 0.74 nT—see Table 2.13.

Using these magnetic fields however, looking at Tables 2.13 and 2.14, the spectral ages are still inconsistent with the dynamical age of 3C444. The spectral ages fitted to the JVLA broad bandwidth data are discrepant by a factor ~ 3 from the dynamical age of ~ 90 Myrs, similar to the discrepancy obtained by Croston et al. (2011), although they derive slightly older ages due to their assumption of a very flat injection index of $\alpha_{inj} = 0.5$. Considering that these spectral ages, which have been measured for 3C444 in Croston et al. (2011) as well in this project using the new and improved methods developed by Harwood et al. (2013), this may point to an inaccurate determination of the dynamical age of 3C444, as discussed below.

3.1.2.2 Dynamical age uncertainty

The dynamical age for 3C444, presented by Croston et al. (2011), was based on a Mach number for the driven shock determined by only the temperature ratios in the shocked and unshocked medium in the northern lobe only—in contrast to the analysis performed in this project for 3C320 where both density and temperature ratios were used from the fits to both lobes. Furthermore, the unshocked region for 3C444 was chosen as a small region encompassing the region just above the northern lobe (reasons for which are given in Croston et al. (2011)), rather than in this project where for 3C320 the entire unshocked cluster region was used. The temperature measurements were poorly constrained, and therefore a dynamical age based solely on the temperature jumps may be inaccurate, although the error on the Mach number was only 24%. The Mach number calculated based on the surface brightness (density) jump was $\mathscr{M} \sim 3$, a factor of two greater than that implied by the temperature jump ($\mathscr{M} \sim 1.7$). A dynamical age based on this Mach number would therefore yield an age a factor of 2 lower (~ 45 Myrs). This would significantly decrease the discrepancy with spectral ages—fitted results gave ~ 43 Myrs for the Tribble model at the lower limit magnetic field of 0.5 nT. I therefore suggest that the constrained Mach number for 3C444, based on poorly constrained temperatures obtained from the X-ray data, is the most probable reason for the discrepancy between ages.

3.1.2.3 Projection effects

Projection effects may play a role in producing a younger spectral age than the potentially true dynamical age for 3C444. If 3C444 is oriented such that the northern lobe is closer to the observer rather than on the plane of the sky, and consequently the southern lobe further away from the observer, this may explain the apparent existence of the northern hotspot only. As can be seen for the images obtained for 3C444, a clear bright hotspot is observed for the northern lobe, while the southern lobe shows no such signs. This may be an implication of the Doppler-shift of the observed break-frequency ν_b, which may be blue-shifted to a higher frequency for the northern lobe, giving a younger spectral age as given by Equation 1.21. The opposite would then be true for the red-shifted southern lobe which would then give an older spectral age relative to the northern lobe. I therefore used BRATS to find the spectral ages for the northern and southern lobes individually, as shown in Figure 3.4.

As expected, the northern lobe had a younger spectral age of 25 Myrs while the southern lobe had an age of 36 Myrs. Although this discrepancy is small relative to the dynamical age, in deriving the most accurate spectral age for jet power estimates, beaming effects may need to be taken account of in future models for those radio galaxies that are not in the plane of the sky.

Projection effects may also underestimate the physical size of the source—affecting the calculation of the dynamical age. If the radio galaxy is truly on the plane of the sky, then the length of the source (from

the core to the hotspot) that is used to determine the dynamical age will be the most 'true' representation of the length. However, if the radio galaxy is oriented at a significant angle from the plane of the sky, then the projected size of the source will be an underestimate of the true size of the source. Consequently this will underestimate the calculated dynamical age, and for 3C444 this would give a dynamical age of $>$ 90 Myrs. Although this increase in dynamical age due to projection effects is expected to be small, this would indeed increase the discrepancy with the spectral ages for 3C444. However, it is generally expected that projection effects are relatively unimportant for radio galaxies compared to other classes of radio-loud AGN since, according to unification models (Section 1.6), they are expected to lie on the plane of the sky. I suggest therefore that, although projection effects are important in determining the most accurate spectral and dynamical ages, they do not give a major contribution to the spectral age/dynamical age problem.

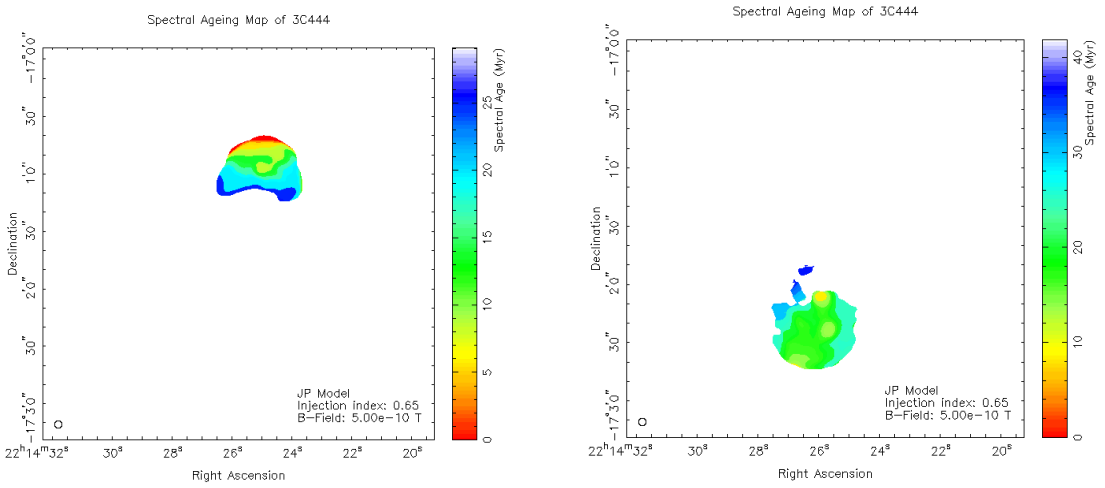

(A) North lobe. (B) South lobe.

FIGURE 3.4: Spectral age fits to the individual lobes of 3C444 using the JP model at 0.50 nT. Note that the colour scaling is different on both images.

3.1.2.4 Ageing models

The injection indices fitted to the lobes of 3C444 using the JP, KP and Tribble model gave consistent results—all models fitted using all three magnetic field strength values gave best-fit values of $\alpha_{inj} \approx 0.65$, although the Tribble model fit was not performed due to the reasons outlined in Section 2.8.1.1, and the JP model fitted indices were taken. Note that this injection index is slightly steeper than that assumed as an *a priori* for the spectral age calculations by Croston et al. (2011) ($\alpha_{inj} = 0.5$).

Similar to the fitted injection indices, the maximum spectral ages obtained were also consistent between the three models for a given magnetic field strength used—see Table 2.13. The fits for the lower limit field strength of 0.5 nT gave ages of $\sim$ 43 Myrs for the JP and Tribble models, while the KP model

gave a slightly younger age. These ages are consistent with the spectral ages derived by Croston et al. (2011), given their flatter injection indices, but still inconsistent with their dynamical age. The average $\chi^2_{\rm red} \sim 10$ obtained in these fits are larger than that obtained for 3C320 as well as for the sources analysed by Harwood et al. (2013, 2015). Again, as explained previously for the statistics for 3C320, this may be attributed to an underestimation on the flux errors in the radio maps.

3.1.2.5 Pressure balance

Croston et al. (2011) found that, for 3C444, the lobes are apparently under-pressured and that there may be a significant contribution from non-radiating particles for pressure balance. Although this is usually attributed to FRI sources due to particle entrainment, other studies have also shown that in similar environments, FR-II radio galaxies tend to be more proton dominated (Belsole et al., 2007; Hardcastle and Croston, 2010). However the analysis from Section 3.1.1.3 regarding 3C320 deviates from these conclusions, suggesting that the apparent under-pressure of the lobes of previously studied sources may be due to other causes. Particularly for 3C444, this may include uncertainties on the temperature measurements leading to potentially incorrect pressure measurements for the external medium. However, given the results from Croston et al. (2011), I also suggest that entrainment of non-radiating particles from the external medium cannot be ruled out, since there is not sufficient evidence to suggest otherwise for FR-II radio galaxies.

It is possible that the estimated magnetic fields are overestimated, since lower magnetic fields would both give older spectral ages and also a higher lobe energy density leading to higher pressures—potentially leading to a pressure balance. It is clear therefore that, either deeper and more sensitive X-ray observations of the cluster surrounding 3C444 must be obtained, or that a further sample of FR-II radio galaxies in rich cluster environments must be studied in order to establish a whether a relationship does indeed exist between lobe particle content and environment for the most powerful sources.

3.1.2.6 Energetic impact

The jet powers obtained for 3C444 using spectral ageing, as well as that obtained by Croston et al. (2011), are given in Table 2.16. There is a clear and expected discrepancy between the jet powers derived using spectral and dynamical ages, highlighting the importance of probing the spectral age/dynamical age discrepancy once more. They are however still in the range expected based on dynamical models (Kaiser and Alexander, 1997). The true age therefore, must be obtained to calculate the true energetic impact of 3C444 on its environment.

3.2 Implications for the dynamics and energetics of 3C320 and 3C444

Recent work using similar spectral ageing analysis (Harwood et al., 2013, 2015) has given the result that spectral ages are underestimated by a factor of 2 (or more), assuming the dynamical ages are the true ages of the source. Furthermore, steep injection indices were found in same work, suggesting that the previously held assumption of a flat spectral index at low-frequencies may not be true.

In this project I find that the injection indices are in fact flat as is found traditionally, suggesting that the lack of low-frequency data showing a power-law spectrum for the hotspots can cause the steep injection indices found by (Harwood et al., 2013, 2015). I find that the spectral age and dynamical age for 3C320 can agree precisely, with a constant lobe magnetic field strength around ~ 0.9 nT—close to the lower limit obtained through the upper-limit inverse-Compton measurement (0.5 nT). However, the high χ^2 values and statistical rejection of all the models at 3σ cannot be neglected, and further work must be done to determine the true flux measurement errors for the JVLA radio maps in order to probe this. I find that the lobes are significantly over-pressured using the magnetic field strength that gives an agreement between the ages, giving further confidence that a field strength of ~ 1.00 nT is close to the true lobe value, and deviating from the conclusions of Croston et al. (2011); Belsole et al. (2007); Hardcastle and Croston (2010)—that the lobes of powerful radio galaxies in rich environments may include a significant contribution from non-radiating particles. This suggests a requirement for the analysis of a larger sample of FR-II sources in rich-cluster environments in order to establish the role of the environment in the dynamical evolution of radio galaxies.

For 3C444, there is still an age discrepancy, even with broad-bandwidth high-resolution images complimented with the existing high-resolution *Chandra* observations analysed in Croston et al. (2011). With some confidence I can therefore rule out poor radio data quality as a reason for the spectral age/dynamical age discrepancy. Since the ages for 3C320 can agree (depending on the magnetic field) using the same spectral age analysis, this may imply that the dynamical age could be the cause of the discrepancy for 3C444, and therefore deeper and more sensitive X-ray observations are needed. Referring to the discussion in Section 3.1.2.2, I conclude that the determination of the Mach number based on both the temperature and surface brightness jumps, as was done for 3C320 in this project, would yield the most reliable and accurate calculation of the dynamical age and hence an agreement in spectral and dynamical ages for powerful radio galaxies in general.

Owing to the high resolution data obtained for 3C444, there is also a suggestion of physical projection effects such as Doppler-shifts and inaccurate size measurements playing a role in the determination of spectral ages, although these effects are less of a concern for radio galaxies in the context of AGN studies in general. However, in order for the most accurate determination of their spectral ages, and therefore

jet powers, projection effects should be taken into consideration in future ageing studies. Furthermore, the complex structure seen in the lobes and the jets of 3C444 (Figure 2.14) are interesting features that are usually unobserved for FR-II sources—possibly due to the low resolution and limited capabilities of the previous generation radio telescopes. X-ray analysis for 3C444 in Croston et al. (2011) gave peculiar temperature variations in the southern lobe—the temperature being highest in the middle and comparatively cooler in the outer edge where a hotspot is likely to exist. Deeper X-ray observations are needed to probe this further to identify the cause of this, whether these temperature variations are due to physical intrinsic features that may be observed in the lobes of other radio galaxies, or that we simply do not know the extent of thermal emission from the lobes of radio galaxies and that thermal models cannot therefore be applied to give conclusive temperature measurements.

The inconsistent behaviour in these lobes may point to a variation its physical parameters (such as the temperature as discussed above) to an extent that cannot be modelled with current spectral ageing models. Although, variations in the lobe magnetic field as a function of position, for example, was found to be insufficient to explain the variation in radio and X-ray properties for the lobes of Pictor A (Hardcastle and Croston, 2005). On the other hand, Machalski et al. (2009) suggest that a spatial variation in the lobe magnetic field strength, with a departure from equipartition as concluded for 3C320 in this work, could decrease the discrepancy between dynamical and spectral ages. Assumptions such as a constant lobe magnetic field may therefore also give rise to the spectral age/dynamical age discrepancy, although the Tribble model gives some account of this through the application of a Gaussian random field.

In terms of spectral ageing models, this work is consistent with the work of Harwood et al. (2013, 2015)— I find that the spectral ageing model of choice is the Tribble model. Along with losses based on the JP model, which itself also results in spectral ages which agree with the dynamical age for 3C320, a physically realistic non-uniform magnetic field gives plausibility to use the Tribble model. The KP model, although in the past it has given better fit statistics, is not as physically realistic as the JP or Tribble. Furthermore, as shown in this work, the KP model was inconsistent with the spectra for 3C320 which otherwise produced consistent results by applying the JP and Tribble models. However, given that the KP model produced consistent results with other models for 3C444, I cannot conclusively reject the KP model as a physical model for spectral ageing. Further tests must therefore be made of the KP model to justify its use for future spectral ageing studies.

Chapter 4

Conclusion and future work

In developing the kinetic luminosity function (the jet power as a function of radio luminosity), an accurate and reliable age is a crucial parameter. Given that the ages are accurately derived, and therefore the jet power, the kinetic luminosity function can then essentially derive kinetic powers for all radio-loud AGN out to high redshifts. This will in fact become possible in the near future with the advent of the Square Kilometre Array (SKA) (described below), which will have the resolution and sensitivity to produce high fidelity images of radio galaxies to high redshift—where powerful FR-IIs are more common. This will also allow studies of the jet power of radio galaxies as a function of redshift, and the opportunity to incorporate accurate quantifications of the energetic impact of radio galaxies into AGN feedback models. Since deep X-ray observations may not be possible for high-redshift sources, the importance of spectral ageing being a reliable tool to determine source ages therefore, cannot be understated.

The conclusions I make from this project are:

- Based on the analysis of 3C320, the spectral and dynamical ages agree precisely. However, the poor fits to the data should not be ignored, and I attribute this to the poorly known flux errors of the radio data. I infer that the age discrepancies for other previously studied sources are a result of the fact that such broad-bandwidth data at low and high frequencies were not obtained. Future spectral ageing studies therefore, should include this, particularly with the advance of the broad-bandwidth capabilities of the JVLA. I suggest that the true low frequency injection index is indeed flat ($\alpha_{inj} \sim 0.5 - 0.7$), contrary to recent similar work (Harwood et al., 2013, 2015), and suggest that deriving a reliable injection index should be based on constraining the low-frequency spectrum at multiple frequencies.
- The traditionally assumed lobe magnetic field value based on equipartition estimates may not be close enough to the true magnetic field for the lobes of powerful radio galaxies in rich clusters.

Inverse-Compton measurements are therefore essential in providing constraints on the magnetic field used to determine spectral ages.

- Since temperature measurements of the cluster medium based on X-ray data may be poorly constrained, a combination of the temperature and surface brightness measurements should be used to determine a Mach number—as has been done in this project. This can potentially yield more accurate dynamical ages and resolve the discrepancy with spectral ages.

- Should the spectral age/dynamical age discrepancy be resolved, by testing the suggestions made in this project for a further sample of FR-II sources, projection effects must then be taken account of in order to determine the most accurate spectral ages, and hence the true energetic impact of FR-II radio galaxies on their environment.

4.1 Proposed future work

The conclusions I have made above have addressed some previous questions regarding the validity of spectral ageing as a tool to derive the age of a radio galaxy. However, some outstanding questions still remain regarding dynamics of these sources. The true relationship between lobe particle content and the environment of FR-II sources for example, still needs to be addressed. With regards to the KP model giving a valid description of spectral ageing in the lobes of radio galaxies, further tests on 3C320 will be made, when the higher-resolution L-band e-MERLIN data becomes available. This will allow further detail to be seen on smaller scales, therefore allowing pixel alignment to be performed. This may improve the spectral age fitting on BRATS, and potentially may also give reliable ages for the KP model. Further deep and higher-resolution X-ray observations of the lobes of 3C320 could also be made, in order to give more information regarding lobe thermal emission. Although analysis using deep X-ray observations can provide a good proxy for the physical parameters of the source, simulations can provide an alternate method of probing the physics of radio galaxies.

Particularly with simulations, the dynamical age is known precisely. This presents an opportunity to test the physical parameters that are used to determine the spectral age, and probe suggestions that have been made in this project regarding magnetic field constraints for example. Furthermore, parameters such as the magnetic field strength and information on the bulk flow of the electrons in the lobes can be used to compute the approximate synchrotron emissivity, and hence synthetic radio maps of the source which can then be compared with the observed radio maps for accuracy. Physical parameters can then be tested with those inferred from observations. For example, a range of angles from the plane of the sky can be tested to see the effect on the dynamical age. This would be particularly useful for 3C444, where I have suggested that the projected size plays a small role in the spectral age/dynamical age discrepancy. Furthermore, the Mach number which gives an agreement between spectral and dynamical ages

for 3C444 should be tested, and simulations compared with the high resolution observations obtained in this project. This would also give an opportunity to probe the peculiar temperature variations found by Croston et al. (2011) in the southern lobe and find the exact causes for this.

With models of spectral ageing incorporated into multidimensional simulations of the dynamical evolution of radio galaxies (e.g. Jones et al. (1999)), it would also be interesting to compare the simulated radio maps with the observed radio maps, giving direct indications of which spectral ageing model gives the best description of the source, and to test the robust suggestion that the Tribble model is the spectral ageing model of choice for powerful radio galaxies.

Other than simulations to probe the spectral age/dynamical age discrepancy, it would also be useful to sample 3C444 further to probe the complex diffuse structure in its observed jets, as seen in Figure 2.4. Polarization images can give insight into a possible complex magnetic field structure within the jets, which may be the cause of this diffuse nature which are generally not observed for FR-II sources. 3C444 therefore represents an interesting source for further study, and will ultimately require higher-resolution and more sensitive observations to observe features on smaller scales, which is indeed possible with existing instruments such as MERLIN. However, with even higher resolution, it would be possible to observe at higher redshift, which is particularly important for FR-II radio galaxies in rich clusters where they are more commonly found. This will be possible with the SKA, as described below.

The SKA is an ongoing project to build the world's largest radio telescope—with up to a million low-frequency antennas and thousands of mid to high-frequency dishes covering a square kilometre. This will enable sky surveys at an an unprecedented level of resolution and sensitivity, and most importantly, at extremely high redshifts when the first galaxies were formed. This will allow, as mentioned above, all radio-loud AGN to be observed out to high redshift. This is particularly important for FR-II sources in rich cluster environments which are scarce at low-redshift where observations using current telescopes can give the resolution and sensitivity required for spectral ageing analysis. Spectral ageing tools will therefore need to be optimized for future studies using the SKA, to obtain the most accurate ages of radio galaxies in order to obtain information on their energetic impact and therefore their role in AGN feedback and overall galaxy evolution. Spectral ageing studies of a further sample of FR-II sources in rich clusters will therefore need to be completed, in order to test whether my findings are robust for the population of powerful radio galaxies, or simply isolated cases.

Bibliography

Aharonian, F.A., 2002. Proton-synchrotron radiation of large-scale jets in active galactic nuclei. *MNRAS*, 332:215.

Alexander, P., 1985. A radio study of 3C 390.3 - A precessing jet? *MNRAS*, 213:743.

Alexander, P., 1987. A study of spectral ageing in the radio galaxy 3C234 and its implications. *MNRAS*, 225:27.

Alexander, P. and Leahy, J.P., 1987. Ageing and speeds in a representative sample of 21 classical double radio sources. *MNRAS*, 225:1.

Antonucci, R., 1993. Unified models for active galactic nuclei and quasars. *Annual Review of Astronomy and Astrophysics*, 31:473.

Balbus, S.A. and Hawley, J.F., 1998. Instability, turbulence, and enhanced transport in accretion disks. *Reviews of Modern Physics*, 70:1.

Bartel, N., Herring, T.A., Ratner, M.I., et al., 1986. VLBI limits on the proper motion of the 'core' of the superluminal quasar 3C345. *Nature*, 319:733.

Barthel, P.D., 1989. Is every quasar beamed? *ApJ*, 336:606.

Basson, J.F. and Alexander, P., 2003. The long-term effect of radio sources on the intracluster medium. *MNRAS*, 339:353.

Begelman, M.C., Blandford, R.D., and Rees, M.J., 1984. Theory of extragalactic radio sources. *Reviews of Modern Physics*, 56:255.

Bell, A.R., 1978. The acceleration of cosmic rays in shock fronts. I. *MNRAS*, 182:147.

Belsole, E., Worrall, D.M., Hardcastle, M.J., et al., 2007. High-redshift Fanaroff-Riley type II radio sources: large-scale X-ray environment. *MNRAS*, 381:1109.

Best, P.N., 2004. The environmental dependence of radio-loud AGN activity and star formation in the 2dFGRS. *MNRAS*, 351:70.

Bicknell, G.V., 1984. A model for the surface brightness of a turbulent low Mach number jet. I - Theoretical development and application to 3C 31. *ApJ*, 286:68.

Birkinshaw, M., Laing, R.A., and Peacock, J.A., 1981. Radio synthesis observations of 3C 296, 3C 442A and 3C 449 at 0.4, 1.4 and 2.7 GHz. *MNRAS*, 197:253.

Blandford, R.D. and Znajek, R.L., 1977. Electromagnetic extraction of energy from Kerr black holes. *MNRAS*, 179:433.

Blundell, K.M. and Rawlings, S., 2001. Spectral ageing: a new age perspective. In R.A. Laing and K.M. Blundell, editors, *Particles and Fields in Radio Galaxies Conference*, volume 250 of *Astronomical Society of the Pacific Conference Series*, page 363.

Burch, S.F., 1979. Multifrequency studies of seven 3CR radio sources. II - Results and interpretation. *MNRAS*, 186:519.

Carilli, C.L. and Harris, D.E., 1996. *Cygnus A – Study of a Radio Galaxy*.

Carilli, C.L., Perley, R.A., Dreher, J.W., et al., 1991a. Multifrequency radio observations of Cygnus A - Spectral aging in powerful radio galaxies. *ApJ*, 383:554.

Carilli, C.L., Perley, R.A., Dreher, J.W., et al., 1991b. Multifrequency radio observations of Cygnus A - Spectral aging in powerful radio galaxies. *ApJ*, 383:554.

Cavagnolo, K.W., Donahue, M., Voit, G.M., et al., 2008. An Entropy Threshold for Strong Hα and Radio Emission in the Cores of Galaxy Clusters. *ApJ*, 683:L107.

Celotti, A. and Fabian, A.C., 1993. The Kinetic Power and Luminosity of Parsecscale Radio Jets - an Argument for Heavy Jets. *MNRAS*, 264:228.

Comerford, J.M., Pooley, D., Barrows, R.S., et al., 2015. Merger-driven Fueling of Active Galactic Nuclei: Six Dual and Offset AGNs Discovered with Chandra and Hubble Space Telescope Observations. *ApJ*, 806:219.

Condon, J.J., Cotton, W.D., Greisen, E.W., et al., 1998. The NRAO VLA Sky Survey. *AJ*, 115:1693.

Cowie, L.L. and Binney, J., 1977. Radiative regulation of gas flow within clusters of galaxies - A model for cluster X-ray sources. *ApJ*, 215:723.

Croston, J.H., Birkinshaw, M., Hardcastle, M.J., et al., 2004. X-ray emission from the nuclei, lobes and hot-gas environments of two FR II radio galaxies. *MNRAS*, 353:879.

Croston, J.H., Hardcastle, M.J., Birkinshaw, M., et al., 2005a. Jet/Environment Interactions of FRI and FRII Radio Galaxies. In L.O. Sjouwerman and K.K. Dyer, editors, *X-Ray and Radio Connections*.

Croston, J.H., Hardcastle, M.J., Birkinshaw, M., et al., 2008. An XMM-Newton study of the environments, particle content and impact of low-power radio galaxies. *MNRAS*, 386:1709.

Croston, J.H., Hardcastle, M.J., Harris, D.E., et al., 2005b. An X-Ray Study of Magnetic Field Strengths and Particle Content in the Lobes of FR II Radio Sources. *ApJ*, 626:733.

Croston, J.H., Hardcastle, M.J., Mingo, B., et al., 2011. A Large-scale Shock Surrounding a Powerful Radio Galaxy? *ApJ*, 734:L28.

Croston, J.H., Kraft, R.P., Hardcastle, M.J., et al., 2009. High-energy particle acceleration at the radio-lobe shock of Centaurus A. *MNRAS*, 395:1999.

Croton, D.J., Springel, V., White, S.D.M., et al., 2006. The many lives of active galactic nuclei: cooling flows, black holes and the luminosities and colours of galaxies. *MNRAS*, 365:11.

Eilek, J.A., 1996. How Radio Sources Stay Young: Spectral Aging Revisited. In P.E. Hardee, A.H. Bridle, and J.A. Zensus, editors, *Energy Transport in Radio Galaxies and Quasars*, volume 100 of *Astronomical Society of the Pacific Conference Series*, page 281.

Eilek, J.A. and Arendt, P.N., 1996. The Synchrotron Spectrum of Diffuse Radio Sources: Effects of Particle and Field Distributions. *ApJ*, 457:150.

Elitzur, M. and Shlosman, I., 2006. The AGN-obscuring Torus: The End of the "Doughnut" Paradigm? *ApJ*, 648:L101.

Erlund, M.C., Fabian, A.C., Blundell, K.M., et al., 2006. Extended inverse-Compton emission from distant, powerful radio galaxies. *MNRAS*, 371:29.

Fabian, A.C., 1984. X-rays from active galactic nuclei. *Physica Scripta Volume T*, 7:129.

Fabian, A.C. and Nulsen, P.E.J., 1977. Subsonic accretion of cooling gas in clusters of galaxies. *MNRAS*, 180:479.

Fanaroff, B.L. and Riley, J.M., 1974. The morphology of extragalactic radio sources of high and low luminosity. *MNRAS*, 167:31P.

Giovannini, G., Cotton, W.D., Feretti, L., et al., 2001. VLBI Observations of a Complete Sample of Radio Galaxies: 10 Years Later. *ApJ*, 552:508.

Goodger, J.L., Hardcastle, M.J., Croston, J.H., et al., 2008. Inverse Compton emission from the lobes of 3C353. *MNRAS*, 386:337.

Greenstein, J.L. and Matthews, T.A., 1963. Redshift of the Radio Source 3C 48. *ApJ*, 68:279.

Hardcastle, M.J., 2008. Hotspots, Jets and Environments. In T.A. Rector and D.S. De Young, editors, *Extragalactic Jets: Theory and Observation from Radio to Gamma Ray*, volume 386 of *Astronomical Society of the Pacific Conference Series*, page 46.

Hardcastle, M.J., 2013. Synchrotron and inverse-Compton emission from radio galaxies with non-uniform magnetic field and electron distributions. *MNRAS*, 433:3364.

Hardcastle, M.J., Birkinshaw, M., and Worrall, D.M., 1998. Magnetic field strengths in the hotspots of 3C 33 and 111. *MNRAS*, 294:615.

Hardcastle, M.J. and Croston, J.H., 2005. The Chandra view of extended X-ray emission from Pictor A. *MNRAS*, 363:649.

Hardcastle, M.J. and Croston, J.H., 2010. Searching for the inverse-Compton emission from bright cluster-centre radio galaxies. *MNRAS*, 404:2018.

Hardcastle, M.J., Evans, D.A., and Croston, J.H., 2007. Hot and cold gas accretion and feedback in radio-loud active galaxies. *MNRAS*, 376:1849.

Hardcastle, M.J., Evans, D.A., and Croston, J.H., 2009. The active nuclei of $z \leq 1.0$ 3CRR radio sources. *MNRAS*, 396:1929.

Hardcastle, M.J. and Krause, M.G.H., 2013. Numerical modelling of the lobes of radio galaxies in cluster environments. *MNRAS*, 430:174.

Hardcastle, M.J., Worrall, D.M., Birkinshaw, M., et al., 2002. A Chandra observation of the X-ray environment and jet of 3C 31. *MNRAS*, 334:182.

Hargrave, P.J. and Ryle, M., 1974. Observations of Cygnus A with the 5-km radio telescope. *MNRAS*, 166:305.

Harwood, J.J., Hardcastle, M.J., and Croston, J.H., 2015. Spectral ageing in the lobes of cluster-centre FR II radio galaxies. *MNRAS*, 454:3403.

Harwood, J.J., Hardcastle, M.J., Croston, J.H., et al., 2013. Spectral ageing in the lobes of FR-II radio galaxies: new methods of analysis for broad-band radio data. *MNRAS*, 435:3353.

Hill, G.J. and Lilly, S.J., 1991. A change in the cluster environments of radio galaxies with cosmic epoch. *ApJ*, 367:1.

Högbom, J.A., 1974. Aperture Synthesis with a Non-Regular Distribution of Interferometer Baselines. *A&A Supp.*, 15:417.

Jaffe, W., Meisenheimer, K., Röttgering, H.J.A., et al., 2004. The central dusty torus in the active nucleus of NGC 1068. *Nature*, 429:47.

Jones, T.W., Ryu, D., and Engel, A., 1999. Simulating Electron Transport and Synchrotron Emission in Radio Galaxies: Shock Acceleration and Synchrotron Aging in Axisymmetric Flows. *ApJ*, 512:105.

Kaiser, C.R. and Alexander, P., 1997. A self-similar model for extragalactic radio sources. *MNRAS*, 286:215.

Kataoka, J. and Stawarz, Ł., 2005. X-Ray Emission Properties of Large-Scale Jets, Hot Spots, and Lobes in Active Galactic Nuclei. *ApJ*, 622:797.

Kellermann, K.I. and Pauliny-Toth, I.I.K., 1981. Compact radio sources. *Annual Review of Astronomy and Astrophysics*, 19:373.

Kennicutt, Jr., R.C., 1989. The star formation law in galactic disks. *ApJ*, 344:685.

King, A.R. and Pringle, J.E., 2007. Fuelling active galactic nuclei. *MNRAS*, 377:L25.

Konar, C. and Hardcastle, M.J., 2013. Particle acceleration and dynamics of double-double radio galaxies: theory versus observations. *MNRAS*, 436:1595.

Krause, M., 2005. Very light jets II: Bipolar large scale simulations in King atmospheres. *A&A*, 431:45.

Lattimer, J.M. and Prakash, M., 2004. The Physics of Neutron Stars. *Science*, 304:536.

Leahy, J.P., 1991. *Interpretation of large scale extragalactic jets*, page 100.

Leahy, J.P., Muxlow, T.W.B., and Stephens, P.W., 1989. 151-MHz and 1.5-GHz observations of bridges in powerful extragalactic radio sources. *MNRAS*, 239:401.

Lobanov, A.P., 1998. Ultracompact jets in active galactic nuclei. *A&A*, 330:79.

Longair, M.S., 2011. *High Energy Astrophysics*.

Longair, M.S., Ryle, M., and Scheuer, P.A.G., 1973. Models of extended radiosources. *MNRAS*, 164:243.

Machalski, J., Chyży, K.T., Stawarz, Ł., et al., 2007. A method for estimating the dynamical age of FR II-type radio sources from multi-frequency data. *A&A*, 462:43.

Machalski, J., Jamrozy, M., and Saikia, D.J., 2009. A multifrequency study of giant radio sources - III. Dynamical age versus spectral age of the lobes of selected sources. *MNRAS*, 395:812.

Martí-Vidal, I., Muller, S., Vlemmings, W., et al., 2015. A strong magnetic field in the jet base of a supermassive black hole. *Science*, 348:311.

Massaro, F., Harris, D.E., Tremblay, G.R., et al., 2013. A Chandra Snapshot Survey for 3C Radio Galaxies with Redshifts between 0.3 and 0.5. *ApJ*, 206:7.

Mathews, W.G. and Bregman, J.N., 1978. Radiative accretion flow onto giant galaxies in clusters. *ApJ*, 224:308.

Matthews, T.A. and Sandage, A.R., 1963. Optical Identification of 3C 48, 3C 196, and 3C 286 with Stellar Objects. *ApJ*, 138:30.

Meisenheimer, K., Roser, H.J., Hiltner, P.R., et al., 1989. The synchrotron spectra of radio hot spots. *A&A*, 219:63.

Meurer, G.R., Heckman, T.M., Leitherer, C., et al., 1995. Starbursts and Star Clusters in the Ultraviolet. *AJ*, 110:2665.

Mingo, B., Hardcastle, M.J., Croston, J.H., et al., 2014. An X-ray survey of the 2 Jy sample - I. Is there an accretion mode dichotomy in radio-loud AGN? *MNRAS*, 440:269.

Mitton, S. and Ryle, M., 1969. High resolution observations of Cygnus A at 2. 7 GHz and 5 GHz. *MNRAS*, 146:221.

Mullin, L.M. and Hardcastle, M.J., 2009. Bayesian inference of jet bulk-flow speeds in Fanaroff-Riley type II radio sources. *MNRAS*, 398:1989.

Mullin, L.M., Riley, J.M., and Hardcastle, M.J., 2008. Observed properties of FRII quasars and radio galaxies at z ¡ 1.0. *MNRAS*, 390:595.

Mushotzky, R.F., 1984. X-ray emission from clusters of galaxies. *Physica Scripta Volume T*, 7:157.

Mushotzky, R.F., Serlemitsos, P.J., Boldt, E.A., et al., 1978. OSO 8 X-ray spectra of clusters of galaxies. I - Observations of twenty clusters: Physical correlations. *ApJ*, 225:21.

Netzer, H., 2015. Revisiting the Unified Model of Active Galactic Nuclei. *Annual Review of Astronomy and Astrophysics*, 53:365.

Offringa, A.R., van de Gronde, J.J., and Roerdink, J.B.T.M., 2012. A morphological algorithm for improving radio-frequency interference detection. *A&A*, 539:A95.

Omma, H. and Binney, J., 2004. Structural stability of cooling flows. *MNRAS*, 350:L13.

O'Neill, S.M. and Jones, T.W., 2010. Three-Dimensional Simulations of Bi-Directed Magnetohydrodynamic Jets Interacting with Cluster Environments. *ApJ*, 710:180.

Orrù, E., Murgia, M., Feretti, L., et al., 2010. Low-frequency study of two giant radio galaxies: 3C 35 and 3C 223. *A&A*, 515:A50.

Owen, F.N., Ledlow, M.J., Morrison, G.E., et al., 1997. The Cluster of Galaxies Surrounding Cygnus A. *ApJ*, 488:L15.

Pearson, T.J. and Readhead, A.C.S., 1988. The milliarcsecond structure of a complete sample of radio sources. II - First-epoch maps at 5 GHz. *ApJ*, 328:114.

Pentericci, L., Van Reeven, W., Carilli, C.L., et al., 2000. VLA radio continuum observations of a new sample of high redshift radio galaxies. *A&A Supp.*, 145:121.

Perley, R.A., Schwab, F.R., and Bridle, A.H., editors, 1989. *Synthesis imaging in radio astronomy*, volume 6 of *Astronomical Society of the Pacific Conference Series*.

Perley, R.A., Willis, A.G., and Scott, J.S., 1979. The structure of the radio jets in 3C449. *Nature*, 281:437.

Pringle, J.E., 1981. Accretion discs in astrophysics. *Annual Review of Astronomy and Astrophysics*, 19:137.

Rachen, J.P. and Biermann, P.L., 1993. Extragalactic Ultra-High Energy Cosmic-Rays - Part One - Contribution from Hot Spots in Fr-II Radio Galaxies. *A&A*, 272:161.

Rees, M.J., 1966. Appearance of Relativistically Expanding Radio Sources. *Nature*, 211:468.

Rybicki, G.B. and Lightman, A.P., 1979. *Radiative processes in astrophysics*.

Saikia, D.J. and Salter, C.J., 1988. Polarization properties of extragalactic radio sources. *Annual Review of Astronomy and Astrophysics*, 26:93.

Scheuer, P.A.G., 1974. Models of extragalactic radio sources with a continuous energy supply from a central object. *MNRAS*, 166:513.

Seyfert, C.K., 1943. Nuclear Emission in Spiral Nebulae. *ApJ*, 97:28.

Shlosman, I., Begelman, M.C., and Frank, J., 1990. The fuelling of active galactic nuclei. *Nature*, 345:679.

Siebenmorgen, R., Haas, M., Krügel, E., et al., 2005. Discovery of 10 μm silicate emission in quasars. Evidence of the AGN unification scheme. *A&A*, 436:L5.

Smith, D.A., Wilson, A.S., Arnaud, K.A., et al., 2002. A Chandra X-Ray Study of Cygnus A. III. The Cluster of Galaxies. *ApJ*, 565:195.

Stawarz, Ł., Tanaka, Y.T., Madejski, G., et al., 2013. Giant Lobes of Centaurus A Radio Galaxy Observed with the Suzaku X-Ray Satellite. *ApJ*, 766:48.

Tingay, S.J., Jauncey, D.L., Reynolds, J.E., et al., 1998. The Subparsec-Scale Structure and Evolution of Centaurus A: The Nearest Active Radio Galaxy. *AJ*, 115:960.

Treister, E., Schawinski, K., Urry, C.M., et al., 2012. Major Galaxy Mergers Only Trigger the Most Luminous Active Galactic Nuclei. *ApJ*, 758:L39.

Turner, T.J. and Pounds, K.A., 1989. The EXOSAT spectral survey of AGN. *MNRAS*, 240:833.

Urry, C.M. and Padovani, P., 1995. Unified Schemes for Radio-Loud Active Galactic Nuclei. *PASP*, 107:803.

van der Laan, H. and Perola, G.C., 1969. Aspects of Radio Galaxy Evolution. *A&A*, 3:468.

Wardle, J.F.C., 1977. Upper limits on the Faraday rotation in variable radio sources. *Nature*, 269:563.

Wardle, J.F.C., Homan, D.C., Ojha, R., et al., 1998. Electron-positron jets associated with the quasar 3C279. *Nature*, 395:457.

White, S.D.M. and Frenk, C.S., 1991. Galaxy formation through hierarchical clustering. *ApJ*, 379:52.

Williams, R.K., 2004. Collimated Escaping Vortical Polar e^-e^+ Jets Intrinsically Produced by Rotating Black Holes and Penrose Processes. *ApJ*, 611:952.

Willis, A.G. and Strom, R.G., 1978. Multifrequency observations of very large radio galaxies. I - 3C 326. *A&A*, 62:375.

Wills, B.J., 1989. Optical-infrared synchrotron emission in luminous AGN. In L. Maraschi, T. Maccacaro, and M.H. Ulrich, editors, *BL Lac Objects*, volume 334 of *Lecture Notes in Physics, Berlin Springer Verlag*, page 107.

Wylezalek, D. and Zakamska, N.L., 2016. Evidence of suppression of star formation by quasar-driven winds in gas-rich host galaxies at z¡1? *MNRAS*, 461:3724.

Wyndham, J.D., 1965. A Search for Optical Objects Associated with 50 Radio Sources. *AJ*, 70:384.

Zensus, J.A., 1997. Parsec-Scale Jets in Extragalactic Radio Sources. *Annual Review of Astronomy and Astrophysics*, 35:607.